NANYANG TECHNOLOGICAL UNIVERSITY
SINGAPORE

# HYBRID ORGANIC-INORGANIC HALIDE PEROVSKITE NANOCRYSTALS FOR LIGHT-EMITTING DIODE APPLICATIONS

**BEVITA KALLUPALATHINKAL CHANDRAN**

**INTERDISCIPLINARY GRADUATE SCHOOL**
**ENERGY RESEARCH INSTITUTE @ NTU (ERI@N)**

**2018**

# HYBRID ORGANIC-INORGANIC HALIDE PEROVSKITE NANOCRYSTALS FOR LIGHT-EMITTING DIODE APPLICATIONS

BEVITA KALLUPALATHINKAL CHANDRAN

Interdisciplinary Graduate School
Energy Research Institute @ NTU (ERI@N)

A thesis submitted to the Nanyang Technological University in partial fulfilment of the requirement for the degree of
Doctor of Philosophy

**2018**

# Statement of Originality

I hereby certify that the work embodied in this thesis is the result of original research and has not been submitted for a higher degree to any other University or Institution.

| | |
|---|---|
| 16-01-2018 | Bevita Kallupalathinkal Chandran |
| . . . . . | . . . . . |
| Date | Student Name |

## Abstract

Organic-inorganic hybrid perovskite materials, in particular, $CH_3NH_3PbX_3$ and $CH(NH_2)_2PbX_3$ ($X = Cl^-, Br^-, I^-$) analogues, show great promise as active emitter materials for lighting, display, and lasing applications due to their narrow emission (i.e. high color purity), wavelength tunability, low-temperature formation, and high photoluminescence quantum yields (more than 90%). The need for charge confinement to aid radiative recombination advocates the use of perovskite nanocrystals (NCs) as the active emitting materials to attain efficient and bright perovskite-based LEDs. A robust and potentially scalable NC fabrication method is the ligand-assisted re-precipitation (LARP) protocol, in which highly luminescent colloidal NCs are prepared using long carbon chain ligands. These ligands passivate the NC surface, while restricting NC growth and reducing the non-radiative channels. The inherent insulating nature of the ligands, however, may inhibit the translation of high photoluminescence (PL) observed in the NCs into high electroluminescence (EL) under device operation, as it may act as an electrical injection barrier. Moreover, a uniform emissive layer is critical to prevent shunt paths between the different transport layers in the LED stack. Hence, an optimized synthesis protocol is required, in which charges are sufficiently confined in the NCs by the ligands (without imposing a further charge injection barrier) and concomitantly uniform surface coverage is attained (after solution processing).

In this thesis, two hypotheses to improve the current LARP protocol for preparation of $CH_3NH_3PbBr_3$ NCs for LED applications were investigated in detail. Firstly, an excess of $CH_3NH_3Br$ was added to aid surface passivation through the reduction of non-radiative defect pathways on the NC surface. A similar strategy has been employed during the direct crystallization of the halide perovskite phase from solution processing methods, however, the implications for the colloidal LARP synthesis are not yet reported. Herein, a non-

stoichiometric precursor ratio of $CH_3NH_3Br:PbBr_2$ = 1.15:1 displayed the best LED efficiency metrics, despite not recording the highest PL. I infer that the surface morphology and NC ink concentration are more decisive for good device performance than PL, as the EL is critically dependent on both carrier injection and fast radiative recombination.

Secondly, modulation of the perovskite NC size via solvent engineering during the NC synthesis is hypothesized to be a potential strategy to maximize the PL and EL efficiencies as the NC surface morphology and trap density are both greatly affected by the nanocrystal size. Moreover, charge carrier confinement, and thus radiative recombination rates, are also influenced. The ability to control the NC size distribution is therefore likely to be useful for LED applications. Herein, the effect of different $CH_3NH_3PbBr_3$ NC size distributions on the optical characteristics and device performance were investigated extensively. A split bimodal NC size distribution, with maximum crystallite populations centered at 10 and 17 nm diameter showed the lowest surface roughness (~4.5 nm) after thin film formation. In contrast, a single mode (centered at ~12 nm diameter) and narrow bimodal distributions (centered at ca. 8 and 18 nm diameter) displayed higher surface roughness of approximately 8.0 and 8.1 nm, respectively. In addition, the NC inks which displayed the single mode and narrow bimodal distributions demonstrated longer PL decay times, 38.8 and 48.7 ns respectively, compared to the split bimodal size distribution (12.6 ns). The fast-recombination and smooth NC thin films, obtained in the latter distribution, displayed the most stable and efficient LED characteristics, thus highlighting the importance of size distribution control.

Finally, $CH_3NH_3PbBr_3$ and $CH(NH_2)_2PbBr_3$ NCs were compared in terms of their optical properties and performance in LED devices. The importance of synthesis optimization, specific for each individual emitter material, was

demonstrated, and the overall favorable attributes of $CH(NH_2)_2PbBr_3$ NCs for LED operation were described in detail.

To summarize, this thesis examined the influence of variations in the precursor ratios as well as NC size distribution modulation via solvent engineering, during the colloidal perovskite NC synthesis, on the efficiency and stability of the NC-based LEDs. A comparison of the $CH_3NH_3PbBr_3$ and $CH(NH_2)_2PbBr_3$ NC synthesis optimizations for LED applications is also presented. The insights obtained from this research are expected to be advantageous for the design of perovskite NC synthesis protocols for optoelectronic applications.

## Acknowledgements

I would like to thank my main supervisor, Prof Chen Xiaodong, co-supervisor Prof Fan Hongjin, and mentor Prof Chen Zhong, who formed the Thesis Advisory Committee, for giving me the opportunity to pursue this project and their support and guidance. I would also like to thank my school, Interdisciplinary Graduate School (IGS) and university, Nanyang Technological University (NTU), Singapore, for the scholarship, research funding and facilities that made this project possible.

I would like to express my heartfelt gratitude to Prof Nripan Mathews, Prof Subodh Mhaisalkar and Dr. Sjoerd Veldhuis for their timely help, guidance and mentorship throughout this project. Without their assistance, this project would never have materialized.

I would like to extend my gratitude to all my colleagues in the ERI@N Lab in Research Techno Plaza, particularly, the LED device group members, Dr. Chin Xin Yu, Nur Fadilah Bte Jamaludin, Ng Yan Fong, Dr. Natalia Yantara and I.V. Kameshwar Rao for their constant encouragement and assistance during this work. I would also like to thank Dr. Annalisa Bruno, Dr. Damodaran Bahulayan, Dr. Sneha Kulkarni, Dr. Teddy Salim, Krishnamoorthy Thirumal, Dr. Saikat Bhaumik, Dr. Subas Kumar Muduli, Dr. Raihana Begum, Nguyen Huy Tiep (Andy), Dr. Chen Shi, Tay Yong Kang (Eugene), and Dr. Ajay Perumal for their assistance with various experiments and useful discussions.

I would also like to thank all my colleagues in Prof Chen Xiaodong's research group, especially, Guo Xintong, Dr. Yu Jiancan, Dr. Li Bin, Dr. Zhang Yanyan, Dr. Tang Yuxin, Dr. Qi Dianpeng, Dr. Yang Hui, Dr. Deng Jiyang, Dr. Liu Yaqing, Dr. He Ke, Dr. Leow Wan Ru, Chen Geng and Jiang Ying for their support and encouragement.

Finally, I would like to thank my family, particularly my father Mr. Chandran K. K., and friends, who became like family here, especially, Anjali Jayakumar, Dr. Rajini Antony, Johns Paul, Rijil Thomas, Aamani Budhota, and Sukriti Gupta for the constant motivation and unwavering support during this challenging and enriching part of my life. Thank you from the bottom of my heart.

# Table of Contents

# Table Captions

# Figure Captions

# Abbreviations

| | |
|---|---|
| 0D | Zero Dimensional |
| 1D | 1 Dimensional |
| 2D | 2 Dimensional |
| 3D | 3 Dimensional |
| AFM | Atomic Force Microscopy |
| BSE | Back-scattered Electron |
| CBM | Conduction Band Minimum |
| EL | Electroluminescence |
| ESCA | Electron Spectroscopy for Chemical Analysis |
| ETL | Electron Transporting Layer |
| HOMO | Highest Occupied Molecular Orbital |
| HRTEM | High Resolution Transmission Electron Microscopy |
| HTL | Hole Transporting Layer |
| IR | Infrared |
| LARP | Ligand-assisted Re-precipitation |
| LED | Light-emitting Diode |
| LUMO | Lowest Unoccupied Molecular Orbital |
| NC | Nanocrystal |
| NIR | Near-infrared |
| OLED | Organic Light-emitting Diode |
| Pe | Perovskite |
| PESA | Photoelectron Spectroscopy in Air |
| PL | Photoluminescence |
| PLE | Photoluminescence Excitation |
| QLED | Quantum-dot Light-emitting Diode |

| | |
|---|---|
| SAED | Selected Area Electron Diffraction |
| SAXS | Small-angle X-ray Scattering |
| SE | Secondary Electron |
| SEM | Scanning Electron Microscopy |
| TCSPC | Time-correlated Single Photon Counter |
| TEM | Transmission Electron Microscopy |
| TRPL | Time-resolved Photoluminescence |
| UPS | Ultraviolet Photoelectron Spectroscopy |
| UV | Ultraviolet |
| VBM | Valence Band Maximum |
| Vis | Visible |
| XRD | X-ray Diffraction |
| XPS | X-ray Photoelectron Spectroscopy |

**Chemical names**

| | |
|---|---|
| B3PYMPM | 4,6-bis(3,5-di(pyridin-3-yl)phenyl)-2-methylpyrimidine |
| BCP | Bathocuproine |
| DMF | *N*,*N*-dimethylformamide |
| DMSO | Dimethylsulfoxide |
| ITO | Indium Tin Oxide |
| PEDOT:PSS | Poly(3,4-ethylenedioxythiophene)-poly(styrenesulfonate) |
| PEO | Polyethylene oxide |
| PO-T2T | 2,4,6-Tris[3-(diphenylphosphinyl)phenyl]-1,3,5-triazine |
| PVK:PBD | (poly(9-vinylcarbazole):2-(4-biphenylyl)-5-phenyl-1,3,4-oxadiazole) |
| TPBI | 2,2′,2″-(1,3,5-benzinetriyl)-tris(1-phenyl-1-H-benzimidazole) |

**Physical Quantities**

| Abbreviation | Quantity | Unit |
|---|---|---|
| CE | Current Efficiency | cd $A^{-1}$ |
| $E_b$ | Binding Energy | meV |
| EQE | External Quantum Efficiency | % |
| FWHM | Full Width Half Maximum | nm |
| IQE | Internal Quantum Efficiency | % |
| J | Current Density | mA $cm^{-2}$ |
| L | Luminance | cd $m^{-2}$ |
| $L_{max}$ | Maximum luminance | cd $m^{-2}$ |
| PCE | Power Conversion Efficiency | % |
| PE | Power Efficiency | lm $W^{-1}$ |
| PLQY | Photoluminescence Quantum Yield | % |
| RH | Relative Humidity | % |
| V | Voltage | V |
| $V_T$ | Turn-on voltage | V |
| WF | Work Function | eV |

# Chapter 1

# Introduction

*In this Chapter, the motivation and hypothesis for this thesis are discussed. The scope of the project and its specific objectives are presented. Finally, the thesis overview and the novelty of the research are described in detail.*

## 1.1 Motivation and Hypothesis

Perovskite materials, particularly, the organic-inorganic hybrid lead halide perovskites have many positive attributes such as high absorption coefficients (greater than $10^4$ $cm^{-1}$),[1] long carrier diffusion lengths (exceeding 1 μm),[2,3] high photoluminescence efficiency,[4] facile band gap tuning by varying the halide composition,[5,6] etc. Furthermore, these halide perovskites can be conveniently synthesized via low-temperature solution processing techniques which make them promising for large scale manufacturing, and print technology compatible with flexible substrates.[7] The efficiencies of perovskite-based light emitting diodes (LEDs) have improved at a tremendous pace, from the first demonstration with <1% external quantum efficiency (EQE) in 2014,[8] to > 10% in 2017.[9,10] In these state-of-the-art devices, perovskite films are prepared by direct crystallization of the perovskite material from the precursor solutions. During this process, anti-solvent dripping and/or additional polymer layers are often used to optimize the film coverage and morphology. Particularly, precise control of the timing and angle of antisolvent deposition, at the specific spinning speed is crucial for attaining smooth films. Subsequently, the perovskite films are annealed to promote crystal formation, as well as to remove the high boiling point solvents in which the precursors are dissolved. Hence, the perovskite layer formation is quite complex and not easy to scale-up. Instead, a one-step deposition of pre-formed perovskite nanocrystal (NC) inks, similar to quantum dot light emitting diode (QLED) technologies, would be more viable for commercialization.

Ligand-assisted re-precipitation (LARP) is a colloidal synthesis technique for preparing highly luminescent perovskite NCs with the help of long carbon chain ligands.[6] The NCs are precipitated from the perovskite precursor solution at room temperature, with the help of miscible anti-solvents. The ligands restrict the NC growth as well as passivate the NC surface by binding to uncoordinated surface

atoms.[11] However, LEDs fabricated from NC inks prepared by the colloidal approach often exhibit much lower device efficiencies compared to the direct thin film crystallization approach.[12-14] One possible reason for the low efficiency is that the ligands, due to their inherent insulating nature, may act as an electric injection barriers. Other factors such as film morphology are also be crucial for device performance, as demonstrated in the mesoporous and planar architecture perovskite solar cells.[15] While good surface coverage of the perovskite layer is essential in any electronic device to prevent shunt paths, the morphological requirements are different for LEDs and solar cells. In case of solar cells, a large-grained (preferably single-crystalline) morphology is desired to enable efficient charge extraction and to prevent both radiative and non-radiative recombination.[16] In contrast, for LEDs radiative recombination is required. Therefore, a nanocrystal morphology, which provides spatial confinement of the charges, is desired. However, this can also increase surface trap-related non-radiative recombination as the surface-to-volume ratio increases with decreasing NC sizes. Hence, NC size, surface traps and film morphology are all factors which need to be modulated for improving perovskite LED performance.

In this project, modifications to the LARP synthesis protocol are proposed to improve the perovskite NC properties and their subsequent thin film formation for application in LEDs. The hypotheses are as follows. Firstly, the use of excess $CH_3NH_3Br$ during synthesis is expected to affect the surface passivation of the $CH_3NH_3PbBr_3$ NCs. Secondly, changes in synthesis conditions, such as the amount of anti-solvent used for precipitating the NCs in the LARP protocol, and introduction of a small amount of polar solvent during synthesis, are postulated to influence the size of NCs. The variation in NC sizes, and thereby the respective size distributions of the NC inks, is anticipated to influence the NCs' radiative recombination and the thin film morphology. Consequently, the synthesis modifications are expected to enhance the perovskite LED performance. In addition, the extension of the optimized synthesis protocol for $CH_3NH_3PbBr_3$

NCs to $CH_2(NH_2)_2PbBr_3$, NCs which exhibit higher thermal stability,[17] can likely boost the LED efficiencies.

## 1.2 Objectives and Scope

The objectives and scope of this project are outlined below.

- To investigate the factors affecting the translation of high photoluminescence (PL) achieved with the colloidal NC synthesis into high electroluminescence (EL) in the LEDs through small modifications in colloidal synthesis of perovskite NCs. Two approaches – (1) use of precursor non-stoichiometry to influence the surface passivation of the NCs, and (2) modulation of anti-solvent amounts and introduction of additional polar solvent in the NC synthesis, to influence the NC size distribution in the NC ink, are investigated. The LED efficiency and stability upon using aforementioned approaches are discussed.

- To examine whether the NC synthesis optimization of $CH_3NH_3PbBr_3$, is translatable to another perovskite system, specifically $CH_2(NH_2)_2PbBr_3$ NC synthesis. The intrinsic properties of the two materials that affects their respective LED performances are evaluated.

## 1.3 Thesis Overview

This thesis is organized as described below:

*Chapter 1* explains the motivation for this project on investigation of the colloidal synthesis of organic-inorganic hybrid lead halide perovskite NCs for LED applications. The hypotheses, specific project objectives, scope, and outcomes of the project are presented.

*Chapter 2* presents a comprehensive review of the development of halide perovskites in the field of optoelectronics, the emergence of perovskite-based light-emitting diodes, and their scope and challenges.

*Chapter 3* gives an overview of the modified LARP protocol employed for the organic-inorganic hybrid lead bromide perovskite NC synthesis in this project, as well as a description of the various experimental techniques used to evaluate the structural, optical, and chemical properties of the NCs and their thin films. The LED fabrication and testing methods are also discussed.

*Chapter 4* discusses the effect of modulation of $CH_3NH_3Br:PbBr_2$ ratio during $CH_3NH_3PbBr_3$ NC synthesis on the optical properties, crystal structure, particle size distribution, and film formation of the NC ink. LEDs fabricated using the modulated NC inks indicate that the NC surface properties and thin film morphology are more important to achieve high device efficiency than PL intensity of the films alone.

*Chapter 5* describes the influence of $CH_3NH_3PbBr_3$ NC size distribution variations on the optical, structural and topographical properties of the NC films. Three different size distributions - single mode, narrow bimodal and split bimodal – were achieved through modifications to the NC synthesis protocol in terms of anti-solvent amounts and introduction of an additional polar solvent. In addition, the effect of the size distribution variation on the LED device efficiency and stability were examined. The LEDs fabricated with NC inks exhibiting a split bimodal distribution demonstrated higher device efficiency and better stability than the single mode and narrow bimodal distributions. The improved device performance can be correlated to the lower thin film surface roughness and faster radiative recombination in the split bimodal NC size distribution as compared to the single mode and narrow bimodal distributions.

*Chapter 6* examines the feasibility of using the optimized $CH_3NH_3PbBr_3$ NC synthesis protocol for the preparation of $CH_2(NH_2)_2PbBr_3$ NCs. The optical and structural properties of the NCs, and their respective LED performances are subsequently compared. The $CH_2(NH_2)_2PbBr_3$-based LEDs exhibited higher luminance compared to the $CH_3NH_3PbBr_3$-based LEDs, however, the higher current densities at turn-on luminance resulted in lower device efficiencies in the former. Introduction of quasi-2D phases by varying the ligand amounts, led to energy funneling from the quasi- 2D to 3D $CH_2(NH_2)_2PbBr_3$ NC phase, and consequently exceptional improvements in device efficiencies. Similar enhancements were, unfortunately, not achieved when the optimized $CH_2(NH_2)_2PbBr_3$ synthesis protocol was used to fabricate $CH_3NH_3PbBr_3$ NCs and subsequent light-emitting devices; thus emphasizing the need for material-specific synthesis optimization.

*Chapter 7* presents the scientific insights gained during this project for the optimization of colloidal organic -inorganic hybrid lead bromide perovskite NCs for LED applications. Suggestions for future work related to ligand choice during the NC synthesis, and selection of transport layers employed in the LED device stack are proposed.

## 1.4 Findings and Outcomes/Originality

- Phase-pure $CH_3NH_3PbBr_3$ NCs were prepared with various molar ratios of $CH_3NH_3Br$:$PbBr_2$, viz. 1:1, 1.05:1, 1.15:1 and 1.25:1. A comparison of the optical and morphological properties, and LED device characterizations, demonstrated that the NC surface properties and thin film morphology were more influential than PL intensity on the LED efficiency.

- $CH_3NH_3PbBr_3$ NC inks with three different NC size distributions – single

mode, narrow bimodal, and split bimodal distributions, were synthesized by small variations to the LARP protocol. Specifically, the amount of the anti-solvent (toluene) used was modulated and an additional polar solvent (1-butanol) was introduced. Subsequent studies revealed that the NC size distribution in the NC ink influenced not only the efficiency of LEDs, but also their operational stability.

- $CH_3NH_3PbBr_3$ NC inks and $CH_2(NH_2)_2PbBr_3$ NC inks were synthesized by two different protocols and their optical and structural properties and LED performances were compared. The investigations established that the colloidal NC synthesis protocol optimized for achieving high device efficiencies with $CH_3NH_3PbBr_3$ NCs may not be appropriate for $CH_2(NH_2)_2PbBr_3$ NC synthesis and vice versa. The synthesis optimization needs to be material-specific.

To conclude, several key factors for improving the efficiency and stability of colloidal perovskite NC-based LEDs were investigated in this thesis. The insights obtained from this research, combined with further improvements in the choice of ligands and the various layers in the LED device stack, is expected to spur the development of perovskite-based LEDs.

## 1.5 References

1 De Wolf, S. *et al.* Organometallic Halide Perovskites: Sharp Optical Absorption Edge and Its Relation to Photovoltaic Performance. *The Journal of Physical Chemistry Letters* **5**, 1035-1039, doi:10.1021/jz500279b (2014).

2 Xing, G. *et al.* Long-Range Balanced Electron- and Hole-Transport Lengths in Organic-Inorganic $CH_3NH_3PbI_3$. *Science* **342**, 344-347, doi:10.1126/science.1243167 (2013).

3 Stranks, S. D. *et al.* Electron-Hole Diffusion Lengths Exceeding 1 Micrometer in an Organometal Trihalide Perovskite Absorber. *Science* **342**, 341-344, doi:10.1126/science.1243982 (2013).

4 Gonzalez-Carrero, S. *et al.* The Luminescence of $CH_3NH_3PbBr_3$ Perovskite Nanoparticles Crests the Summit and Their Photostability under Wet Conditions is Enhanced. *Small* **12**, 5245-5250, doi:10.1002/smll.201600209 (2016).

5 Kitazawa, N., Watanabe, Y. & Nakamura, Y. Optical properties of $CH_3NH_3PbX_3$ (X = halogen) and their mixed-halide crystals. *Journal of Materials Science* **37**, 3585-3587, doi:10.1023/A:1016584519829 (2002).

6 Zhang, F. *et al.* Brightly Luminescent and Color-Tunable Colloidal $CH_3NH_3PbX_3$ (X = Br, I, Cl) Quantum Dots: Potential Alternatives for Display Technology. *ACS Nano* **9**, 4533-4542, doi:10.1021/acsnano.5b01154 (2015).

7 Di Giacomo, F., Fakharuddin, A., Jose, R. & Brown, T. M. Progress, challenges and perspectives in flexible perovskite solar cells. *Energy & Environmental Science* **9**, 3007-3035, doi:10.1039/C6EE01137C (2016).

8 Tan, Z.-K. *et al.* Bright light-emitting diodes based on organometal halide perovskite. *Nature Nanotechnology* **9**, 687-692, doi:10.1038/nnano.2014.149 (2014).

9 Xiao, Z. *et al.* Efficient perovskite light-emitting diodes featuring nanometre-sized crystallites. *Nature Photonics* **11**, 108-115, doi:10.1038/nphoton.2016.269 (2017).

10 Zhang, L. Q. *et al.* Ultra-bright and highly efficient inorganic based perovskite light-emitting diodes. *Nature Communications* **8**, 15640, doi:10.1038/ncomms15640 (2017).

11 Owen, J. The coordination chemistry of nanocrystal surfaces. *Science* **347**, 615-616, doi:10.1126/science.1259924 (2015).

12 Xing, J. *et al.* High-Efficiency Light-Emitting Diodes of Organometal Halide Perovskite Amorphous Nanoparticles. *ACS Nano* **10**, 6623-6630, doi:10.1021/acsnano.6b01540 (2016).

13 Li, J. *et al.* 50-Fold EQE Improvement up to 6.27% of Solution-Processed All-Inorganic Perovskite $CsPbBr_3$ QLEDs via Surface Ligand Density Control. *Advanced Materials* **29**, 1603885(1603881-1603889), doi:10.1002/adma.201603885 (2017).

14 Perumal, A. *et al.* High brightness formamidinium lead bromide perovskite nanocrystal light emitting devices. *Scientific Reports* **6**, 36733, doi:10.1038/srep36733 (2016).

15 Snaith, H. J. Perovskites: The Emergence of a New Era for Low-Cost, High-Efficiency Solar Cells. *The Journal of Physical Chemistry Letters* **4**, 3623-3630, doi:10.1021/jz4020162 (2013).

16 Herz, L. M. Charge-Carrier Dynamics in Organic-Inorganic Metal Halide Perovskites. *Annual Review of Physical Chemistry* **67**, 65-89, doi:10.1146/annurev-physchem-040215-112222 (2016).

17 Eperon, G. E. *et al.* Formamidinium lead trihalide: a broadly tunable perovskite for efficient planar heterojunction solar cells. *Energy & Environmental Science* **7**, 982-988, doi:10.1039/C3EE43822H (2014).

# Chapter 2

# Literature Review

*This Chapter describes the history and development of organic-inorganic hybrid lead halide perovskites. The early, and contemporary, demonstrations of perovskite-based light-emitting diodes (LEDs) are discussed in detail. The outlook for perovskite LED research, remaining challenges, and the scope for this thesis in context of literature, are summarized.*

## 2.1 History and Development of Organic-Inorganic Lead Halide Perovskites

The term perovskite refers to a class of compounds, which have the same crystal structure as calcium titanium oxide ($CaTiO_3$), named after Russian mineralogist, Count Lev Aleksevich von Perovski.[1] These compounds have the general chemical formula, $ABX_3$, wherein the X anion binds to cations A and B of dissimilar sizes. The ideal perovskite structure is a cubic lattice with the cations A and B at the center, and corners of the cube, respectively, and the X anions at the face centers. In the classical $ABO_3$ structure, this would yield a B-O distance = $a/2$ (where $a$ is the cubic unit cell parameter) while the A-O distance = $(a/\sqrt{2})$ and the following relationship holds between the ionic radii: $r_A + r_O = \sqrt{2}(r_B + r_O)$. However, it has been established that the perovskite structure is achieved within a tolerance factor, $t$, such that $0.75 < t < 1.0$ where $t = r_A + r_O / \sqrt{2}(r_B + r_O)$; $t$ is between 0.9 to 1 for cubic perovskite while the lower values give distorted perovskite structures.[2,3] As a consequence, a majority of the natural metals form stable perovskite-type oxide structures leading to applications in wide variety of areas such as catalysis,[4] piezoelectricity,[5] ferroelectricity,[6] super-conductivity,[7] magnetoresistivity,[8] to name a few.

Recently, halide perovskites have come to the forefront of the research world due to the exceptional advances in the field of photovoltaics, demonstrating solar cells with certified efficiencies close to 20%.[9] Herein, the halides are found at the X-site instead of oxygen, while monovalent and bivalent cations occupy the A-site and B-site, respectively as opposed to the bivalent and tetravalent cations found in the A and B-sites respectively for the oxide perovskites. These were first reported in 1958 by Moller for cesium lead halides.[10] Interestingly, the A-site, in-between the lead halide octahedrons, can also be occupied by small organic molecules with effective radii less than 260 pm, such as methylammonium, formamidinium, hydroxylammonium, hydrazinium and so on.[11,12] In fact, the

highest solar cell efficiencies have been achieved with these hybrid organic-inorganic lead halide perovskites, specifically, $CH_3NH_3PbI_3$ and $CH(NH_2)_2PbI_3$.[13,14]

The first report of organic cation in lead halide perovskites was made by Dieter Weber in 1978, who synthesized $CH_3NH_3PbX_3$ (X = Cl, Br, I).[15] Following this, layered perovskite systems (commonly, $(R\text{-}NH_3)_2MX_4$) came into the forefront, wherein the extended inorganic lead halide framework is separated by large organoammonium cations.[16] Typically, the ammonium heads of the cations form hydrogen bonds with the halogens in the inorganic sheets while the organic tails interact via van der Waals forces. These systems can be considered as multi-layered quantum well structures, with the metal halide sheets forming the wells and the wider bandgap organic layers forming the barriers. Due to their inherent quantum confinement as well as the large difference in dielectric constant between the organic and inorganic layers, these systems exhibit large exciton binding energies ($E_b$), for e.g., $(C_{10}H_{21}NH_3)_2PbI_4$ exhibits $E_b > 300$ meV.[17,18] This results in radiative decay of the excitons within the inorganic potential wells giving rise to strong room temperature photoluminescence (PL). The PL properties varies significantly depending on the metal atom, halogen, and the dimensionality of the perovskite material.

The effective dimensionality of the perovskite system is related to the thickness of the inorganic layer or sheet. The $AMX_3$ compound initially described, (which can be considered as infinite layers stacked together), is referred to as three-dimensional (3D) perovskite and the layered system is referred to as two-dimensional (2D) perovskite. In case of pure 2D phase, each inorganic layer is separated by large organic cations. Alternatively, if both small and large organic cations are present, a mixture of 2D and 3D phases, known as quasi-2D phases, can be formed in which multiple layers of inorganic sheets incorporating small organic cations, are sandwiched between the large organic cations. This results

in perovskites with different sheet thickness, $n$ = 2,3,4, etc., where $n$ refers to the number of inorganic layers, (pure 2D is $n$ =1). Similarly, depending on the organic cation used, instead of layered structure, one-dimensional (1D) or zero-dimensional (0D) structures can also be formed. As the dimensionality is reduced, band gap of materials progressively increases and changes in coloration from black to white, as well as increase in exciton binding energy are observed. For example, for 3D, $CH_3NH_3PbI_3$, exciton binding energy, $E_b$ = 30-45 meV while for quasi 2D, $(CH_3NH_3)_{n-1}(C_9H_{19}NH_3)_2Pb_nI_{n+1}$, (n=4, 3, 2), $E_b$ = 60, 96, 181-220 meV, respectively, for 2D, $(C_9H_{19}NH_3)_2PbI_4$, $E_b$ = 330-388 meV, for 1D, $[NH_2C(I){=}NH_2]_3PbI_5$, $E_b$ = 410 meV, and for 0D, $(CH_3NH_3)_4PbI_6{\cdot}2H_2O$, $E_b$ = 545 meV.[19]

Variation of the halide is also found to influence the bandgap of the material. For instance, the position of the excitonic peak in the absorption spectra shifted from 2.55 eV for $(C_{10}H_{21}NH_3)_2PbI_4$ to 3.17 eV for $(C_{10}H_{21}NH_3)_2PbBr_4$, and 3.75 eV for $(C_{10}H_{21}NH_3)_2PbCl_4$, indicating a progressive increase in the bandgap. The change in the optical properties with the change of halogen is due to the hybridization of metal and halogen states in the valance band maxima of the material, while metal states alone make up the conduction band minima.[20] Expectedly, a change in the metal atom also influences the optical properties; when the metal atom is varied from Pb to Sn and Ge, a red-shift as well as broadening of the PL peak is observed, indicating a decrease in band gap as well as a decrease in the exciton binding energy.[21]

These highly tunable halide perovskites are very interesting for optical applications. However, for electronic applications, the quantum well structure responsible for its exceptional room temperature luminance, becomes the hindrance. These materials are found to be largely insulating, and while quasi-2D and 3D structures show lower resistivity, as the number of inorganic sheets

increase, they also show lower exciton binding energies and hence their room temperature luminescence also decreases.

## 2.2 Early Demonstrations of Electroluminescence in Halide Perovskites

The first demonstration of electroluminescence (EL) from halide perovskites was on $(C_6H_5C_2H_4NH_3)_2(CH_3NH_3)Pb_2I_7$ (n=2) single crystals, wherein electric field was applied in-plane to the perovskite sheets using direct silver contacts, obtaining orange luminescence at 77 K.[22] Subsequently, EL was also demonstrated from perpendicular electric field application, using a thin layer of 2D phenylethylamine, $(C_6H_5C_2H_4NH_3)_2PbI_4$ as emitter in a heterostructure device consisting of indium tin oxide anode, an oxadiazole derivate electron transport layer and Mg-Ag cathode.[23] A green, 520 nm EL peak, with luminance > 10,000 cd $m^{-2}$ at 2 A $cm^{-2}$ current density was obtained by applying 24 V at 77 K. Further, the external quantum efficiency (EQE) of the devices were improved from ~0.9% obtained with $(C_6H_5C_2H_4NH_3)_2PbI_4$ to 2.8% (at 110 K) just by the change of emitter layer to cyclohexenylethylamine, $(C_6H_9C_2H_4NH_3)_2PbI_4$.[24] The room temperature luminance in these light emitting diodes (LEDs) was presumed to be hindered due to PL quenching because of thermal ionization of the excitons.[23]

The first room temperature EL from hybrid perovskites was demonstrated using a dye cation based on oligothiophene and ethylammonium units which can form $a(H_3N\text{-}R\text{-}NH_3)MX_4$) type layered structure.[25] Herein, the ammonium groups on the two ends of the organic cation bind to adjacent inorganic layers, removing the van der Waals gap between the layers. However, due to difficulty in solubilizing the oligothiophenes, this material could not be deposited by solution processing methods, and a thermal ablation method was required for the depositing the perovskite film for device fabrication. Following this first

demonstration of room temperature EL in 1999, this field was dormant until 2014, when 3D perovskite based-LEDs were reported.[26]

## 2.3 Rise of Halide Perovskites in the 21st Century

The renewed interest in halide perovskites was sparked by the development of 3D perovskite based solar cells. In 2009, $CH_3NH_3PbI_3$ and $CH_3NH_3PbBr_3$ were used as sensitizers in liquid-based dye-sensitized solar cells (DSSCs) and power conversion efficiencies (PCEs) of 3.8% and 3.1% respectively were attained.[27] This was improved to 6.5% PCE in 2011 by Im et al.[28] But the rapid degradation of the liquid based-DSSCs, due to the solubility of the perovskites in the liquid electrolytes, proved a major hindrance to further development of the field.

A significant breakthrough came in 2012 when the first solid-state perovskite solar cells were reported with PCEs of 7.6% and 9.7%.[29,30] Following this, perovskite solar cell PCE improved rapidly, reaching ~20% certified efficiency by 2015.[14] In addition, investigations on the potential of perovskite materials in other areas such as LEDs, lasing, photodetectors, transistors, memristors, etc. gained momentum.[1,31-34] This unprecedented rise of the perovskite-related research was due to the combination of numerous favorable attributes of perovskites, such as:

- the long and balanced electron and hole mobilities,[35]
- high absorption coefficients in the visible and near-infrared region,[36]
- facile bandgap tuning by variation of composition as well as dimensionality, (refer Section 2.2)
- compatibility with solution processing techniques applied in organic electronics and quantum dot-based electronics,[37] and
- potential for application in flexible devices,[38] to name a few.

## 2.4 Requirements for LED Application

### 2.4.1 Efficiency Requirements

1. High radiative recombination needs to be achieved in the emitter layer, inhibiting non-radiative recombination channels in the emitter layer and at the interfaces.
2. Pin-hole free emitter layer is required to prevent shunt paths and reduce leakage current.
3. Proper choice of electrodes and transport layers is crucial to ensure balanced electron and hole injection as well as minimize the injection barrier to reduce the turn-on voltage (voltage at which 1 cd $m^{-2}$ luminance is achieved).

To be commercially viable an EQE of ≈ 20% is needed. Building on the knowledge gained from organic and quantum-dot-based light emitting diodes (OLEDs and QLEDs), as well as the film formation techniques used in the perovskite photovoltaic applications, perovskite-based LEDs have made tremendous progress as discussed in Section 2.5.

### 2.4.2 Stability Requirements

For any practical application, device stability is a must. In terms of LEDs, an operational lifetime > 10,000 h wherein the spectral purity and intensity of the LED is maintained, is needed for commercialization. Given, the low formation energy of perovskites (~0.1-0.3 eV), these materials are unstable when exposed to heat, light, electric field, and most notoriously, moisture. Hence, the perovskite device fabrications are generally carried out in controlled atmosphere inside an Ar or $N_2$ glove box. The devices are then encapsulated inside the glove box before taking them outside for testing in ambient conditions. As the devices tend to heat up during operation, thermal stability of the materials is also important.

Intrinsically, the spectral purity of perovskites (especially for single halide systems), is one of the advantages of perovskites over the inorganic semiconductor quantum dots. Strategies to improve device stability, as well as to enable device fabrication in ambient conditions are being investigated by various research groups, as discussed in Section 2.5.

## 2.5 Current Developments in Perovskite-based LEDs

The first room temperature luminance from solution-processed perovskite-based LEDs was achieved in 2014, using $CH_3NH_3PbI_{3-x}Cl_x$ and $CH_3NH_3PbBr_3$ as the emitter layers.[26] The emitter layer was formed by spin coating the precursor solution (containing the methylammonium halide and lead halide precursors in the required ratios). The 3D perovskite material was sandwiched between two large bandgap semiconductors, to form a double heterostructure, to confine the injected charges. Moreover, given the small exciton binding energies of the 3D perovskites, the emitter layer was designed to be thin, to spatially confine the charges and promote radiative recombination. Re-absorption losses are also likely to be lower in the thinner films, enhancing luminescence. Thus, infrared emission with maximum EQE of 0.23% was achieved from ~15 nm-$CH_3NH_3PbI_{3-x}Cl_x$ emitter layer. Similarly, green luminance with 0.1% EQE was attained from ~20 nm-$CH_3NH_3PbBr_3$ emitter layer-based LEDs.

Notably the EQE increased with increasing voltage and current density, indicating that a high density of charges was required for efficient radiative recombination. However, both radiance and efficiency dropped at high current densities, which was attributed to device heating at high current densities as inferred from pulse bias experiments. Hence, thermal instability of the materials is one of the limiting factors for high electroluminescence and device efficiency. Other limiting factors were the incomplete surface coverage of the perovskite layer, creating possible shunt paths between the transport layers, as well as the

luminescence quenching at the perovskite/ semiconductor interface. The authors demonstrated that an ultra-thin layer of $Al_2O_3$ between the $TiO_2$ electron transport layer (ETL) and perovskite layer improved the device EQE from 0.23% to 0.76% (> 3-fold improvement).

Several techniques have been employed to improve the surface coverage and/or charge confinement in perovskite LEDs. One approach is to embed perovskite nanocrystals in a polymer matrix. This was demonstrated by Li et al. with $CH_3NH_3PbBr_3$ NCs in a polyimide matrix which yielded LEDs with 1.2% EQE.[39] Similarly, polyethylene oxide (PEO) has also been used to form the polymer matrix, using which LEDs could be made even without hole and electron transport layers.[40] Use of polymers was also shown to improve the stability of perovskites – ambient air fabrication of fully printed perovskite LEDs with 1.1% EQE were demonstrated using $CH_3NH_3PbBr_3$-PEO matrix as the emitting layer.[41] Meanwhile, LEDs based on fully inorganic perovskite, $CsPbBr_3$ which is typically more thermally stable than organic-inorganic hybrid perovskites, were also reported.[42] The polymer-matrix approach proved effective in improving the surface morphology for the inorganic perovskites also, and enabled the highest reported brightness (> 500000 cd $m^{-2}$) for perovskite-LEDs (EQE = 5.7%, device fabrication and measurement inside $N_2$ glove box) .[43]

Another promising approach to improve device efficiency was demonstrated by Cho et al, achieving 8.53% EQE.[44] Herein, a small organic molecule was dissolved in a highly volatile non-polar solvent (chloroform) and dropped onto the perovskite film during the spin coating process to reduce grain size, and increase uniformity, of the perovskite ($CH_3NH_3PbBr_3$) layer. In addition, a slight excess of $CH_3NH_3Br$ was used to reduce non-radiative recombination sites in the $CH_3NH_3PbBr_3$ layer by preventing the formation of metallic Pb atoms. Another interesting strategy is the use of bulky organoammonium halides along with the desired perovskite precursors to confine the nanocrystal growth, in situ film

formation, as demonstrated by Rand's group.[45,46] They achieved 10.4% EQE for the $CH_3NH_3PbI_3$ system (red emission) and 9.3% EQE for the $CH_3NH_3PbBr_3$ system (green emission) by this method.[45] Large excess of $CH_3NH_3Br$ precursor was also demonstrated to be beneficial for confining the excitons in $CH_3NH_3PbBr_3$ NCs by forming an in situ type I heterostructure ($CH_3NH_3Br$-$CH_3NH_3PbBr_3$-$CH_3NH_3Br$) within the emitter layer.[47] These researchers also employed a solvent-vacuum-drying process to remove the excess solvent instead of the commonly used thermal annealing method, to prevent aggregation of the NCs, and observed a 7-fold improvement in EQE compared the LEDs with thermal annealed perovskite films. Recently, Byun et al. demonstrated LEDs fabricated from quasi-2D perovskites, $(C_6H_5C_2H_4NH_3)_2(CH_3NH_3)_{m-1}Pb_mBr_{3m+1}$ ($m$ = 1-4, integer). Herein, carrier funneling from larger band gap (lower $m$ value) to smaller band gap (higher $m$ value) perovskite crystals, enables carrier injection into the smallest band gap crystal where in radiative recombination occurs.[48] Efficiency of the layered perovskite devices were significantly improved, by Qian et al., by controlling the distribution of the different layered perovskites in the emitter layer, achieving an EQE of 7.4%.[49] Incorporation of $Cs^+$ and $CH(NH_2)_2^+$ cations in the $CH_3NH_3PbX_3$ perovskites is another promising strategy employed to improve the stability of perovskite-based LEDs with efficiencies matching that of $CH_3NH_3PbX_3$ emitter layer.[50,51]

A completely different approach for perovskite-based LEDs, is to prepare the perovskite film by deposition of inks containing perovskite nanocrystals (NCs) synthesized by colloidal methods. In the colloidal synthesis, the NC growth as well as agglomeration are inhibited by ligands which attach to the NC surface. These ligands also passivate the surface defects, enabling high luminance from the NCs.[52] The shape and size of such NCs can be controlled by variety of techniques available to the colloidal synthesis such as variation of temperature, ligands, solvents etc.[53] Then the NCs of desired shapes and sizes can be dispersed in suitable solvents. The critical step is the purification of the NCs to remove

excess precursors and ligands, before integration into devices, as these residues may cause PL quenching and electrical injection barriers, respectively. This typically involves multiple centrifugation steps and use of polar solvents that can remove the excess ligands. However, perovskites are unstable in polar solvents. Hence, alternative purification methods to remove the synthesis residues, and/or synthesis protocols which can produce NCs in which the injection barrier from the ligands can be overcome, are required.

The first LED devices based on colloidally synthesized perovskite NCs were reported by Schmidt et al, based on $CH_3NH_3PbBr_3$ NCs. Later, Huang et al demonstrated an emulsion synthesis of perovskite $CH_3NH_3PbBr_3$ NCs whereby the NCs could be purified by a controlled demulsion process to achieve EL with 1.1% EQE and a maximum brightness of ~2500 cd $m^{-2}$.[54] Ling et al reported LEDs based on $CH_3NH_3PbBr_3$ nanoplatelets which gave > 10,000 cd $m^{-2}$ luminance, albeit at 0.48% EQE.[55] Xing et al achieved a 3.8% EQE from perovskite film formed from amorphous $CH_3NH_3PbBr_3$ nanoparticles which exhibited lower non-radiative decay compared to polycrystalline $CH_3NH_3PbBr_3$ films.[56] The colloidal NC synthesis approach was also applied to $CH(NH_2)_2PbBr_3$ NCs, and luminance of ~2700 cd $m^{-2}$ was obtained.[57]

In the above examples, octylamine was used as the ligand which is known to provide sufficient surface passivation without hindering the electrical injection. Hence, purification by centrifugation was sufficient to enable charge injection and other aspects such as film morphology and suppression of non-radiative recombination pathways need to be investigated to further improve the device performances. In contrast, for the fully inorganic perovskites, the colloidal NC synthesis involves highly insulating oleate precursors and oleylamine ligands. These form very good quality NCs with high color purity across the visible spectrum,[58] but purification steps using polar solvents are essential for good electrical injection. An EQE of 6.27% was achieved for $CsPbBr_3$ NCs by two

cycles of purification using hexane/ethyl acetate mixed solvent.[59] Further solvent treatment reduced the photoluminescence quantum yield (PLQY) and ink stability, emphasizing the need for proper control of ligand density to achieve high device efficiency.

## 2.6 Scope for Perovskite-based LEDs and Issues to be Addressed

Perovskite-based LEDs have exhibited phenomenal improvements in device efficiency, like the perovskite photovoltaics. Nevertheless, they haven't yet attained the 20% efficiency required for commercial viability. So, investigations to enhance the efficiency of perovskite-based LEDs are still very important.

In comparison to the already commercialized OLEDs and QLEDs, the material costs for perovskites are lesser than the expensive organic light emitters and the complicated core-shell structured QDs.[60] Moreover, perovskite LEDs show comparable (at some wavelengths, better), spectral purity than QLEDs. For QLEDs, the color tuning is due to the size-dependent quantum confinement in semiconductor nanoparticles. As the size is reduced, bang gap increases and the emission wavelength blue shifts. Hence, the spectral purity is critically dependent on the size distribution of the QDs. Among the QDs emitting in the visible range, red QDs, being the biggest in size, can tolerate more size variation without compromising the color quality, compared to the blue and green QDs.[61] In contrast, as the perovskites can be efficiently color tuned by halide composition, they are relatively size independent. Particularly, the green perovskite-based LEDs have shown very promising spectral intensities and color purity. In fact, use of the green light emitting perovskites as a phosphor in white light emitting diodes is proposed to be a good entry point for perovskites in to the LED market, albeit only as photoluminescent (not electroluminescent) material.

To manufacture large-area devices, the colloidal NC synthesis approach is easier for integration with existing OLED and QLED technologies. The pre-formed NC ink can be easily conveniently deposited on different substrates. It is also compatible with the printing techniques used in the flexible and large area devices. In contrast, in the direct thin film crystallization approach, the crystallization and surface coverage are highly substrate dependent.[38] Moreover, the precise control of the deposition conditions, such as anti-solvent dripping at specific times and thermal/ vacuum drying of the films, complicates the film formation step. Hence, the pre-formed NC ink deposition may be the simpler route for large-scale applications.

One major concern for the halide perovskite research in general is that the high-performance materials are based on lead, which is known to be highly toxic. Hence, the feasibility of replacing lead with less toxic elements such as tin, bismuth, antimony, etc., is under investigation by many research groups. Tin-based LEDs with luminance in the near infrared (IR) and red regime have been reported,[62,63] of which only the near IR emission have achieved a promising EQE of 3.8%.[62] Efficient EL from lead-free perovskites in the visible light regime is yet to be achieved.

The elephant in the room is the instability of perovskites. The low formation energies of perovskites, which enable the formation of high quality crystals from facile solution processing techniques, itself forms the bottle neck for the progress of perovskite-based applications. The material is sensitive to several external factors – degradation when exposed to air and water, and ion migration under electric and thermal stress, being the main concerns for the LED application. Electrically insulating polymers are commonly employed as interfacial layer or made to form perovskite-polymer composites to tackle both issues. However, it is difficult to achieve high efficiencies using this method, because the electrical injection is hampered by the insulating polymers. Hence, polymer-free

approaches to improve the device stability need to be investigated. Use of fully inorganic perovskites, with higher thermal and moisture stability than the hybrid organic inorganic perovskites, is also a highly-researched area. However, efficiency-wise, the hybrid perovskites consistently outperform the fully inorganic perovskites. In addition, the choice of transport layers can also significantly affect the thermal and electrical stability as well as the environmental exposure of the perovskite layer. A proper choice of transport layers, with balanced injection and good heat dissipation can significantly improve the overall device stability (further discussed in Chapter 7).

In this thesis, I have attempted to investigate factors influencing the efficiency and stability of perovskite-based LEDs from the emitter layer perspective. The investigations focus on the emitter layer, formed by the pre-formed NC ink deposition technique, which has more potential for commercial viability than the direct thin film crystallization approach. Also, the 3D organic-inorganic lead bromide perovskites which have shown highest efficiencies for perovskites to-date, was chosen as the system of study, for this project.

## 2.7 References

1 Chen, Q. *et al.* Under the spotlight: The organic–inorganic hybrid halide perovskite for optoelectronic applications. *Nano Today* **10**, 355-396, doi:10.1016/j.nantod.2015.04.009 (2015).

2 Goldschmidt, V. M. Die Gesetze der Krystallochemie. *Naturwissenschaften* **14**, 477-485, doi:10.1007/bf01507527 (1926).

3 Peña, M. A. & Fierro, J. L. G. Chemical Structures and Performance of Perovskite Oxides. *Chemical Reviews* **101**, 1981-2018, doi:10.1021/cr980129f (2001).

4 Zhu, J. *et al.* Perovskite Oxides: Preparation, Characterizations, and Applications in Heterogeneous Catalysis. *ACS Catalysis* **4**, 2917-2940, doi:10.1021/cs500606g (2014).

5 Jaffe, B., Cook, W. R. & Jaffe, H. L. *Piezoelectric ceramics*. (Marietta, Ohio : R.A.N. Publishers, [1990], ©1971., 1990).

6 Cohen, R. E. Origin of ferroelectricity in perovskite oxides. *Nature* **358**, 136-138 (1992).

7 Maeno, Y. *et al.* Superconductivity in a layered perovskite without copper. *Nature* **372**, 532-534 (1994).

8 Kaplan, T. & Mahanti, S. *Physics of manganites*. (Springer Science & Business Media, 2006).

9 Green, M. A. *et al.* Solar cell efficiency tables (version 50). *Progress in Photovoltaics: Research and Applications* **25**, 668-676, doi:10.1002/pip.2909 (2017).

10 MØLLER, C. K. Crystal structure and photoconductivity of caesium plumbohalides. *Nature* **182**, 1436-1436 (1958).

11 Kieslich, G., Sun, S. & Cheetham, A. K. Solid-state principles applied to organic-inorganic perovskites: new tricks for an old dog. *Chemical Science* **5**, 4712-4715, doi:10.1039/C4SC02211D (2014).

12 Mitzi, D. B. Templating and structural engineering in organic-inorganic perovskites. *Journal of the Chemical Society, Dalton Transactions*, 1-12, doi:10.1039/B007070J (2001).

13 Park, N.-G. Nonstoichiometric Adduct Approach for High-Efficiency Perovskite Solar Cells. *Inorganic Chemistry* **56**, 3-10, doi:10.1021/acs.inorgchem.6b01294 (2017).

14 Yang, W. S. *et al.* High-performance photovoltaic perovskite layers fabricated through intramolecular exchange. *Science* **348**, 1234-1237, doi:10.1126/science.aaa9272 (2015).

15 Weber, D. $CH_3NH_3PbX_3$, ein Pb (II)-system mit kubischer perowskitstruktur/$CH_3NH_3PbX_3$, a Pb (II)-system with cubic perovskite structure. *Zeitschrift für Naturforschung B* **33**, 1443-1445 (1978).

16 Ishihara, T. in *Optical Properties of Low-Dimensional Materials* 288-339 (World Scientific, 1996).

17 Ishihara, T., Takahashi, J. & Goto, T. Exciton state in two-dimensional perovskite semiconductor $(C_{10}H_{21}NH_3)_2PbI_4$. *Solid State Communications* **69**, 933-936, doi:10.1016/0038-1098(89)90935-6 (1989).

18 Ishihara, T. Optical properties of PbI-based perovskite structures. *Journal of Luminescence* **60**, 269-274, doi:10.1016/0022-2313(94)90145-7 (1994).

19 Papavassiliou, G. C. Synthetic Three-and Lower-Dimensional Semiconductors Based on Inorganic Units. *Molecular Crystals and Liquid Crystals Science and Technology. Section A. Molecular Crystals and Liquid Crystals* **286**, 231-238, doi:10.1080/10587259608042291 (1996).

20 Teruya, I., Masakatsu, H. & Takenari, G. Optical Properties and Electronic Structures of Self-Organized Quantum Well $(C_nH_{2n+1}NH_3)_2PbX_4$ (X=I, Br, Cl). *Japanese Journal of Applied Physics* **34**, 71 (1995).

21 Mitzi, D. B. Synthesis, Crystal Structure, and Optical and Thermal Properties of $(C_4H_9NH_3)_2MI_4$ (M = Ge, Sn, Pb). *Chemistry of Materials* **8**, 791-800, doi:10.1021/cm9505097 (1996).

22 Hong, X., Ishihara, T. & Nurmikko, A. V. Photoconductivity and electroluminescence in lead iodide based natural quantum well structures. *Solid State Communications* **84**, 657-661, doi:10.1016/0038-1098(92)90210-Z (1992).

23 Era, M., Morimoto, S., Tsutsui, T. & Saito, S. Organic - inorganic heterostructure electroluminescent device using a layered perovskite

semiconductor $(C_6H_5C_2H_4NH_3)_2PbI_4$. *Applied Physics Letters* **65**, 676-678, doi:10.1063/1.112265 (1994).

24 Hattori, T., Taira, T., Era, M., Tsutsui, T. & Saito, S. Highly efficient electroluminescence from a heterostructure device combined with emissive layered-perovskite and an electron-transporting organic compound. *Chemical Physics Letters* **254**, 103-108, doi:10.1016/0009-2614(96)00310-7 (1996).

25 Chondroudis, K. & Mitzi, D. B. Electroluminescence from an Organic−Inorganic Perovskite Incorporating a Quaterthiophene Dye within Lead Halide Perovskite Layers. *Chemistry of Materials* **11**, 3028-3030, doi:10.1021/cm990561t (1999).

26 Tan, Z.-K. *et al.* Bright light-emitting diodes based on organometal halide perovskite. *Nature Nanotechnology* **9**, 687-692, doi:10.1038/nnano.2014.149 (2014).

27 Kojima, A., Teshima, K., Shirai, Y. & Miyasaka, T. Organometal Halide Perovskites as Visible-Light Sensitizers for Photovoltaic Cells. *Journal of the American Chemical Society* **131**, 6050-6051, doi:10.1021/ja809598r (2009).

28 Im, J.-H., Lee, C.-R., Lee, J.-W., Park, S.-W. & Park, N.-G. 6.5% efficient perovskite quantum-dot-sensitized solar cell. *Nanoscale* **3**, 4088-4093, doi:10.1039/C1NR10867K (2011).

29 Lee, M. M., Teuscher, J., Miyasaka, T., Murakami, T. N. & Snaith, H. J. Efficient hybrid solar cells based on meso-superstructured organometal halide perovskites. *Science* **338**, 643-647, doi:10.1126/science.1228604 (2012).

30 Kim, H.-S. *et al.* Lead Iodide Perovskite Sensitized All-Solid-State Submicron Thin Film Mesoscopic Solar Cell with Efficiency Exceeding 9%. *Scientific Reports* **2**, 591, doi:10.1038/srep00591 (2012).

31 Veldhuis, S. A. *et al.* Perovskite Materials for Light-Emitting Diodes and Lasers. *Advanced Materials* **28**, 6804-6834, doi:10.1002/adma.201600669 (2016).

32 Kim, Y.-H., Cho, H. & Lee, T.-W. Metal halide perovskite light emitters. *Proceedings of the National Academy of Sciences* **113**, 11694-11702, doi:10.1073/pnas.1607471113 (2016).

33 Tress, W. Metal Halide Perovskites as Mixed Electronic–Ionic Conductors: Challenges and Opportunities—From Hysteresis to Memristivity. *The Journal of Physical Chemistry Letters* **8**, 3106-3114, doi:10.1021/acs.jpclett.7b00975 (2017).

34 Chin, X. Y., Cortecchia, D., Yin, J., Bruno, A. & Soci, C. Lead iodide perovskite light-emitting field-effect transistor. *Nature Communications* **6**, 7383, doi:10.1038/ncomms8383 (2015).

35 Xing, G. *et al.* Long-Range Balanced Electron- and Hole-Transport Lengths in Organic-Inorganic $CH_3NH_3PbI_3$. *Science* **342**, 344-347, doi:10.1126/science.1243167 (2013).

36 De Wolf, S. *et al.* Organometallic Halide Perovskites: Sharp Optical Absorption Edge and Its Relation to Photovoltaic Performance. *The Journal of Physical Chemistry Letters* **5**, 1035-1039, doi:10.1021/jz500279b (2014).

37 Snaith, H. J. Perovskites: The Emergence of a New Era for Low-Cost, High-Efficiency Solar Cells. *The Journal of Physical Chemistry Letters* **4**, 3623-3630, doi:10.1021/jz4020162 (2013).

38 Di Giacomo, F., Fakharuddin, A., Jose, R. & Brown, T. M. Progress, challenges and perspectives in flexible perovskite solar cells. *Energy & Environmental Science* **9**, 3007-3035, doi:10.1039/C6EE01137C (2016).

39 Li, G. *et al.* Efficient Light-Emitting Diodes Based on Nanocrystalline Perovskite in a Dielectric Polymer Matrix. *Nano Letters* **15**, 2640-2644, doi:10.1021/acs.nanolett.5b00235 (2015).

40 Li, J., Bade, S. G. R., Shan, X. & Yu, Z. Single-Layer Light-Emitting Diodes Using Organometal Halide Perovskite/Poly(ethylene oxide) Composite Thin Films. *Advanced Materials* **27**, 5196-5202, doi:10.1002/adma.201502490 (2015).

41 Bade, S. G. R. *et al.* Fully Printed Halide Perovskite Light-Emitting Diodes with Silver Nanowire Electrodes. *ACS Nano* **10**, 1795-1801, doi:10.1021/acsnano.5b07506 (2016).

42 Yantara, N. *et al.* Inorganic Halide Perovskites for Efficient Light-Emitting Diodes. *The Journal of Physical Chemistry Letters* **6**, 4360-4364, doi:10.1021/acs.jpclett.5b02011 (2015).

43 Li, J. *et al.* Single-Layer Halide Perovskite Light-Emitting Diodes with Sub-Band Gap Turn-On Voltage and High Brightness. *The Journal of Physical Chemistry Letters*, 4059-4066, doi:10.1021/acs.jpclett.6b01942 (2016).

44 Cho, H. *et al.* Overcoming the electroluminescence efficiency limitations of perovskite light-emitting diodes. *Science* **350**, 1222-1225, doi:10.1126/science.aad1818 (2015).

45 Xiao, Z. *et al.* Efficient perovskite light-emitting diodes featuring nanometre-sized crystallites. *Nature Photonics* **11**, 108-115, doi:10.1038/nphoton.2016.269 (2017).

46 Zhao, L. *et al.* In Situ Preparation of Metal Halide Perovskite Nanocrystal Thin Films for Improved Light-Emitting Devices. *ACS Nano*, doi:10.1021/acsnano.7b00404 (2017).

47 Lee, J.-W. *et al.* In-Situ Formed Type I Nanocrystalline Perovskite Film for Highly Efficient Light-Emitting Diode. *ACS Nano* **11**, 3311-3319, doi:10.1021/acsnano.7b00608 (2017).

48 Byun, J. *et al.* Efficient Visible Quasi-2D Perovskite Light-Emitting Diodes. *Advanced Materials* **28**, 7515-7520, doi:10.1002/adma.201601369 (2016).

49 Quan, L. N. *et al.* Tailoring the Energy Landscape in Quasi-2D Halide Perovskites Enables Efficient Green-Light Emission. *Nano Letters* **17**, 3701-3709, doi:10.1021/acs.nanolett.7b00976 (2017).

50 Zhang, X. *et al.* Hybrid Perovskite Light-Emitting Diodes Based on Perovskite Nanocrystals with Organic–Inorganic Mixed Cations. *Advanced Materials* **29**, 1606405(1606401-1606407), doi:10.1002/adma.201606405 (2017).

51 Kim, H. P. *et al.* High-Efficiency, Blue, Green, and Near-Infrared Light-Emitting Diodes Based on Triple Cation Perovskite. *Advanced Optical Materials* **5**, 1600920(1600921-1600929), doi:10.1002/adom.201600920 (2017).

52 Owen, J. The coordination chemistry of nanocrystal surfaces. *Science* **347**, 615-616, doi:10.1126/science.1259924 (2015).

53 Bai, S., Yuan, Z. & Gao, F. Colloidal metal halide perovskite nanocrystals: synthesis, characterization, and applications. *Journal of Materials Chemistry C* **4**, 3898-3904, doi:10.1039/C5TC04116C (2016).

54 Huang, H. *et al.* Emulsion Synthesis of Size-Tunable $CH_3NH_3PbBr_3$ Quantum Dots: An Alternative Route toward Efficient Light-Emitting Diodes. *ACS Applied Materials & Interfaces* **7**, 28128-28133, doi:10.1021/acsami.5b10373 (2015).

55 Ling, Y. *et al.* Bright Light-Emitting Diodes Based on Organometal Halide Perovskite Nanoplatelets. *Advanced Materials* **28**, 305-311, doi:10.1002/adma.201503954 (2016).

56 Xing, J. *et al.* High-Efficiency Light-Emitting Diodes of Organometal Halide Perovskite Amorphous Nanoparticles. *ACS Nano* **10**, 6623-6630, doi:10.1021/acsnano.6b01540 (2016).

57 Perumal, A. *et al.* High brightness formamidinium lead bromide perovskite nanocrystal light emitting devices. *Scientific Reports* **6**, 36733, doi:10.1038/srep36733 (2016).

58 Protesescu, L. *et al.* Nanocrystals of Cesium Lead Halide Perovskites ($CsPbX_3$, X = Cl, Br, and I): Novel Optoelectronic Materials Showing Bright Emission with Wide Color Gamut. *Nano Letters* **15**, 3692-3696, doi:10.1021/nl5048779 (2015).

59 Li, J. *et al.* 50-Fold EQE Improvement up to 6.27% of Solution-Processed All-Inorganic Perovskite $CsPbBr_3$ QLEDs via Surface Ligand Density Control. *Advanced Materials* **29**, 1603885(1603881-1603889), doi:10.1002/adma.201603885 (2017).

60 Li, G., Price, M. & Deschler, F. Research Update: Challenges for high-efficiency hybrid lead-halide perovskite LEDs and the path towards electrically pumped lasing. *APL Materials* **4**, 091507, doi:10.1063/1.4962351 (2016).

61 Dong, Y., Chen, H., He, J. & Wu, S.-T. Emerging Solution-Processable Luminescent Nanomaterials in Hybrid Structures Offer New Solutions for Displays and Lighting. *Information Display* **2**, 6-14 (2017).

62 Hong, W.-L. *et al.* Efficient Low-Temperature Solution-Processed Lead-Free Perovskite Infrared Light-Emitting Diodes. *Advanced Materials* **28**, 8029-8036, doi:10.1002/adma.201601024 (2016).

63 Lai, M. L. *et al.* Tunable Near-Infrared Luminescence in Tin Halide Perovskite Devices. *The Journal of Physical Chemistry Letters* **7**, 2653-2658, doi:10.1021/acs.jpclett.6b01047 (2016).

# Chapter 3

# Experimental Methodology

*Fundamentals of the colloidal synthesis of organic-inorganic hybrid perovskite nanocrystals by ligand assisted re-precipitation (LARP) are discussed, with a justification why this approach was chosen. The underlying principles of various characterization techniques, used to study the nanocrystals in solution and thin film, are discussed in detail, highlighting the scope and limitations of each technique. The fabrication of light-emitting diodes and their subsequent performance evaluation are also discussed.*

## 3.1 Rationale for Method Selection

The highest efficiency for perovskite-based LEDs to-date have been achieved by creating nanocrystal architectures using elaborate protocols during the solution deposition of the perovskite active layer.[1-3] To achieve these specific nano-grained architectures, judicious control over processing steps are prerequisite for high efficiencies. For example, anti-solvent dripping at precise timing, use of additional organic molecules in either the precursor solution or the anti-solvent and thermal or vacuum annealing for specific periods to remove the excess high boiling point solvents, ultimately limiting the control over thin film uniformity and process reproducibility. Decoupling the perovskite NC synthesis from the subsequent thin film formation, however, would allow better control over crystal size and film thickness, thus potentially aid fabrication reproducibility, thus opening opportunities to scale up device fabrication. Hence, a colloidal NC synthesis approach was used in this project to prepare NC inks. The inks can be directly spin coated to form the active emitter layer of the LED, without any additional solvent engineering, thus significantly simplifying the device fabrication process.

## 3.2 $CH_3NH_3PbBr_3$ NC Synthesis – Ligand-assisted Re-precipitation

The $CH_3NH_3PbBr_3$ NCs are synthesized at room temperature and under ambient conditions by a ligand-assisted re-precipitation (LARP) protocol.[4] The technique requires two solvents which are miscible with each other but have difference in solubility with respect to the precursor materials to induce precipitation or nucleation of nanoparticles, as well as ligands to control the NC growth and stabilize the solution. In this case, a polar solvent (‘good solvent’) like dimethylformamide (DMF) or dimethylsulfoxide (DMSO) are used to dissolve the methylammonium bromide ($CH_3NH_3Br$) and lead bromide ($PbBr_2$) precursor salts to form a transparent solution (referred to as precursor solution). A non-

polar solvent (‘poor solvent’ or ‘anti-solvent’) like e.g. toluene, diethylether, hexane, etc. - which is miscible with DMF - is used to precipitate the NCs. Long carbon chain aliphatic amines and carboxylic acids are chosen as ligands that bind to the $CH_3NH_3PbBr_3$ NCs. It is postulated that the amine group forms an aliphatic ammonium bromide compound, whereby the ammonium cation binds to the surface bromide, presumably through a hydrogen bridge, and the bromide anion binds to the surface cations.[5] The carboxylic acid is assumed to bind, not directly to the NCs, but via a reaction with amines to form alkoxy groups, which then bind to the NCs similar to the ammonium bromide ligands.[5] The ligands further prevent NC aggregation and help improve the colloidal stability. Concurrently, they enhance the radiative recombination in the NCs through passivation of the lower coordination surface atoms.[6]

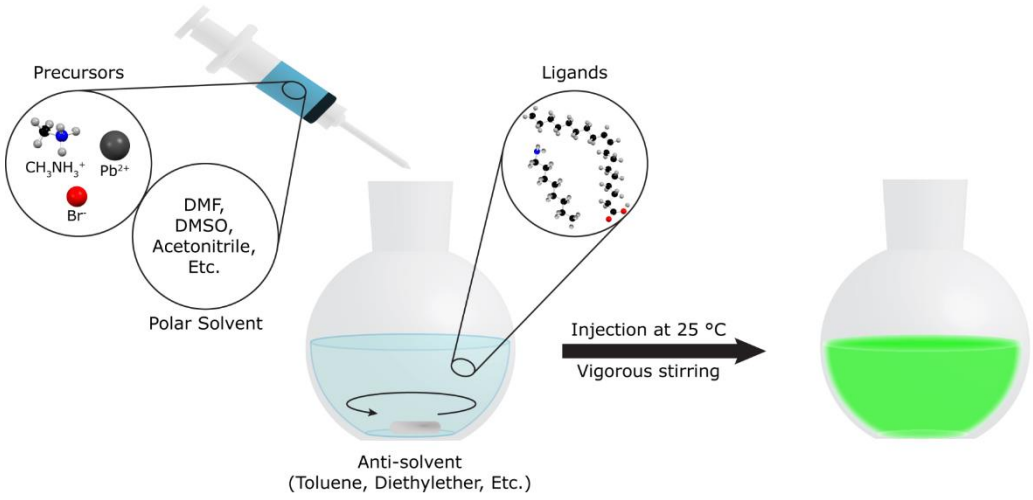


**Figure 3.1** Schematic illustrating the LARP synthesis protocol used in this thesis.

A schematic of the LARP protocol is presented in Figure 3.1. As illustrated, the precursor solution is injected into a vigorously stirring solution containing ‘poor solvent’ toluene and surface ligands. Upon addition, an immediate color change from transparent to greenish yellow is observed, indicating the formation of $CH_3NH_3PbBr_3$ NCs. The NCs are then purified by a two-step purification process to remove excess precursors and/or excess ligands as well as to obtain

luminescent NCs with a narrow size distribution. Firstly, the colloidal solution is centrifuged at high speeds to precipitate the $CH_3NH_3PbBr_3$ particles (dark yellow precipitate, which contains particles of different sizes) and remove the excess reagents retained in the supernatant. The obtained precipitate phase is then re-dispersed in fixed quantities of fresh toluene, and centrifuged at lower speeds. Here, the larger particles settle down and the smaller NCs remain in the solution, yielding a highly luminescent, green colored, supernatant phase. The supernatant is used as NC ink for all further characterizations and LED fabrication. The concentration of the NC ink is estimated by vacuum drying the solvent. In detail, a known volume of the NC ink is kept in a vacuum oven overnight at room temperature to remove toluene completely. The difference in weight, before and after solvent drying, gives the weight of the NCs. As the ink volume is known, an approximate ink concentration can be calculated.

As the name implies, the ligands play a crucial role in the LARP protocol. Besides stabilization of the colloidal solution and NC surface passivation, ligands play a key role in controlling the growth of the nanoparticles and thereby its size, shape and dimensionality. For example, during the $CsPbBr_3$ NC synthesis, a change of ligand from oleylamine ($C_{18}$) to *n*-octylamine ($C_8$) changed the NC shape from nanocube to nanoplatelet. In addition, if the carbon chain length of the carboxylic acid was varied (for a fixed aliphatic amine), the size of the NC changed while maintaining its original shape.[7] Moreover, the electrical properties of the NCs are influenced by the amount and type of ligands bound to the NCs. For example, long carbon chain ligands like oleylamine provide good surface passivation and thereby higher PLQYs;[7] however, they are also generally insulating in nature. Hence, they may inhibit the electrical injection into the perovskite layer, essential for efficient electroluminescence.

To improve the performance of perovskites NC-based LEDs, a balance between surface passivation and electrical injection is therefore required. Due to the ionic

nature of the NCs and consequently the ionic ligand binding, the ligands are easily removed by polar solvents.[5] So, use of purification protocols which involve slightly polar solvents can help control the ligand density.[8] However, usage of such solvents in large quantities may remove ligands excessively and even degrade the structural integrity of the NCs. Alternatively, one can employ shorter carbon chain ligands, which may reduce its insulating nature, albeit at the cost of reduced colloidal stability and surface passivation. Octylamine is known to provide a good balance between surface passivation and charge transport,[9] hence I used this aliphatic amine for all syntheses described in this project.

## 3.3 Characterization of the NC Inks and Films: Principles and Analysis

### 3.3.1 X-Ray Diffraction

X-ray diffraction (XRD) works on the principle that the regularly spaced atoms in crystals or crystal lattices can act as scattering centers for X-rays, as the wavelength of X-rays are of the same order as the interatomic distance in crystals.[10] A system, in which long-range order exists, the scattered rays constructively interfere to form diffraction beams. By using X-rays of known wavelengths, $\lambda$, and measuring the angle between diffracted beam and transmitted beam, $2\theta$ (in degrees), one can determine the spacing of various atomic planes in a crystal, $d$, as per the Bragg law (Figure 3.2),

$$2d \sin\theta = n\lambda. \quad (3.1)$$

The method is applicable only for solid crystalline samples, wherein atoms are periodically arranged, which result in diffraction peaks corresponding to the lattice spacing. For amorphous materials, due to the random arrangement of atoms and lack of long-range order, only destructive interference occurs and no clear patterns are discernible.

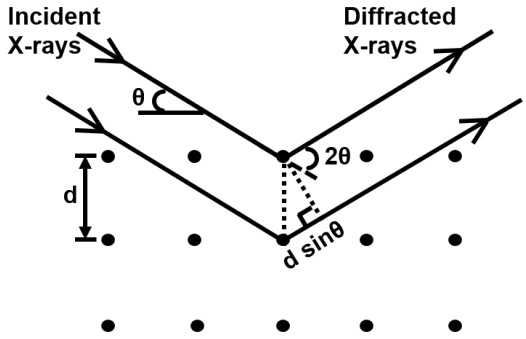


**Figure 3.2** Schematic depicting Bragg's law of X-ray diffraction.

The X-ray diffractograms are used to identify the crystal symmetry of a material. The diffraction peaks may broaden due to presence of nanocrystallites as well as strain in the crystal structure. The two types of peak broadening can be separately identified by use of either the Williamson-Hall plot (an approximate, but more facile method),[11] or Warren Averbach method (more accurate, but complex technique).[12,13] In case of NC size-related peak broadening, the mean size of the crystallite domains ($\tau$) in a polycrystalline sample can be estimated by applying the Scherrer equation,

$$\tau = \frac{K\lambda}{\beta \cos\theta} \tag{3.2}$$

where $K$ refers to a dimensionless shape factor with a typical value of 0.9, $\beta$ refers to the broadening of the diffraction peak minus the instrumental broadening, calculated in radians ($radians = degree \times \frac{180}{\pi}$), and $\theta$ refers to the Bragg diffraction angle (in degrees).

In this project, X-ray diffraction was applied to (1) verify that the synthesized NCs show the typical cubic perovskite crystal structure and lattice parameters, (2) investigate whether the changes introduced in the NC synthesis lead to the formation of any (unwanted) secondary phases, and (3) estimate the crystallite sizes of the synthesized NCs. Typical measurements were performed using a Bruker Advance D8 diffractometer with Cu Kα radiation, Göbel mirror configuration, and 0.02 rad Soller slit. NC samples were prepared by drop casting

the NC ink on glass substrates (solvent evaporation at room temperature). The samples were measured from 2θ = 5-60° with step sizes of 0.02° and 0.5 s per step under a fixed theta value of 1°.

### 3.3.2 Small-angle X-ray Scattering (SAXS)

Small-angle x-ray scattering is a form of diffuse scattering at angles close to the transmitted beam (scattering angle, $2\theta$ = 0° to 2°, normally). The variation of the scattering intensity, $I(q)$ (where $q$ is magnitude of the scattering vector) with respect to the $2\theta$ value is analyzed to determine the size and shape of particles, up to 100 nm in size.[14] $I(q)$ can then be correlated to the scattering angle, and the wavelength ($\lambda$) of the incident beam through:

$$q = \frac{4\pi}{\lambda} \sin\theta \tag{3.3}$$

Since scattering does not rely on long-range order, both amorphous and crystalline samples and even liquids can be analysed using this technique.

The variations in scattering intensity arise from changes in local electron densities. Such density fluctuations could arise in a homogeneous suspension of nanocrystals (with electron density $\rho$) in a solvent matrix of different electron density, $\rho_0$ or due to porosity of particles. Electron interference, both intra-particular (within the nanocrystal) and inter-particular (between electrons in a particle assembly) can result in scattering. The scattering intensity is given by:

$$I(q) = N \cdot (\Delta p)^2 \cdot P(q) \cdot S(q) \tag{3.4}$$

where $N$ is the number density of particles, $\Delta\rho$ is the electron density difference between the particles and the solvent matrix ($(\Delta\rho)^2$ is the scattering contrast), $P(q)$ is the form factor and $S(q)$ is the structure factor. For dilute systems, $S(q)$ is assumed to be 1, as the particles are expected to be far enough to prevent inter-particular interference. For spherical particles, $P(q)$ is given by:

$$P(q, r_0) = \left[3\frac{\sin(q\cdot r_0) - q\cdot r_0\cdot\cos(q\cdot r_0)}{(q\cdot r_0)^3}\right]^2 \tag{3.5}$$

where $r_0$ is the radius of the smallest scattering particles. At high $q$ values ($q \cdot r_0 >> 1$), scattering from the small particles are observed, as per Porod's law, $I(q)\ \alpha\ q^{-4}$.[14] However, the scattering intensity is predominantly determined by the large particles or aggregates at low $q$ values, and is described by the Guinier approximation,[15]

$$I(q) = I_0 \cdot exp\left[-\frac{(q \cdot R_g)^2}{3}\right] (for\ q \to 0) \tag{3.6}$$

The radius of gyration, $R_g$, is defined as the root-mean square of the center-of-mass distances within a particle or an assembly of particles. It can be determined from the slope in a plot of $q^2$ vs ln $I(q)$; valid for $q \cdot R_g << 1$. $R_g$, can be related to the particle radius, $r$, as

$$R_g = \sqrt{\frac{3}{5}} \cdot r \tag{3.7}$$

Small angle scattering measurements were conducted using the Xenocs Nano-inXider, equipped with a Dectris Pilatus3 hybrid pixel detector. The effective scattering vector magnitude was in the range of $0.097 < q < 4.49$ nm$^{-1}$. Samples were measured in sealed glass capillaries (inner diameter 0.95 mm, length 100 mm) under vacuum at room temperature. Particle size distributions were obtained (form-free) from the scattering curves using the Monte Carlo based software package McSAS,[16] using a convergence criterion of 2, with 10 calculating repetitions, and 500 contributions.

### 3.3.3 Electron Microscopy

In electron microscopy, electrons accelerated at high voltages are used to image samples. Generally, electron beams have much smaller wavelength than e.g. visible light (for instance, an electron beam operating at 100 keV has a wavelength in the range of 3-4 pm); therefore, an image resolution of the order of nanometers can be achieved. Since electrons are charged particles, they can be focused using electric or magnetic fields, while sample scanning can be

performed by applying electrostatic fields. However, since the interaction of electrons with matter is very strong, the measurements require vacuum conditions of at least $10^{-4}$ Pa.[17] Two types of electron microscopy techniques were used in this thesis – scanning electron microscopy (SEM), which is mainly a surface technique based on scattering of electrons by the sample and transmission electron microscopy (TEM), which gives more in-depth information regarding the sample as it analyses the transmitted electrons.

#### 3.3.3.1 Scanning Electron Microscopy (SEM)

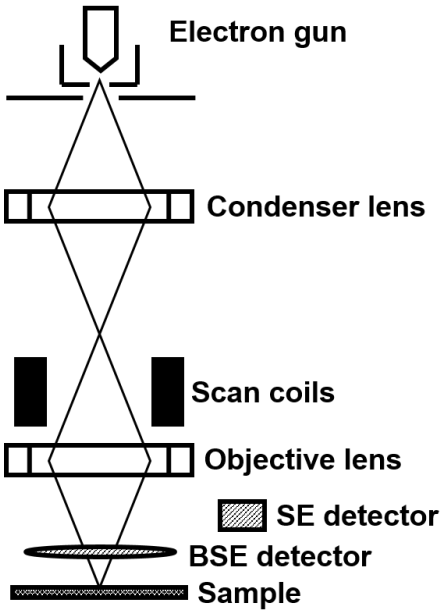


**Figure 3.3** Schematic diagram showing the basic parts and working of an SEM.

In SEM, signals produced from the interaction of the specimen's surface with a focused electron beam (1-20 kV) is utilized to gain insight into the surface topography and composition of NC thin films.[18] The schematic diagram of an SEM is shown in Figure 3.3. Scanning of the electron beam across the specimen's surface results in both elastic and inelastic scattering of the incident electrons, giving rise to a variety of signals. For example, secondary electrons (SE) of low energy, typically 3-5 eV, produced by inelastic scattering, are most commonly

used to provide topographical information with a resolution of 10 nm or better. Another extremely useful signal is obtained from the electrons scattered elastically by angles > 90° (back scattered electrons, BSE). The yield of such electrons is dependent on the atomic mass of the nucleus of the specimen atoms, for example, for a light element such as carbon, the back scattered electron yield is only ~6%, while for heavier elements like tungsten or gold it is almost 10 times higher. Hence, compositional contrast can be clearly observed in BSE images.

As the sample imaging is performed with the help of electrons, the samples need to be conductive to prevent charge accumulation. Hence, additional sample preparation is required for imaging of non-conductive samples to improve the sample surface conductivity. Typically, a thin layer of Pt or Au is sputter coated on top of the sample, while the sample is electrically grounded using thin strips of Cu tape.

In this project, SEM imaging is used to examine the surface coverage and morphology of the NC thin films (formed by spin-coating the NC ink). Top view images of the samples reveal the packing density and uniformity of the NC layer, and whether or not the NCs maintain their size/shape or aggregate after thin film formation. Cross sectional imaging of the samples helps to identify the NC layer thickness due to compositional contrast with the underlying layers. However, due to the organic-inorganic nature of the investigated samples, electron beam irradiation can easily damage the sample. Another implication is the comparable size of the synthesized NCs and the sputtered Pt nanoparticles, therefore, top view samples must be imaged without Pt sputtering to clearly observe the film morphology. Consequently, sample damage is severe and image resolution is low. So, high resolution imaging without use of electron beams would be preferable for surface topography imaging (e.g. AFM, see below) of the perovskite NCs.
SEM measurements were performed using a field-emission scanning electron microscopy (FESEM; Jeol 7600F) with an acceleration voltage of 5 kV. For

surface morphology studies, the perovskite layer was spin coated (1 min at 2000 rpm) on ITO/PEDOT:PSS and observed without any sputter coating. For determining the thickness, cross-section images of the ITO/PEDOT:PSS/ perovskite NC samples were captured. The samples for cross-section imaging were sputtered with Pt for 30 s at 30 mA prior to the microscopy studies.

#### 3.3.3.2 Transmission Electron Microscopy (TEM)

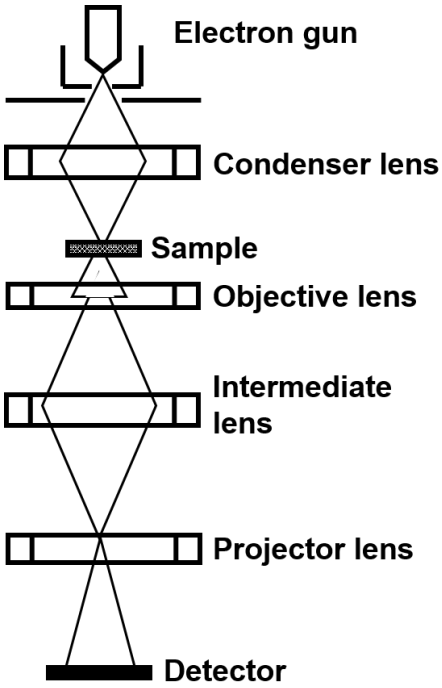


**Figure 3.4** Schematic diagram showing image formation in a TEM

In TEM, the electron beam is accelerated at much higher voltages than with SEM, typically 100-400 kV and the electrons transmitted through the sample are collected by the detector (schematic shown in Figure 3.4).[17] As significantly higher voltages are used, it provides higher image resolution, as well as deeper penetration of the electrons into the sample specimen. Similar to SEM, electronic conductivity of the sample is a prerequisite for TEM analysis. Typically, samples

are in the form of 3 mm diameter discs, up to a few hundred nanometers in thickness.

In addition to imaging, diffraction experiments can also be performed inside a TEM. Moreover, unlike XRD which is a bulk technique, herein selected NCs or small assemblies of NCs can be accurately examined. A sample area, with a diameter of approximately 0.1 μm, can be selected by a selected area diffraction aperture to obtain a selected area electron diffraction (SAED) pattern. The SAED pattern can provide structural details such as the phase and orientation of the sample.

For amorphous materials, diffuse diffraction rings are obtained which are associated with the average interatomic separations within the sample. Conversely, in crystalline materials wherein the atoms are periodically arranged, electrons are scattered through well-defined Bragg angles. Hence, the diffraction pattern for a single crystalline sample consists of points which are spaced at distances proportional to the inverse of lattice spacing and are aligned in a direction perpendicular to the reciprocal lattice plane. For polycrystalline materials, in which the crystallites are randomly oriented, the diffraction pattern consists of concentric rings of radii $r$ which are inversely proportional to the lattice spacing $d$. More specifically:

$$\frac{r}{L} = 2\theta = \frac{\lambda}{d} \tag{3.8}$$

where $\lambda$ is the wavelength of incident beam and $L$ is the camera length.

In this project, TEM was used to corroborate the NC size distribution obtained from SAXS measurement, to verify the shape of the NCs and to confirm its crystalline phase. The NC ink was drop casted on a Cu grid to ensure good conductivity. The ink was dried overnight in a dry box at < 30% relative humidity (RH). The images and diffraction patterns were recorded using a Jeol JEM-2010 microscope, operated at 200 kV.

### 3.3.4 Atomic Force Microscopy (AFM)

AFM is a surface probing technique used for topographical imaging of samples, mainly in the so-called AC mode or tapping mode. Briefly, a force probe, which is typically a Si cantilever (force constant >10 N $m^{-1}$),[19] with a sharp tip at one end, is oscillated at a frequency near to its resonant frequency (drive frequency). The amplitude and phase of the oscillation with respect to the drive signal is measured as it scans over the sample's surface.[20] Generally, a piezoelectric actuator oscillates the cantilever mechanically; a laser and a split photodiode are used to optically detect the cantilever deflection (Figure 3.5); and the imaging is performed in repulsive AC mode where the tip is in contact with the sample's surface only for a small fraction of time during its oscillation. Since there is very little contact between sample surface and probe tip, sample damage is minimal. In fact, for soft biological samples, a softer tip with smaller force constants and lower drive frequencies may be used for attractive mode scanning to prevent sample damage. However, for imaging in air, unavoidable surface contamination reduces the resolution in the attractive regime and the true surface topography is not obtained.[19] Hence, the AC repulsive mode is commonly preferred for surface imaging of samples measured under ambient conditions.

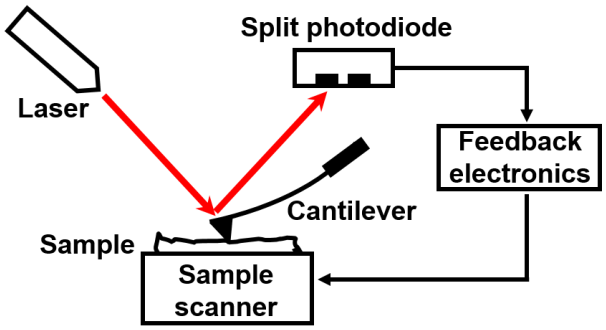


**Figure 3.5** Schematic depicting the different parts and working principle of an AFM

The main advantage of AFM is that it can be used for imaging both conductive and non-conducting samples, without significant sample degradation, at

nanometer scale resolution, and in ambient conditions. This is in contrast to electron microscopy, which is a destructive technique that can analyze only conductive samples in vacuum atmosphere.[21] Sub-nanometer vertical resolution and close to 1 nm lateral resolution can be obtained using AFM. However, the physical probing technique restricts the scan area to several tens of square micrometers and requires the sample roughness to be less than few micrometers.[22]

In this project, AFM was used to obtain surface morphology and roughness information of the nanocrystal thin films. The imaging was performed on spin coated samples using Asylum Research Cypher S, in repulsive AC mode using an Al-coated Si tip with a force constant of 42 N $m^{-1}$ and resonance frequency of 285 kHz. The height measurements are displayed using the color scheme violet orange yellow where violet is lower elevation and yellow is higher elevation.

### 3.3.5 Optical Spectroscopy

Electronic transitions between orbitals in the conduction and valence band of materials typically lie in the ultraviolet (UV), visible (Vis), and near infra-red (NIR) regions of the electromagnetic spectrum (200-900 nm). Hence, when UV-Vis-NIR radiations are used to excite the sample, the absorption (or transmittance), reflection, and emission of the these radiations give insight into a material's electronic band structure.[17]

These spectroscopic measurements can be of two types – steady-state and transient. In steady-state spectroscopy, the sample is irradiated by a continuous light source and the spectral signals are collected as a function of wavelength. For transient or time-resolved spectroscopies, a non-continuous light source, e.g. a pulsed laser, is used to obtain changes in the optical signals, as a function of delay time after the light pulse.

### 3.3.5.1 Steady-state Absorption Spectroscopy

In steady-state absorption spectroscopy, a sample is irradiated by a monochromatic beam from a continuous light source. The attenuation of beam intensity as it passes through the sample is measured over a range of incident wavelengths. The mathematical-physical basis for the measurements is given by the Bouguer-Lambert-Beer law:

$$\log\left(\frac{I_0}{I}\right)_\lambda = \log\left(\frac{100}{T(\%)}\right)_\lambda \equiv A_\lambda = \varepsilon_\lambda \cdot c \cdot d \qquad (3.9)$$

where $A_\lambda = \log\left(\frac{I_0}{I}\right)_\lambda$ is the absorbance, $T_\lambda = \left(\frac{I}{I_0}\right) \cdot 100$ (in %) is the transmittance, $\varepsilon_\lambda$ is the molar extinction coefficient, $I_0$ is the intensity of incident monochromatic beam, $I$ is the intensity of the transmitted beam, $c$ is the sample concentration and $d$ is the path length of the sample.[23] The equation is valid for dilute solutions where $\varepsilon_\lambda$ is independent of sample concentration. For concentrated solutions (> $10^{-2}$ mol $L^{-1}$), $\varepsilon_\lambda$ depends significantly on the refractive index of the solution and the linear relation between absorbance and sample concentration is no longer valid.

In this project, the steady state absorbance measurements were used to elucidate the optical band gap of the material from the absorption edge of the absorbance spectra.[24] Moreover, presence of excitons and/or mixed dimensional phases in the material can also be detected as peaks in the absorbance spectra. The absorbance measurements were performed using a Shimadzu UV-2550 spectrophotometer with an integrating sphere attachment (20 nm slit width, 0.5 nm resolution). The instrument has attachments for both thin film and liquid samples. The liquid samples were measured in quartz cuvettes. Toluene was used as reference and the inks were diluted more than 100 times for the spectroscopic measurements. Typically, 20 µL of the ink was added to 3 mL toluene ($c \approx .10^{-4}$ mol $L^{-1}$). For the thin film samples, the NC ink was spin coated under similar conditions as used for device fabrication so that optical properties could be

meaningfully correlated to the device performance.

#### 3.3.5.2 Steady-state Photoluminescence (PL)

In steady-state PL, samples are photoexcited at specific wavelengths, and the light scattered from the sample are collected by a photodetector.[17] The detector disperses the obtained spectra as function of wavelength and records the intensity at each wavelength. Photoluminescence excitation (PLE) spectroscopy, is a modification of this technique whereby the intensity of a single luminescence band (i.e. specific emission wavelength) is monitored while the excitation wavelength is varied. The PL and PLE measurements elucidate the types of radiative recombination occurring in the material. The PL peak position reveals the electronic states which contribute to the radiative recombination. The intensity of the emission serves as a magnitude of the radiative recombination in the material. The PLE indicates which electronic states are involved in absorption resulting in photoluminescence emission at a specific wavelength. This also gives insight into whether charge transfer is occurring within the luminescent material.

In this project, steady-state PL was used as a basic characterization tool to record the PL emission from the various NC thin films. PLE was used in conjunction with absorption spectroscopy to check for energy funneling within the thin film. The sample preparation conditions were the same as that for absorption spectroscopy measurements. The steady-state PL and PLE spectra of the $CH_3NH_3PbBr_3$ NCs were measured using a Horiba Fluoromax-4 spectrofluorometer with 0.4-0.5 nm band pass, excitation and emission front and back slits. An integration time of 0.1 s was used for the PL measurement, while a 0.2 nm band pass slits and integration time of 0.2 s were used for the excitation spectra. In order to compare the PL spectra of different samples, the PL emission was corrected for differences in the absorption of the sample at the wavelength of PL excitation to fairly compare the radiative recombination capability:

$$PL_{cor_{(\lambda_{ex})}} = PL_{(\lambda_{ex})}/(1 - (10^{-\varepsilon_\lambda})) \quad (3.10)$$

where $PL_{cor_{(\lambda_{ex})}}$ refers to the corrected PL intensity and the $PL_{(\lambda_{ex})}$ is the as-measured PL intensity at a particular excitation wavelength $\lambda_{ex}$. Typically, an excitation wavelength of 400 nm was used in this project.

#### 3.3.5.3 Time-resolved Photoluminescence (TRPL)

The time-resolved measurements give insight into the charge carrier dynamics in the material after excitation by an incident radiation pulse.[17] Herein, a pulsed-laser source is used to excite the sample and a single photon counter is used to detect the emitted light as a function of decay time. The radiative recombination, and hence the PL decay time, depend on the intrinsic diffusion lengths, exciton binding energies, as well as trap density in the material. For example, for perovskite single crystals with low trap density, the decay times of hundreds of ns are obtained.[25] On the other hand, in nanocrystals wherein excitons are spatially confined and surface traps are more dominant, the lifetimes are generally reduced to several to tens of ns.[26]

In this project, TRPL was used as one of the critical characterization tools to study the influence of variations in the synthesis protocol on the radiative recombination in the NC thin films. Additionally, the TRPL measurements were also performed at different wavelengths within the emission peak to comprehensively study the recombination behavior of differently sized NCs within the respective size distributions. The NC thin films were prepared by spin coating the NC inks on glass substrates (1 min at 1000 or 2000 rpm). A 405-nm laser source with low intensity excitation (~2 μJ $cm^{-2}$) was used to excite the samples. The PL signals were detected using a time-correlated single photon counter (TCSPC), with a resolution of 16 ps, and analyzed using the PicoQuant software package.

### 3.3.6 Photoelectron Spectroscopy

In photoelectron spectroscopy, solid samples are photo-excited and the kinetic energy of the electrons emitted from the samples are analyzed. Briefly, electrons are excited upon absorption of photons and if the photon energy is sufficiently high, electrons can escape from the material's surface into vacuum. While travelling to the surface, most electrons collide inelastically with other electrons and lose some part of their kinetic energy. The primary electrons, generated mostly from the outermost 10 nm of the sample surface, which do not undergo inelastic collisions with other electrons, result in distinct spectral features depending on the binding energy of the electron.

Typically, soft X-rays (200–2000 eV), commonly produced from Al or Mg anodes, are used as the excitation source for this spectroscopic technique, referred to as X-ray photoelectron spectroscopy (XPS) or electron spectroscopy for chemical analysis (ESCA).[27] The kinetic energy of the ejected electron, $KE_{XPS}$, electron binding energy, $BE_{XPS}$, and the incident photon energy, $E_{ph}$, are related as

$$KE_{XPS} = E_{ph} - \varphi_{XPS} - BE_{XPS} \quad (3.11)$$

where $\varphi_{XPS}$ is the work function of the instrument. The technique can detect the elemental composition as well as speciation of elements from Li to U with a sensitivity of concentrations up to 0.1 atomic percentage (sensitivity higher for higher atomic weight elements); however, a high vacuum ~$10^{-7}$ is required for the precise electron detection from the samples.[28]

For determining the work function, $\varphi$, (of metals) or valence band maxima (VBM) (of semiconductors), only the outer electrons need to be excited, hence UV radiation is used to excite the sample. This technique is called ultraviolet photoelectron spectroscopy (UPS) and the common excitation source in this case

is a He discharge lamp of either 21.2 eV or 40.8 eV emission.[29] The work function, $\varphi$, (or VBM) is determined as:

$$\varphi\ (or\ VBM) = h\nu - W \tag{3.12}$$

where $h\nu$ is the energy of the photon and $W$ is the width of the UPS spectrum.

Similar to XPS, UPS is generally conducted in a high vacuum environment to enable good electron detection. However, a method for the detection of the photoelectrons in atmospheric pressure is also available, whereby the electrons excited by an UV source is detected using an air-filled counter with two grids.[30] This technique is called photoelectron spectroscopy in air (PESA). Herein, the grids inside the air counter are made of a gold-plated stainless steel mesh. These grids protect the sample from the positive ions produced during discharge and quench the counter discharge caused by the incident electrons, thus enabling accurate detection of low-energy electrons emitted from the sample's surface.

In this thesis, XPS was used to determine the chemical composition of the NCs synthesized using different precursor stoichiometries. The NCs were spin coated as inks on conducting ITO substrates to form thin films. The films were then excited with a monochromatic Al K-α ($h\nu$ = 1486.7 eV) radiation source. The output signals were detected by an electron analyzer (Omicron, EA125) and the analyzer work function was calibrated using the Au Fermi edge. For the determination of VBM of the NCs, the ink was drop casted NC on ITO substrates. A Riken Photoelectron Spectrometer (Model AC-2) was used to perform the PESA measurements. The conduction band minima (CBM) were calculated by addition of VBM and the optical band gap obtained from absorbance measurements.

## 3.4 LED Fabrication and Testing

LEDs were fabricated following a multi-step process. Firstly, pre-etched indium tin oxide (ITO)-coated glass substrates (sheet resistance = 8 Ω $m^{-2}$) were cleaned sequentially in a soap solution, water, acetone, ethanol, and isopropyl alcohol, after which were these further cleaned by UV ozone for 15 min at 20 °C. The UV ozone also renders the top surface hydrophilic which would improve the wettability of the water-based hole transport layer (HTL), poly(3,4-ethylenedioxythiophene)-poly(styrenesulfonate) (PEDOT:PSS). Approximately 40 nm PEDOT:PSS was spin coated (1 min at 4000 rpm) on the substrate, followed by thermal annealing for 15 min at 130 °C to remove any water content. The substrates were then transferred to an Ar glove box, where the NC inks were spin coated (typically, 1 min at 1000 or 2000 rpm) on the as-deposited PEDOT:PSS layer.

Next, the spin coated films were transferred, without further heat treatment, to the evaporation chamber (within the Ar glove box) for thermal evaporation of the subsequent layers. Organic electron transport layer (ETL), either 4,6-bis(3,5-di(pyridin-3-yl)phenyl)-2-methylpyrimidine (B3PYMPM) or 2,4,6-Tris[3-(diphenylphosphinyl)phenyl]-1,3,5-triazine (PO-T2T) of thickness 45 nm, followed by 7 nm of Ca, and 80 -100 nm Al (cathodes) were sequentially deposited. The Ca serves as an interfacial layer to aid the electron transfer from Al to the lowest unoccupied molecular orbital (LUMO) level of the ETL. Finally, the resulting devices, with an active area of 3 $mm^2$, were encapsulated with glass using UV adhesive epoxy resin and characterized under ambient conditions (60% RH). The flat-band energy level diagram displaying the various layers in the LED device stack and a representative photograph of the fabricated device are depicted in Figure 3.6.

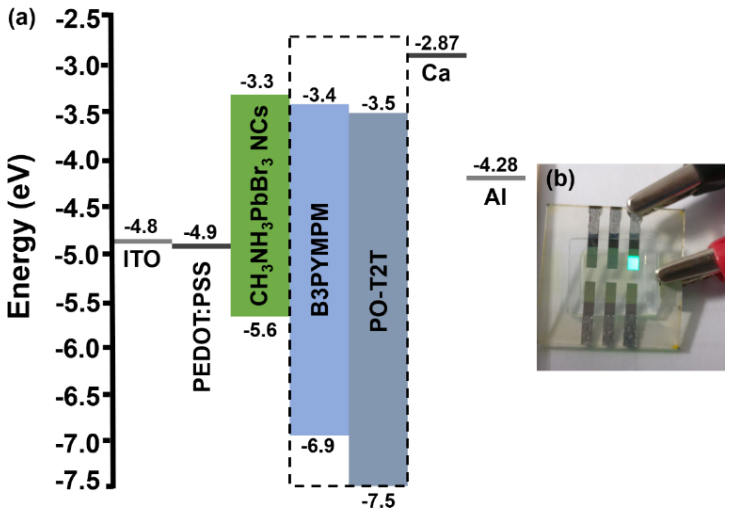


**Figure 3.6** (a) Flat-band energy level diagram of the various layers in the LED device stack. The values beside the energy levels represent the work function and highest occupied molecular orbital (HOMO)/LUMO of the respective layers. Either of the two electron transport layers (within the dashed rectangle) were used for LED fabrication. (b) Representative photograph of an encapsulated LED showing green emission.

The current-voltage characteristics of the devices were obtained using the Keithley 2612B as voltage source. Voltage sweeps were performed starting from -1.5 V until the luminance of the device started to drop; typically, close to 6 V. The light emission was collected by an integrating sphere (OceanOptics FOIS-1) coupled to a calibrated spectrophotometer (OceanOptics QEPro). The key parameters associated with the LED performance are described below. The external quantum efficiency (EQE), defined as the ratio of emitted photons to the number of electrons injected into the device which can be expressed as:

$$EQE = IQE \cdot \eta_{extraction} \tag{3.13}$$

where $\eta_{extraction}$ refers to the photons generated in the emitter layer that exit the device and the internal quantum efficiency, IQE, is defined as

$$IQE = \eta_{injection} \cdot \eta_{radiative} \tag{3.14}$$

where $\eta_{injection}$ is the proportion of electrons injected into the active emitter layer to the number of electrons passing through the device, and $\eta_{radiative}$ is the proportion of electron-hole recombinations that occur radiatively within the

emitter layer.[31] Other efficiency parameters commonly reported are the current efficiency (CE), which is defined as the ratio of the luminance to the current flowing in the device and power efficiency (PE), defined as the ratio of luminous flux to the power injected by the voltage source.

Lastly, to evaluate the stability of the LEDs, two types of measurements were performed: (1) constant-current operation – here, an initial voltage sweep was performed to determine the current required to obtain a luminance of approximately 100 cd $m^{-2}$. Subsequently, the current flowing through the LED was fixed to this value and changes in luminance were monitored until the luminance value dropped to half its initial value. (2) Multiple voltage sweeps from 1.5 V to a set value of 3 or 4 V (i.e. in the range where the luminance was still increasing). Here, changes in current and luminance were monitored concurrently. These measurements test the suitability of the devices for practical applications and help to identify the parameters that need further investigation to improve the device stability.

## 3.5 References

1 Cho, H. *et al.* Overcoming the electroluminescence efficiency limitations of perovskite light-emitting diodes. *Science* **350**, 1222-1225, doi:10.1126/science.aad1818 (2015).

2 Xiao, Z. *et al.* Efficient perovskite light-emitting diodes featuring nanometre-sized crystallites. *Nature Photonics* **11**, 108-115, doi:10.1038/nphoton.2016.269 (2017).

3 Lee, J.-W. *et al.* In-Situ Formed Type I Nanocrystalline Perovskite Film for Highly Efficient Light-Emitting Diode. *ACS Nano* **11**, 3311-3319, doi:10.1021/acsnano.7b00608 (2017).

4 Zhang, F. *et al.* Brightly Luminescent and Color-Tunable Colloidal $CH_3NH_3PbX_3$ (X = Br, I, Cl) Quantum Dots: Potential Alternatives for

Display Technology. *ACS Nano* **9**, 4533-4542, doi:10.1021/acsnano.5b01154 (2015).

5 De Roo, J. *et al.* Highly Dynamic Ligand Binding and Light Absorption Coefficient of Cesium Lead Bromide Perovskite Nanocrystals. *ACS Nano* **10**, 2071-2081, doi:10.1021/acsnano.5b06295 (2016).

6 Owen, J. The coordination chemistry of nanocrystal surfaces. *Science* **347**, 615-616, doi:10.1126/science.1259924 (2015).

7 Pan, A. *et al.* Insight into the Ligand-Mediated Synthesis of Colloidal $CsPbBr_3$ Perovskite Nanocrystals: The Role of Organic Acid, Base, and Cesium Precursors. *ACS Nano* **10**, 7943-7954, doi:10.1021/acsnano.6b03863 (2016).

8 Li, J. *et al.* 50-Fold EQE Improvement up to 6.27% of Solution-Processed All-Inorganic Perovskite $CsPbBr_3$ QLEDs via Surface Ligand Density Control. *Advanced Materials* **29**, 1603885(1603881-1603889), doi:10.1002/adma.201603885 (2017).

9 Bakueva, L. *et al.* Size-tunable infrared (1000–1600 nm) electroluminescence from PbS quantum-dot nanocrystals in a semiconducting polymer. *Applied Physics Letters* **82**, 2895-2897, doi:10.1063/1.1570940 (2003).

10 Cullity, B. D. & Stock, S. R. *Elements of x-ray diffraction*. (Upper Saddle River, NJ : Prentice Hall, c2001., 2001).

11 Williamson, G. K. & Hall, W. H. X-ray line broadening from filed aluminium and wolfram. *Acta Metallurgica* **1**, 22-31, doi:10.1016/0001-6160(53)90006-6 (1953).

12 Warren, B. E. & Averbach, B. L. The Separation of Cold‐Work Distortion and Particle Size Broadening in X‐Ray Patterns. *Journal of Applied Physics* **23**, 497-497, doi:10.1063/1.1702234 (1952).

13 Warren, B. E. & Averbach, B. L. The Effect of Cold‐Work Distortion on X‐Ray Patterns. *Journal of Applied Physics* **21**, 595-599, doi:10.1063/1.1699713 (1950).

14 Glatter, O. & Kratky, O. *Small angle X-ray scattering*. (Academic press, 1982).

15 Guiner, A., Fournet, G. & Walker, C. Small angle scattering of X-rays. *J. Wiley & Sons, New York* (1955).

16 Pauw, B. R., Pedersen, J. S., Tardif, S., Takata, M. & Iversen, B. B. Improvements and considerations for size distribution retrieval from small-angle scattering data by Monte Carlo methods. *Journal of Applied Crystallography* **46**, 365-371, doi:10.1107/S0021889813001295 (2013).

17 Kelsall, R., Hamley, I. W. & Geoghegan, M. *Nanoscale Science and Technology. [electronic resource]*. (Hoboken : John Wiley & Sons, Ltd., 2006., 2006).

18 Zhou, W., Apkarian, R., Wang, Z. L. & Joy, D. in *Scanning Microscopy for Nanotechnology: Techniques and Applications* (eds Weilie Zhou & Zhong Lin Wang) 1-40 (Springer New York, 2007).

19 Eaton, P. & West, P. *Atomic force microscopy*. (Oxford University Press, 2010).

20 Voigtländer, B. *Scanning Probe Microscopy. [electronic resource] : Atomic Force Microscopy and Scanning Tunneling Microscopy*. (Berlin, Heidelberg : Springer Berlin Heidelberg : Imprint: Springer, 2015., 2015).

21 Bandyopadhyay, S., Samudrala, S. K., Bhowmick, A. K. & Gupta, S. K. in *Functional Nanostructures: Processing, Characterization, and Applications* (ed Sudipta Seal) 504-568 (Springer New York, 2008).

22 Haugstad, G. in *Atomic Force Microscopy* 1-32 (John Wiley & Sons, Inc., 2012).

23 Perkampus, H.-H. *UV-VIS spectroscopy and its applications*. (Berlin ; New York : Springer-Verlag, c1992., 1992).

24 Tauc, J., Grigorovici, R. & Vancu, A. Optical properties and electronic structure of amorphous germanium. *physica status solidi (b)* **15**, 627-637 (1966).

25 Shi, D. *et al.* Low trap-state density and long carrier diffusion in organolead trihalide perovskite single crystals. *Science* **347**, 519-522, doi:10.1126/science.aaa2725 (2015).

26 Protesescu, L. *et al.* Monodisperse Formamidinium Lead Bromide Nanocrystals with Bright and Stable Green Photoluminescence. *Journal of the American Chemical Society* **138**, 14202-14205, doi:10.1021/jacs.6b08900 (2016).

27 Rao, C. N. R. & Biswas, K. Characterization of Nanomaterials by Physical Methods. *Annual Review of Analytical Chemistry* **2**, 28 (2009).

28 Van der Heide, P. *X-ray photoelectron spectroscopy. [electronic resource] : an introduction to principles and practices*. (Hoboken, N.J. : Wiley, 2012., 2012).

29 Niemantsverdriet, J. W. in *Spectroscopy in Catalysis* 39-83 (Wiley-VCH Verlag GmbH & Co. KGaA, 2007).

30 Kirihata, H. & Uda, M. Externally quenched air counter for low‐energy electron emission measurements. *Review of Scientific Instruments* **52**, 68-70, doi:10.1063/1.1136448 (1981).

31 Zhao, H., Liu, G., Zhang, J., Arif, R. A. & Tansu, N. Analysis of Internal Quantum Efficiency and Current Injection Efficiency in III-Nitride Light-Emitting Diodes. *Journal of Display Technology* **9**, 212-225, doi:10.1109/JDT.2013.2250252 (2013).

# Chapter 4

## Precursor Non-stoichiometry to Enable Improved $CH_3NH_3PbBr_3$ Nanocrystal LED Performance

*In this chapter, a modified ligand-assisted re-precipitation (LARP) protocol was used for $CH_3NH_3PbBr_3$ nanocrystal (NC) synthesis. The ratio of precursors $CH_3NH_3Br$:$PbBr_2$ was varied to maximize radiative recombination in the NCs and thereby improve the performance. of $CH_3NH_3PbBr_3$-based light-emitting diodes (LEDs). The optical properties, crystallinity, particle size distribution and film formation of the NC inks were investigated in detail. The highest LED efficiency (1.75% external quantum efficiency) and brightness (>2700 cd $m^{-2}$) was achieved for the 1.15:1 precursor ratio. It is inferred that NC surface properties and film coverage are more crucial than photoluminescence intensity to achieve high device efficiency.*

## 4.1 Introduction

$CH_3NH_3PbBr_3$ nanoparticles for light-emitting diode (LED) applications have previously been synthesized by various methods, such as the emulsion synthesis technique for preparing the nanocrystals of different sizes,[1] HBr addition to obtain nanoplatelet architecture,[2] and fabrication of amorphous nanoparticles with high photoluminescence quantum yields.[3] In this project, a ligand-assisted re-precipitation (LARP) method, employed to synthesize $CH_3NH_3PbBr_3$ quantum dots for display applications,[4] was modified to fabricate spherical $CH_3NH_3PbBr_3$ nanocrystal (NC) inks exhibiting a NC size distribution of ca. 4-20 nm in diameter. Briefly, the precursors, $CH_3NH_3Br$ and $PbBr_2$, were dissolved in small quantities of polar *N,N*-dimethylformamide (DMF) and subsequently injected into non-polar toluene, which acts as anti-solvent to precipitate the NCs. No additional polar solvents were employed to further assist the NC precipitation. In addition, the long carbon chain ligands which passivate the NC surface and control their growth,[5-9] were pre-mixed in the toluene phase to ensure a uniform dispersion of ligands, while inhibiting the interactions of the precursors with the ligands prior to NC formation.

Further, the ratio of precursors, $CH_3NH_3Br$:$PbBr_2$ in the NC synthesis was varied to investigate possible passivation of NC surface using excess $CH_3NH_3Br$. A similar strategy was effective for direct crystallization of the halide perovskite phase from solution processing methods,[10] however, its implications for the colloidal LARP synthesis are not yet reported. The effect of precursor non-stoichiometry on the optical properties, crystallinity, particle size distribution, and film formation of the NC ink, was examined. LEDs fabricated from the NC inks synthesized from all the investigated precursor ratios showed promising device performances, with a ratio $CH_3NH_3Br$:$PbBr_2$ 1.15:1 displaying the highest brightness and efficiency. Moreover, the facile and scalable solution processing techniques involved in the NC ink synthesis and LED fabrication, makes this

research promising for large scale device manufacturing processes such as spray coating and inkjet printing.

## 4.2 Materials and Synthesis Protocol

**Materials.** Methylammonium bromide (Dyesol), lead bromide (TCI), *N*,*N*-dimethylformamide (DMF; Sigma Aldrich; anhydrous, 99.8%), toluene (Sigma Aldrich; anhydrous, 99.8%), *n*-octylamine (Aldrich; 99%), and oleic acid (Fluka; Ph. Eur) were used to prepare the perovskite NCs. All chemicals were used as received, without any further purification. Poly(3,4-ethylenedioxythiophene)-poly(styrenesulfonate) (PEDOT:PSS; Heraeus, Al 4083), 4,6-bis(3,5-di(pyridin-3-yl)phenyl)-2-methylpyrimidine (B3PYMPM; Lumtec), Ca, and Al, were used as hole-transporting layer (HTL), electron-transporting layer (ETL), and top electrodes, respectively. The electron transport and top electrode materials were stored and handled in Ar atmosphere. UV curing adhesive (Lumtec; epoxy resin/polymer) was used to encapsulate the LEDs.

**Synthesis and NC purification.** The $CH_3NH_3PbBr_3$ NCs were synthesized by a modification of the ligand-assisted reprecipitation (LARP) method.[4] First, stock solutions of $CH_3NH_3Br$ in DMF (0.1 mmol $mL^{-1}$) and $PbBr_2$ in DMF (0.1 mmol $mL^{-1}$), were prepared. The different precursor ratios, 1:1, 1.05:1, 1.15:1, and 1.25:1, were achieved by mixing the stock solutions in the corresponding ratios. The amount of $PbBr_2$ was fixed to 0.075 mmol for all the ratios and the volume of the precursor solution was maintained at 250 µL by adding required amounts of DMF (exact amounts presented in Table 4.1). Subsequently, this solution was swiftly injected into 5 mL toluene under vigorous stirring, in which an equimolar amount of *n*-octylamine (0.075 mmol; 12.4 µL) and 500 µL oleic acid were mixed prior to the precursors' injection. All reactions were carried out at room temperature under ambient conditions (60% relative humidity). The reaction was continued for 1 min, after which the obtained colloidal NC solution was

centrifuged for 5 min at 6000 rpm. The supernatant phase, containing unreacted precursors and excess ligands, was discarded. Subsequently, the precipitated NCs were re-dispersed in 1 mL toluene and centrifuged again for 5 min at 1000 rpm. The resulting supernatant phase was used as NC ink for subsequent studies and LED device fabrication.

**Table 4.1** Precursor amounts used in the non-stoichiometric synthesis of $CH_3NH_3PbBr_3$ NCs. MABr refers to $CH_3NH_3Br$.

| **MABr:$PbBr_2$ molar ratio** | **MABr (in millimoles)** | **MABr stock solution (in µL)** | **$PbBr_2$ (in millimoles)** | **$PbBr_2$ stock solution (in µL)** | **DMF (in µL)** | **Total solution (in µL)** |
|---|---|---|---|---|---|---|
| **1:1** | 0.075 | 75 | 0.075 | 75 | 100 | 250 |
| **1.05:1** | 0.07875 | 78.75 | 0.075 | 75 | 96.25 | 250 |
| **1.15:1** | 0.08625 | 86.25 | 0.075 | 75 | 88.75 | 250 |
| **1.25:1** | 0.09375 | 93.75 | 0.075 | 75 | 81.25 | 250 |

## 4.3 Result and Discussion

### 4.3.1 Optical and Structural Characterization – Stoichiometric Synthesis

$CH_3NH_3PbBr_3$ NC inks were first synthesized from a stoichiometric ratio of precursors, by a modified LARP method, as discussed in Section 4.2. The instantaneous change of the transparent toluene solution, into a greenish-yellow colloidal solution, upon precursor addition, indicated the formation of ligand-capped NCs.[4,11] No additional reagents, like butanol, γ-butyrolactone, or acetone,[3,11-13] were required to further assist the NC precipitation. The NC ink obtained after purification was bright and fluorescent green, indicating the formation of highly luminescent NCs (inset Figure 4.1-a). The absorption and photoluminescence (PL) spectra, revealed an absorption edge and PL maximum at ~531 nm and 522 nm, respectively (Figure 4.1-a), similar to reported values for $CH_3NH_3PbBr_3$ NCs.[14,15] The PL peak exhibits a full width half maximum (FWHM) of 21 nm, which indicates high color saturation favorable for display applications.[4]

The phase-purity of the NCs was determined from X-ray diffraction (XRD) measurements (Figure 4.1-b). The XRD patterns clearly shows the characteristic perovskite $CH_3NH_3PbBr_3$ peaks at 14.9°, 21.1°, 30.1°, 33.7°, 36.9°, 43.2°, and 46.1° which correspond to the (100), (110), (200), (210), (211), (220), and (300) planes, respectively.[10,13] This corresponds to the cubic phase with lattice constant 5.94 Å and Pm-3m space group.[13,16] The *n*-octylamine ligand used in the NC synthesis may also form a 2D layered octylammonium bromide structure, concurrently to the 3D $CH_3NH_3PbBr_3$ phase resulting in diffraction peaks below $2\theta = 10°$.[17] The absence of such additional peaks in the diffractograms indicate that phase-pure $CH_3NH_3PbBr_3$ NCs were fabricated from the stoichiometric precursor solutions.

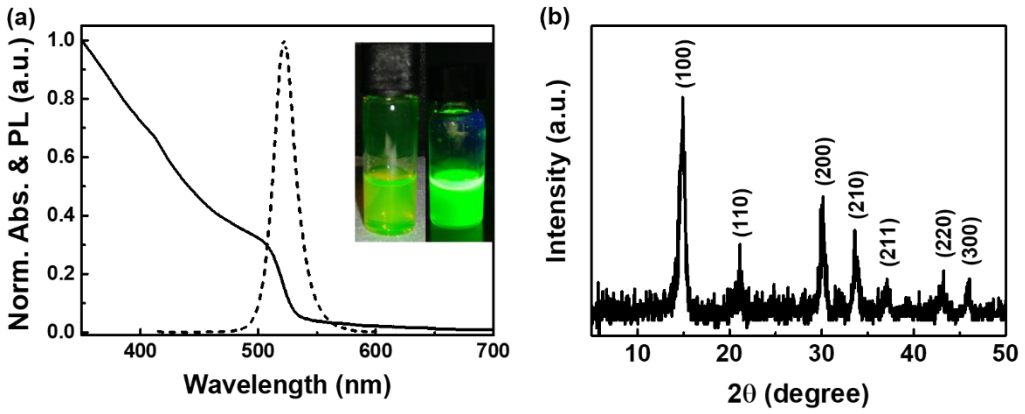


**Figure 4.1** Optical and structural characterization of $CH_3NH_3PbBr_3$ NCs synthesized from 1:1 ratio of $CH_3NH_3Br:PbBr_2$. (a) Absorbance of the NC ink (solid line) and steady-state PL of the spin-coated NC thin film (dashed line) The inset shows images of the NC ink under white light (left) and UV light (right), respectively. (b) XRD pattern of drop-casted NC film.

### 4.3.2 Non-Stoichiometric Synthesis and Subsequent Characterizations

The effect of excess $CH_3NH_3Br$ during the NCs synthesis was investigated using various ratios of $CH_3NH_3Br:PbBr_2$ in the precursor solution, specifically 1.05:1, 1.15:1, and 1.25:1, while keeping other reaction parameters and the

centrifugation procedure unchanged. (i.e. similar to reactions carried out with stoichiometric ratio). The NC inks exhibited similar bright green fluorescence for all tested stoichiometries, although it should be mentioned that for ratio 1.25:1 the NC ink appeared cloudy and less stable.

X-ray diffraction patterns of the samples were then analyzed to investigate if excess $CH_3NH_3Br$ affects the as-formed nanocrystals' phase and crystal structure. All tested precursor ratios displayed the characteristic cubic perovskite peaks, without the formation of secondary phases. The crystal phase and crystalline nature of the NCs was thus retained upon changing the precursor ratios (Figure 4.2).

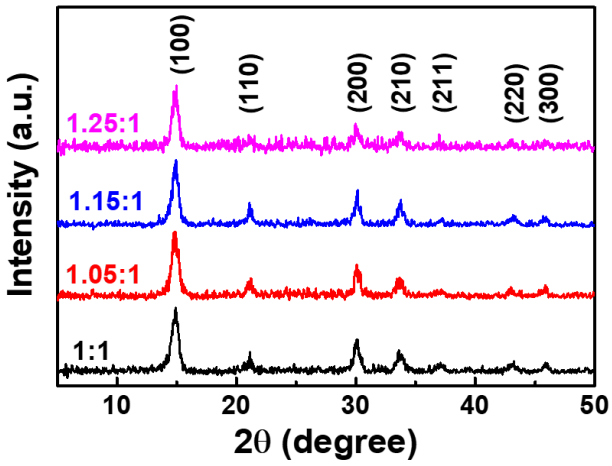


**Figure 4.2** XRD patterns of drop-casted films of $CH_3NH_3PbBr_3$ NC inks synthesized from the different $CH_3NH_3Br$:$PbBr_2$ ratios.

While no significant peak shifts were observed in the diffractograms, slight variations in the FWHM of the peaks were observed. The average crystallite size, as calculated from the Scherrer equation, were 11.3 nm, 11.6 nm, 13.6 nm and 12.3 nm, respectively for ratios 1:1, 1.05:1, 1.15:1 and 1.25:1. This suggests that excess $CH_3NH_3Br$ did not affect the crystal lattice, and only slightly influenced the NC sizes. This corroborates with the results obtained in case of using excess

$CH_3NH_3Br$ during direct formation of perovskite NC by spin coating the precursor solution to form thin films, as demonstrated by Cho et al.[10] Subsequent X-ray photoelectron spectroscopy (XPS) measurements showed a Br deficiency on the NC surface for all tested stoichiometries, with Pb:Br of ca. 2.6-2.7, similar to that reported by Gonzalez-Carrero et al.[13] (Table 4.2).

**Table 4.2** Elemental composition of the NCs synthesized from 1:1, 1.05:1, 1.15:1 and 1.25:1 ratios of $CH_3NH_3Br:PbBr_2$ extracted from X-ray photoelectron spectroscopy measurement.

| **$MABr:PbBr_2$** | **1:1** | **1.05:1** | **1.15:1** | **1.25:1** |
|---|---|---|---|---|
| Br/Pb | 2.64 | 2.67 | 2.56 | 2.69 |
| N/Pb | 1.26 | 1.33 | 1.09 | 1.23 |
| C/Pb | 1.03 | 1.04 | 1.30 | 1.60 |

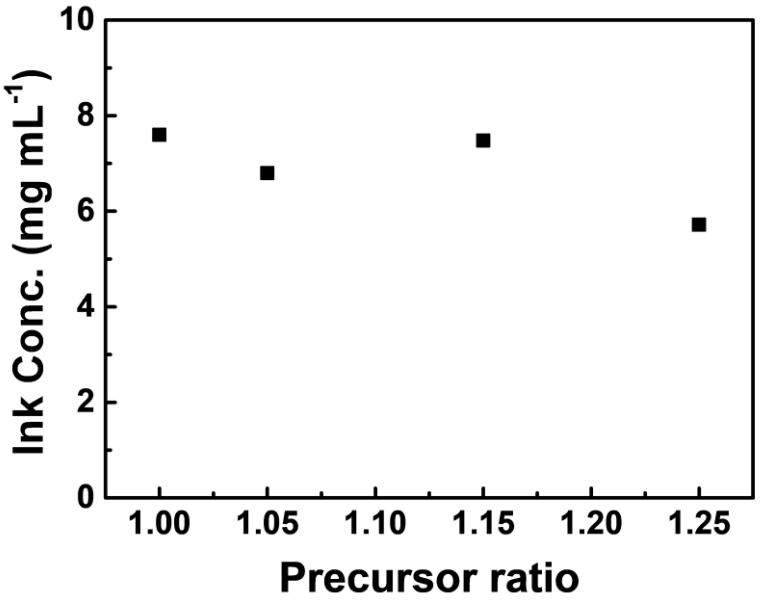


**Figure 4.3** NC ink concentration/ NC synthesis yield for the NCs prepared from the various $CH_3NH_3Br:PbBr_2$ ratios viz., 1:1, 1.05:1, 1.15:1, and 1.25:1.

The NCs synthesized using non-stoichiometric precursor ratios showed different ink concentrations (i.e. NC yield, Figure 4.3) compared to stoichiometric synthesis. This is clearly observed in the absorbance spectra of the NC inks (Figure 4.4-a). Although all samples displayed a similar absorption edge ranging 531-534 nm (ca. 2.3 eV optical band gap), the absorbance was significantly lower for the 1.25:1 ratio. This may be related to the lower colloidal phase stability (i.e. cloudy NC ink with precipitate), and consequently lower NC yield after purification.

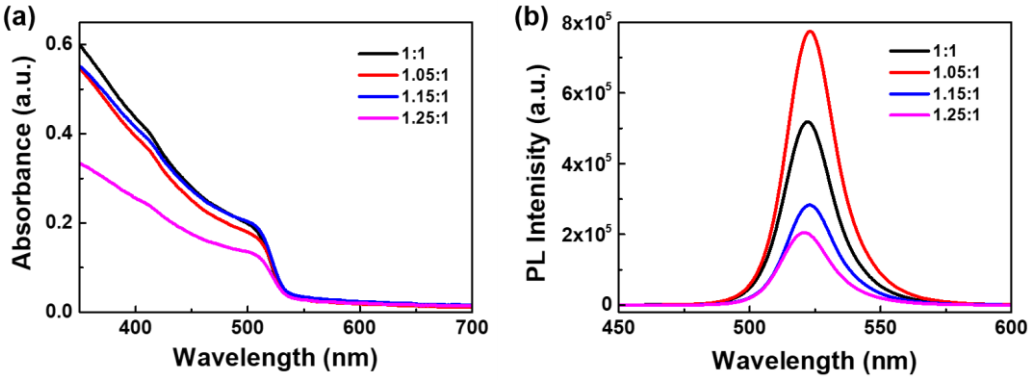


**Figure 4.4** Comparison of (a) absorbance, (b) steady-state PL spectra of NCs prepared by varying the $CH_3NH_3Br:PbBr_2$ ratios viz., 1:1 (black), 1.05:1 (red), 1.15:1 (blue), and 1.25:1 (magenta). The normalized PL intensity is corrected for the differences in absorbance according to $PL_{corr}=PL/[1-(10^{-Abs})]$. Here, the excitation wavelength used for PL measurements was 400 nm.

Next, the PL of the NCs inks was studied as an important indicator for the electroluminescence (EL) in light-emitting devices. A comparison of the spin-coated thin films prepared from all tested $CH_3NH_3Br:PbBr_2$ ratios, displayed a similar maximum PL emission and FWHM of approximately 522.7 ± 0.1 nm and 22.2 ± 0.1 nm, respectively (Table 4.3; peak fits shown in Figure 4.5). The PL intensity was corrected for the differences in absorbance at the excitation wavelength using $PL_{corr}=PL/[1-(10^{-Abs})]$, to fairly compare the PL from the various samples (Figure 4.4-b). A slight excess of $CH_3NH_3Br:PbBr_2$ = 1.05:1 displayed the highest PL, while increased $CH_3NH_3Br$ amounts led to decline in

the PL intensity. Since the PL is already corrected for the absorbance, the higher PL intensity thus indicates improved radiative recombination. The decrease in PL at higher $CH_3NH_3Br:PbBr_2$ ratios may be due to replacement of capping ligands by the excess $CH_3NH_3^+$ ions,[18] which may adversely affect charge confinement and thereby reduce radiative recombination. Moreover, excessive amounts of $CH_3NH_3Br$ can de-stabilize the colloidal solution, as observed in case of 1.25:1 ratio.

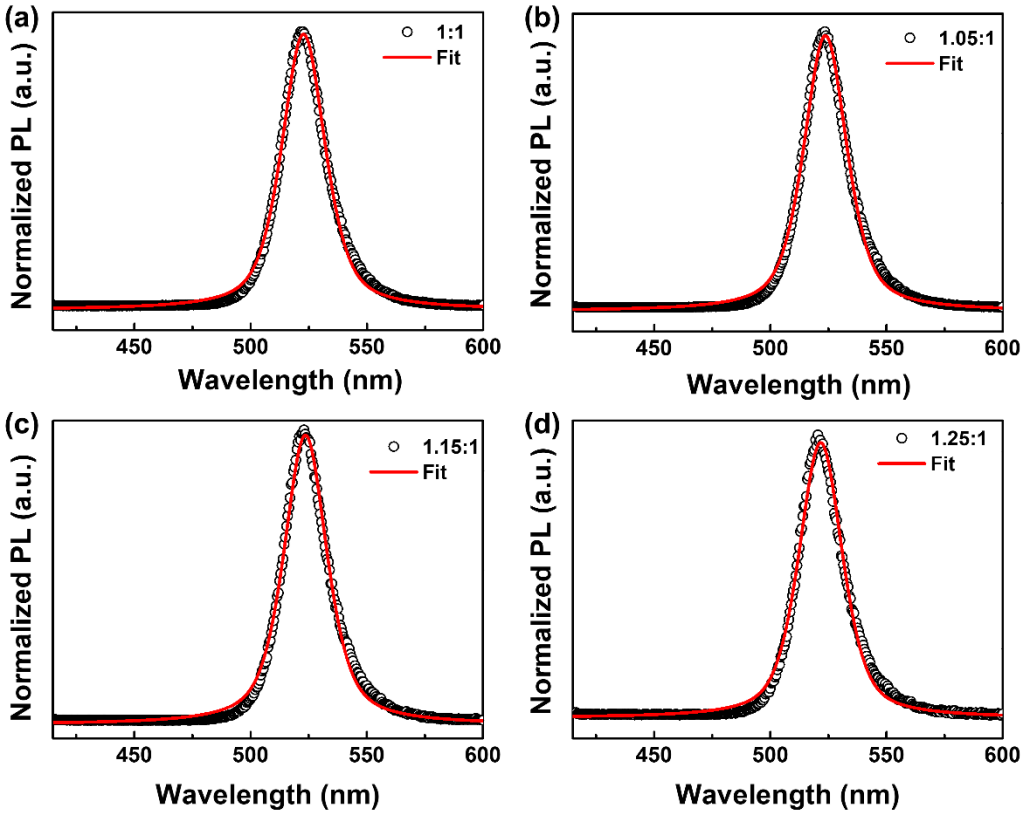


**Figure 4.5** Steady state photoluminescence (PL) spectra (black circles) and fits for maximum PL (red line) for NCs prepared from the various $CH_3NH_3Br:PbBr_2$ ratios. (a) 1:1, (b) 1.05:1, (c).1.15:1, and (d) 1.25:1.

**Table 4.3** Steady state PL peak positions and full width half maximum (FWHM) obtained from the non-linear pseudo-Voigt curve fits.

| Ratios | PL peak wavelength (nm) | FWHM (nm) |
|---|---|---|
| **1:1** | 522.7 | 22.2 |
| **1.05:1** | 523.7 | 22.1 |
| **1.15:1** | 523.6 | 22.1 |
| **1.25:1** | 521.7 | 22.3 |

Next, the size distribution of the NC inks (in solution phase) was investigated by means of small angle X-ray scattering (SAXS). Interestingly, a bimodal size distribution was observed with peaks centered roughly at 6 nm and 18 nm mean diameter for all investigated samples (Figure 4.6-a). To confirm whether the size distribution is retained after solvent evaporation (i.e. in thin film), the particle size distribution was also determined from the low-magnification TEM images of the 1.15:1 sample (Figure 4.6-b, c). The size distribution obtained from the TEM image corresponds well with the values extracted from the scattering curves. Moreover, the average nanocrystal sizes obtained from the TEM image matches well with the average sizes obtained from XRD. It is noticed that the average NC sizes in the solution phase are slightly larger than that in films. This could be due to the dynamic nature of the ligand attachment and separation in the solution,[6] which may affect the sizes measured with SAXS.

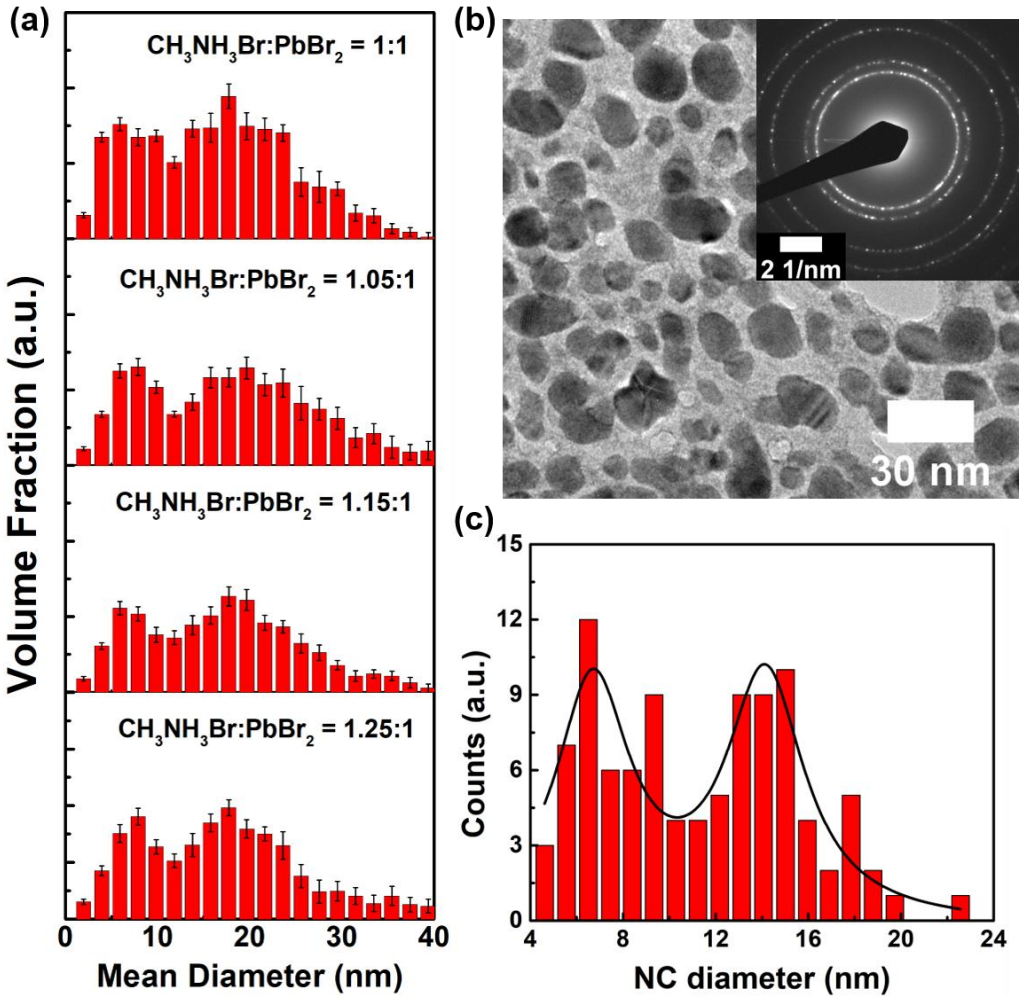


**Figure 4.6** (a) Particle size distribution of the NC ink, extracted from the small angle X-ray scattering measurements, for the $CH_3NH_3PbBr_3$ NCs synthesized from $CH_3NH_3Br$:$PbBr_2$ ratios of 1:1, 1.05:1, 1.15:1, and 1.25:1. (b) TEM image of NC ink prepared from 1.15:1 precursor, drop casted on Cu grid. The inset is the SAED images clearly showing the polycrystalline nature of the NCs. (c) Particle size distribution extracted from the above TEM image, at least 100 NCs were measured.

To investigate the effect of precursor non-stoichiometry on the NC surface passivation, time-resolved photoluminescence (TRPL) measurements were performed. The PL decay kinetics, after photoexcitation from a pulsed laser, reveal the nature of the radiative recombination. The recombination lifetimes were obtained from bi-exponential fitting the TRPL decay curves. The fit

function is: $I(t) = A_f e^{\frac{-t}{\tau_f}} + A_s e^{\frac{-t}{\tau_s}}$, where $\tau_f$ and $\tau_s$ are the fast and slow decay lifetimes, respectively, and $A_f$ and $A_s$ are their respective decay amplitudes. The average lifetime is calculated as $\tau_{avg} = A_f\tau_f + A_s\tau_s$. Generally, fast decay represents the trap-assisted recombinations at the crystal surface and the longer-lifetime component represents radiative recombinations inside the crystals.[19] Herein, average decay times of 5.52 ns, 5.49 ns, 6.30 ns and 8.36 ns were estimated for the 1:1, 1.05:1, 1.15:1 and 1.25:1 ratios of $CH_3NH_3Br$:$PbBr_2$, respectively (Figure 4.7, Table 4.2; peak fits shown in Figure 4.8).

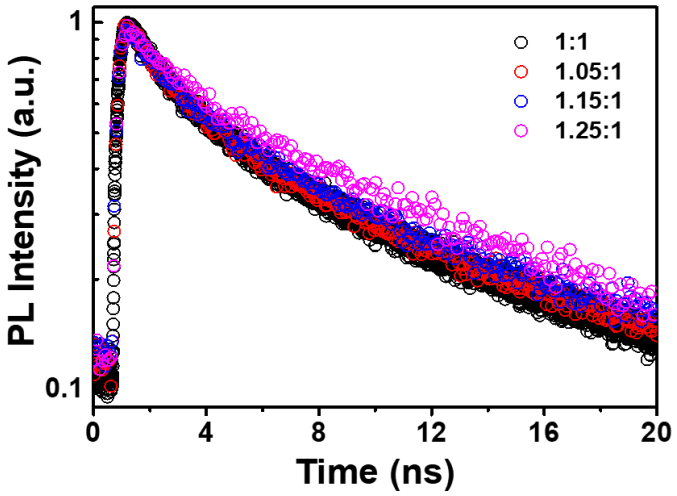


**Figure 4.7** TRPL spectra of NCs prepared by varying the $CH_3NH_3Br$:$PbBr_2$ ratios viz. 1:1 (black), 1.05:1 (red), 1.15:1 (blue), and 1.25:1 (magenta).

**Table 4.4** Recombination lifetimes obtained from bi-exponential fitting of the TRPL decay curves.

| Ratios | $\tau_f$ (ns) | $A_f$ (%) | $\tau_s$ (ns) | $A_s$ (%) | $\tau_{avg}$ (ns) |
|---|---|---|---|---|---|
| **1:1** | 1.60 | 43 | 8.43 | 57 | 5.52 |
| **1.05:1** | 1.53 | 42 | 8.40 | 58 | 5.49 |
| **1.15:1** | 1.52 | 32 | 8.55 | 68 | 6.30 |
| **1.25:1** | 1.97 | 35 | 11.84 | 65 | 8.36 |

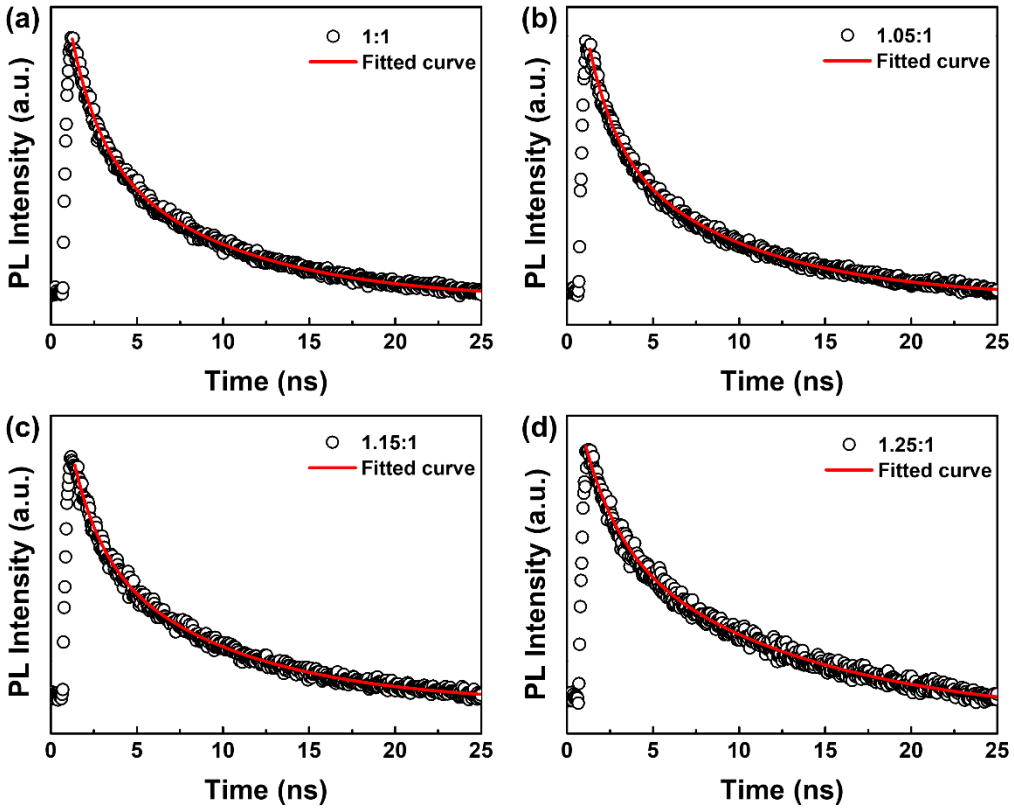


**Figure 4.8** Time-resolved photoluminescence (TRPL) decays (black circles) and fits (red line) for NCs prepared from the various $CH_3NH_3Br$:$PbBr_2$ ratios. (a) 1:1, (b) 1.05:1, (c).1.15:1, and (d) 1.25:1.

The short average lifetimes (< 10 ns), are indicative of the large number of grain boundaries, which may act as traps in the NC film. However, the relative contribution of the trap-assisted recombination component, $A_f$, decreased from ca. 42 % for both 1:1 and 1.05:1 ratios, to approximately 32 % for 1.15:1. The decrease in $A_f$ value may indicate a slight reduction in number of trap states due to improved surface defect passivation by the excess $CH_3NH_3Br$. Moreover, if we calculate the volume of the NCs from the average crystallite size determined from the Scherrer equation, there is a ~75% crystallite volume increase for the 1.15:1 $CH_3NH_3Br$:$PbBr_2$ compared to the 1:1 ratio, despite the minor increase in crystallite size (13.6 nm compared to 11.3 nm, respectively). This increase in NC volume implies a 20% decrease in surface-to-volume ratio for the former, which

could significantly lower the contribution of surface traps to the recombination in the NC films. It is noted that the amplitude of the trap-assisted decay component is similar to the 1.15:1 ratio for the 1.25:1 $CH_3NH_3Br:PbBr_2$ ratio, however, the low colloidal stability of the latter makes it less promising for LED applications.

### 4.3.3 LED Fabrication and Characterization

Light-emitting diodes (LEDs) were fabricated using the $CH_3NH_3PbBr_3$ NCs prepared from the different precursor ratios of $CH_3NH_3Br:PbBr_2$. A device structure with ITO / PEDOT:PSS / $CH_3NH_3PbBr_3$ NC / B3PYMPM (45 nm) / Ca (7nm) / Al (80 nm) was used. Here, the PEDOT:PSS and the $CH_3NH_3PbBr_3$ NC layers were spin coated, while the subsequent charge transport layers were thermally evaporated. Cross-sectional imaging of the ITO/PEDOT:PSS/ $CH_3NH_3PbBr_3$ NC stack, under a scanning electron microscope (SEM), showed ~30 nm of PEDOT:PSS layer and ~40 nm NC layer (Figure 4.9-a) The top view SEM imaging revealed that the nanoparticle morphology was retained in the thin film (Figure 4.9-b).

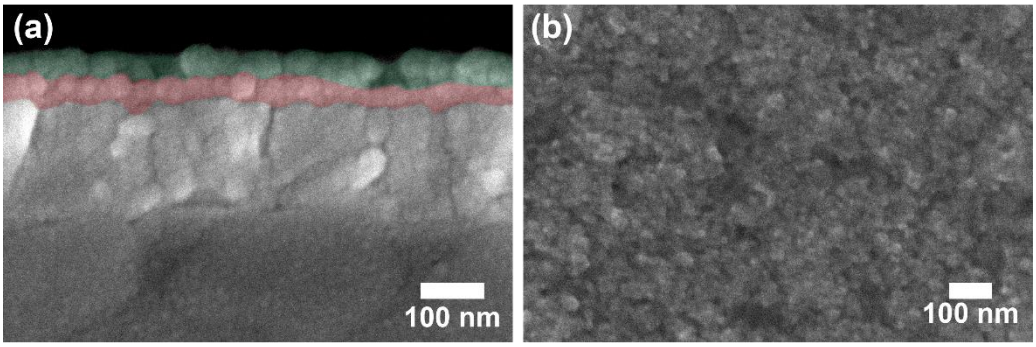


**Figure 4.9** Scanning electron microscopy (SEM) images of (a) cross section and (b) top morphology of NC ink prepared from 1.15:1 ratio of $CH_3NH_3Br:PbBr_2$, spin coated on top of ITO/PEDOT:PSS. The green and red layers in (a) represent the perovskite emitter and PEDOT:PSS layer, respectively.

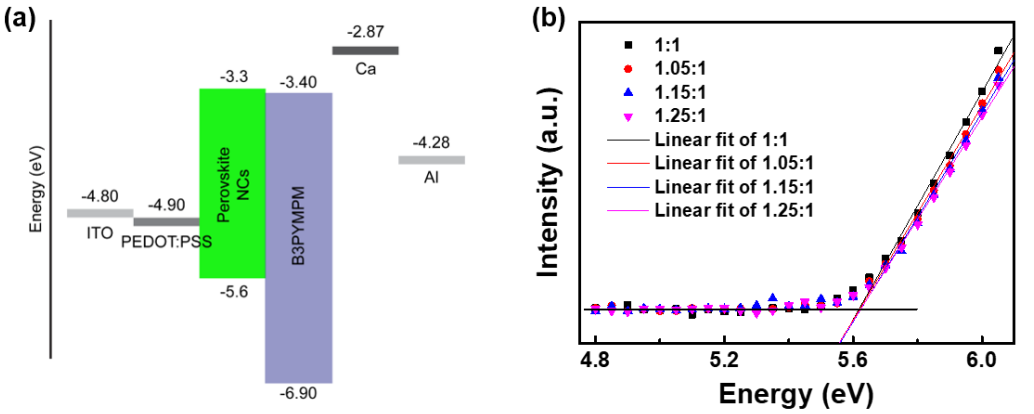


**Figure 4.10** (a) Schematic diagram of the flat band energy levels of the LED device stack. (b) Valence band maxima (VBM) of the various NC inks prepared from the $CH_3NH_3Br$:$PbBr_2$ ratios of 1:1 (black), 1.05:1 (red), 1.15:1 (blue), and 1.25:1 (magenta), calculated from the photoelectron spectroscopy in air (PESA) measurements.

The flat-band energy level diagram for the complete LED device stack is depicted in Figure 4.10-a. Valence band maxima (VBM) for the NCs, ca. 5.6 eV for all samples (Figure 4.10-b), calculated from photoelectron spectroscopy in air (PESA), correspond well with previous reports for $CH_3NH_3PbBr_3$.[20] The PEDOT:PSS and B3PYMPM layers acted as good hole and electron transport layers, with a work function (WF) of 4.9 eV,[21] and lowest unoccupied molecular orbital (LUMO) level of ca. 3.4 eV,[22] respectively. The WF has an offset of ~0.7 eV with the NC VBM, whereas the LUMO level has a 0.1 eV offset with the NC conduction band minimum (CBM). Here, the CBM value was calculated through the addition of the optical band gap of 2.3 eV to the VBM value.

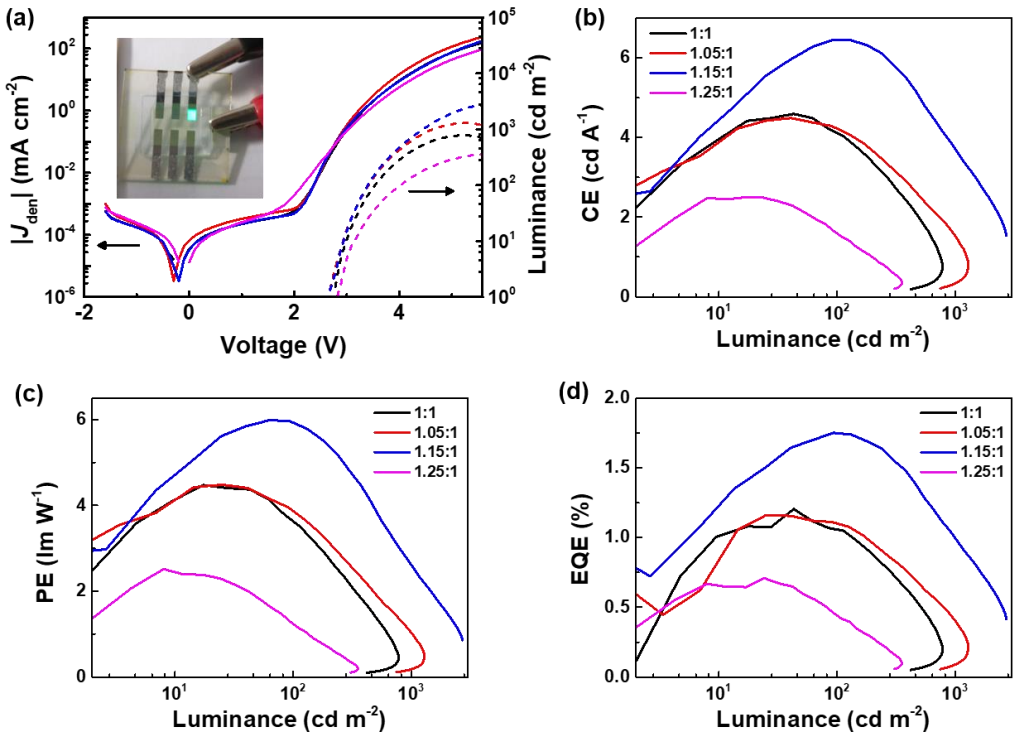


**Figure 4.11** LED characterization (a) Current density-voltage-luminance (J-V-L) curves of the devices – the solid lines represent the J-V curves while the dashed lines represent the L-V curves. The inset shows a representative image of my LED device. (b-d) Current efficiency (CE), power efficiency (PE) and external quantum efficiency (EQE) plot, respectively, of the devices as a function of luminance. The black, red, blue and magenta curves correspond to the 1:1, 1.05:1, 1.15:1, and 1.25:1 ratios of $CH_3NH_3Br$:$PbBr_2$ respectively.

The device performances are shown in Figure 4.11. All the devices displayed a turn-on voltage (defined as voltage required to reach 1 cd $m^{-2}$) of 2.7-2.8 V. The turn-on voltage is higher than the optical band gap of 2.3 eV, but lower than previously reported for $CH_3NH_3PbBr_3$ nanoparticle LEDs.[1-3] The turn-on voltage is dependent on the transport layers used,[11] and may be further lowered by employing transport layers which provide better charge injection and charge confinement (Figure A1 - See Appendix). The J-V-L curves also reveal low leakage currents (~$10^{-4}$ mA $cm^{-2}$), in all the devices. The low turn-on voltages and leakage currents are indicative of good injection of carriers (no significant

injection barrier due to the ligands) as well as good surface coverage of the NCs (no shunt paths).

As shown in Figure 4.11, the 1.15:1 ratio of $CH_3NH_3Br:PbBr_2$ displayed the highest luminance among all fabricated devices, with a maximum luminance of 2721 cd $m^{-2}$ at 5.6 V. The same device also exhibited the best current efficiency of 6.45 cd $A^{-1}$, obtained at 3.4 V and 93.8 cd $m^{-2}$ luminance. The maximum EQE obtained was 1.75% which is, to the best of my knowledge, the second highest recorded efficiency for perovskite NC-based LEDs. The performance of the best device compared to other $CH_3NH_3PbBr_3$ NC reported in literature is summarized in Table A1 - See Appendix. It is interesting that despite a lower PL intensity compared to the 1.05:1 and 1:1 ratios, the EL intensity and device efficiency was higher for the 1.15:1 ratio. This could be related to the lower trap-assisted recombination in the 1.15:1 ratio samples, as determined with TRPL. In addition, the morphology of the NC film can critically influence the device performance.[10,23]

To examine the surface morphology of the NC films, atomic force microscopy (AFM) was used. A 3D view of the AFM images clearly depicts non-uniform NC coverage for all investigated samples (Figure 4.12). I postulate that the large gaps (violet to pink color) observed in the images are in fact a layer of NCs. In case of pin hole formation, high leakage currents and shunt paths are expected.[7,24] The absence of any additional resistances in the J-V curve (Figure 4.11-a) and good diode behavior, thus suggests that the nanocrystals form a sufficiently dense film. Nevertheless, the $CH_3NH_3Br:PbBr_2$ 1.05:1 and 1.25:1 ratios showed poor thin film uniformity, as illustrated by large areas of low NC film height (violet to pink color) in the respective NC thin films. The surface morphology appears, relatively less non-uniform for the 1:1 and 1.15:1 ratios. To more accurately compare the surface morphologies of the 1:1 and 1.15:1 ratios, were examined using height profiles extracted from the 2D AFM top-view images. (Figure 4.13).

Clearly, the height variation for the 1.15:1 ratio is less than that observed for the 1:1 ratio, which could lead to more concentrated recombination, and consequently, to higher electroluminescence in the $CH_3NH_3Br:PbBr_2$ 1.15:1 sample.

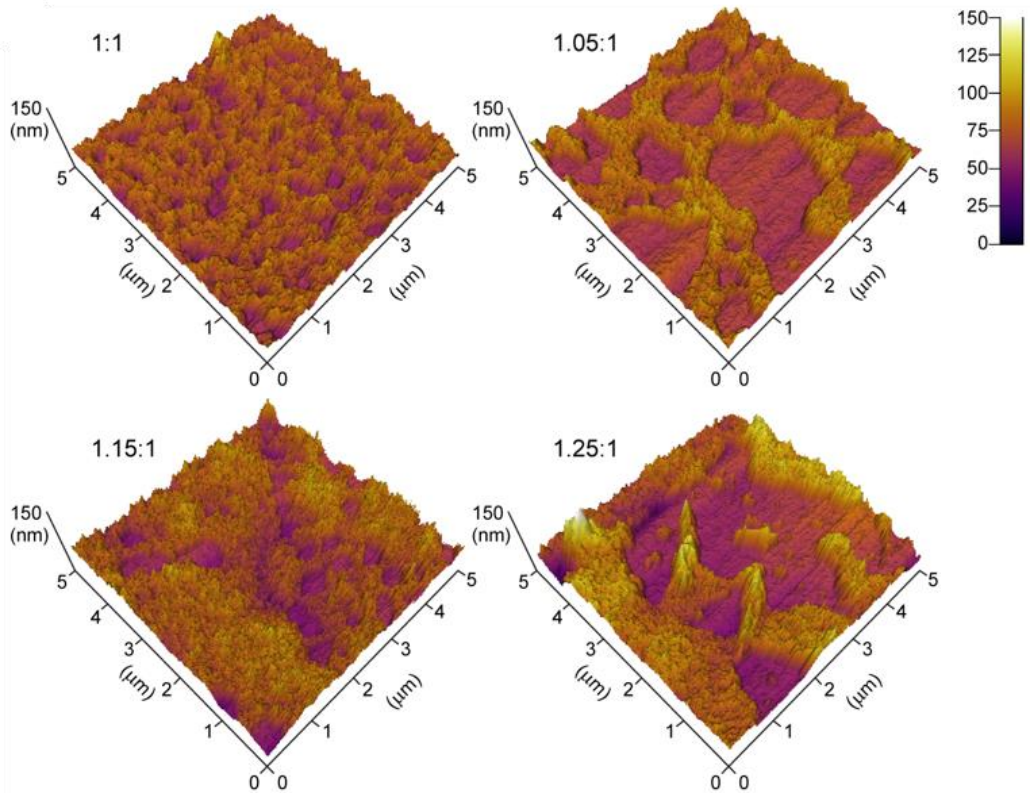


**Figure 4.12** 3D view of AFM images of thin films of NCs prepared by varying the $CH_3NH_3Br:PbBr_2$ ratios viz., 1:1, 1.05:1, 1.15:1, and 1.25:1.

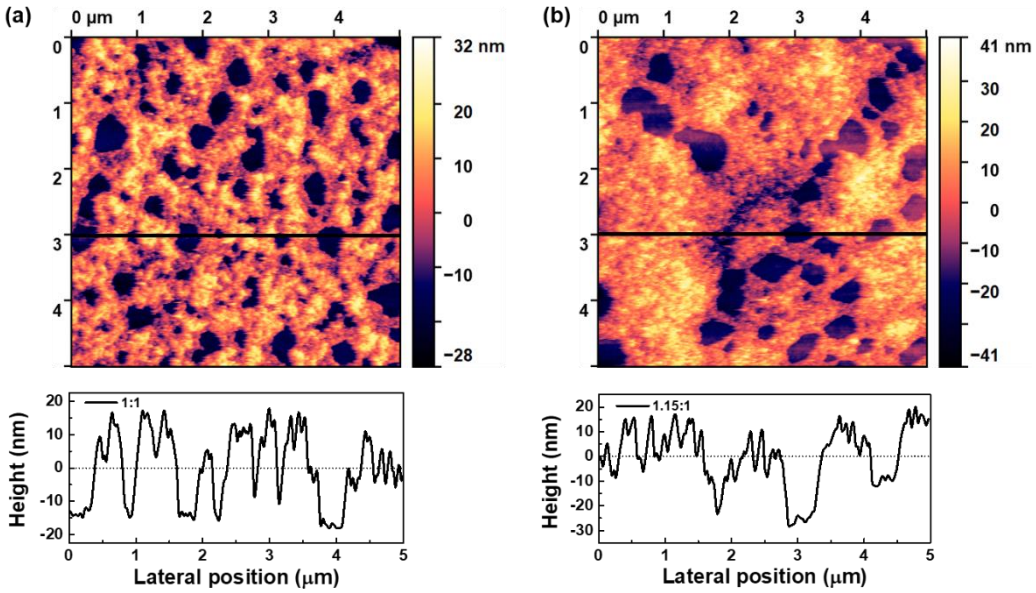


**Figure 4.13** Comparison of 2D AFM images and height profiles of $CH_3NH_3PbBr_3$ NC thin films prepared from (a) 1:1 and (b) 1.15:1 ratio of $CH_3NH_3Br$:$PbBr_2$. The horizontal black lines in the images indicate the position of height profile measurement.

## 4.4 Conclusion

Highly luminescent $CH_3NH_3PbBr_3$ NC inks, with a bimodal particle size distribution, were synthesized through a modified LARP synthesis protocol. The $CH_3NH_3Br$:$PbBr_2$ ratio in the precursor solution was varied to 1.05:1, 1.15:1, and 1.25:1. The influence of the precursor non-stoichiometry on the optical and structural properties of the NCs, as well as the implications for NC film formation and subsequent LED performances were evaluated. The cubic perovskite crystal structure and the NC sizes were virtually unaffected by the addition of excess $CH_3NH_3Br$; however, the optical properties and the NC film surface morphologies, were significantly influenced. Interestingly, while the PL intensity was highest for the NCs formed from 1.05:1 ratio of $CH_3NH_3Br$:$PbBr_2$, EL intensity was highest for the 1.15:1 ratio. The higher electroluminescence for the 1.15:1 precursor ratio could be attributed to higher NC density in the spin-coated films as well as the reduction in trap-assisted recombination, compared to the other investigated precursor ratios. The NC surface properties and film coverage

were found to be more critical than high PL in the NCs for achieving high EL in devices. Notably, the LEDs prepared from the $CH_3NH_3PbBr_3$ NC inks, synthesized from a 1.15:1 precursor ratio, achieved a maximum EQE of 1.75%, which is among the best reported efficiencies for $CH_3NH_3PbBr_3$ NC-based LEDs.

## 4.5 References


1 Huang, H. *et al.* Emulsion Synthesis of Size-Tunable $CH_3NH_3PbBr_3$ Quantum Dots: An Alternative Route toward Efficient Light-Emitting Diodes. *ACS Applied Materials & Interfaces* **7**, 28128-28133, doi:10.1021/acsami.5b10373 (2015).

2 Ling, Y. *et al.* Bright Light-Emitting Diodes Based on Organometal Halide Perovskite Nanoplatelets. *Advanced Materials* **28**, 305-311, doi:10.1002/adma.201503954 (2016).

3 Xing, J. *et al.* High-Efficiency Light-Emitting Diodes of Organometal Halide Perovskite Amorphous Nanoparticles. *ACS Nano* **10**, 6623-6630, doi:10.1021/acsnano.6b01540 (2016).

4 Zhang, F. *et al.* Brightly Luminescent and Color-Tunable Colloidal $CH_3NH_3PbX_3$ (X = Br, I, Cl) Quantum Dots: Potential Alternatives for Display Technology. *ACS Nano* **9**, 4533-4542, doi:10.1021/acsnano.5b01154 (2015).

5 De Roo, J., De Keukeleere, K., Hens, Z. & Van Driessche, I. From ligands to binding motifs and beyond; the enhanced versatility of nanocrystal surfaces. *Dalton Transactions* **45**, 13277-13283, doi:10.1039/C6DT02410F (2016).

6 De Roo, J. *et al.* Highly Dynamic Ligand Binding and Light Absorption Coefficient of Cesium Lead Bromide Perovskite Nanocrystals. *ACS Nano* **10**, 2071-2081, doi:10.1021/acsnano.5b06295 (2016).

7 Li, J. *et al.* 50-Fold EQE Improvement up to 6.27% of Solution-Processed All-Inorganic Perovskite $CsPbBr_3$ QLEDs via Surface Ligand Density

Control. *Advanced Materials* **29**, 1603885(1603881-1603889), doi:10.1002/adma.201603885 (2017).

8 Pan, A. *et al.* Insight into the Ligand-Mediated Synthesis of Colloidal $CsPbBr_3$ Perovskite Nanocrystals: The Role of Organic Acid, Base, and Cesium Precursors. *ACS Nano* **10**, 7943-7954, doi:10.1021/acsnano.6b03863 (2016).

9 Gonzalez-Carrero, S. *et al.* The Luminescence of $CH_3NH_3PbBr_3$ Perovskite Nanoparticles Crests the Summit and Their Photostability under Wet Conditions is Enhanced. *Small* **12**, 5245-5250, doi:10.1002/smll.201600209 (2016).

10 Cho, H. *et al.* Overcoming the electroluminescence efficiency limitations of perovskite light-emitting diodes. *Science* **350**, 1222-1225, doi:10.1126/science.aad1818 (2015).

11 Perumal, A. *et al.* High brightness formamidinium lead bromide perovskite nanocrystal light emitting devices. *Scientific Reports* **6**, 36733, doi:10.1038/srep36733 (2016).

12 Schmidt, L. C. *et al.* Nontemplate synthesis of $CH_3NH_3PbBr_3$ perovskite nanoparticles. *J Am Chem Soc* **136**, 850-853, doi:10.1021/ja4109209 (2014).

13 Gonzalez-Carrero, S., Galian, R. E. & Perez-Prieto, J. Maximizing the emissive properties of $CH_3NH_3PbBr_3$ perovskite nanoparticles. *Journal of Materials Chemistry A* **3**, 9187-9193, doi:10.1039/c4ta05878j (2015).

14 Zhu, F. *et al.* Shape Evolution and Single Particle Luminescence of Organometal Halide Perovskite Nanocrystals. *ACS Nano* **9**, 2948-2959, doi:10.1021/nn507020s (2015).

15 Edri, E., Kirmayer, S., Cahen, D. & Hodes, G. High Open-Circuit Voltage Solar Cells Based on Organic–Inorganic Lead Bromide Perovskite. *The Journal of Physical Chemistry Letters* **4**, 897-902, doi:10.1021/jz400348q (2013).

16 Poglitsch, A. & Weber, D. Dynamic disorder in methylammoniumtrihalogenoplumbates (II) observed by millimeter‐wave spectroscopy. *The Journal of Chemical Physics* **87**, 6373-6378, doi:10.1063/1.453467 (1987).

17 Bhaumik, S. *et al.* Highly stable, luminescent core-shell type methylammonium-octylammonium lead bromide layered perovskite nanoparticles. *Chemical Communications*, doi:10.1039/C6CC01056C (2016).

18 Wang, L. *et al.* Scalable Ligand-Mediated Transport Synthesis of Organic-Inorganic Hybrid Perovskite Nanocrystals with Resolved Electronic Structure and Ultrafast Dynamics. *ACS Nano* **11**, 2689-2696, doi:10.1021/acsnano.6b07574 (2017).

19 Shi, D. *et al.* Low trap-state density and long carrier diffusion in organolead trihalide perovskite single crystals. *Science* **347**, 519-522, doi:10.1126/science.aaa2725 (2015).

20 Ryu, S. *et al.* Voltage output of efficient perovskite solar cells with high open-circuit voltage and fill factor. *Energy & Environmental Science* **7**, 2614-2618, doi:10.1039/C4EE00762J (2014).

21 Ratcliff, E. L. *et al.* Formation of interfacial traps upon surface protonation in small molecule solution processed bulk heterojunctions probed by photoelectron spectroscopy. *Journal of Materials Chemistry C* **1**, 6223-6234, doi:10.1039/C3TC31064G (2013).

22 Sasabe, H. *et al.* Influence of Substituted Pyridine Rings on Physical Properties and Electron Mobilities of 2-Methylpyrimidine Skeleton-Based Electron Transporters. *Advanced Functional Materials* **21**, 336-342, doi:10.1002/adfm.201001252 (2011).

23 Wen, X. *et al.* Morphology and Carrier Extraction Study of Organic–Inorganic Metal Halide Perovskite by One- and Two-Photon Fluorescence Microscopy. *The Journal of Physical Chemistry Letters* **5**, 3849-3853, doi:10.1021/jz502014r (2014).

24 Li, J., Bade, S. G. R., Shan, X. & Yu, Z. Single-Layer Light-Emitting Diodes Using Organometal Halide Perovskite/Poly(ethylene oxide) Composite Thin Films. *Advanced Materials* **27**, 5196-5202, doi:10.1002/adma.201502490 (2015).

# Chapter 5

# Effect of Nanocrystal Size Distribution on $CH_3NH_3PbBr_3$-based LED Performance

*This chapter summarizes the efforts to improve the LED device efficiency and stability through manipulation of the size distribution of the nanocrystals (NCs) in the $CH_3NH_3PbBr_3$ ink. Three different size distributions – single mode, narrow bimodal and split bimodal – were investigated. The effect of variation of the NC size distribution on structural, topographical and optical properties of the NC film was examined. The split bimodal size distribution resulted in efficient radiative recombination and low surface roughness upon film formation. Finally, LEDs were fabricated with NC inks of all three size distributions, and improved LED device efficiency and stability were obtained for the split bimodal distribution.*

## 5.1 Introduction

The $CH_3NH_3PbBr_3$ nanocrystal (NC) inks synthesized in this work using a modified ligand assisted re-precipitation (LARP) approach, displayed a bimodal NC size distribution, centered at roughly 6 and 18 nm (see Chapter 4). In contrast, previous reports of colloidal $CH_3NH_3PbBr_3$ NC-based LEDs have employed inks with single mode NC size distribution centered at approximately 6.1 nm,[1] 4.6 ± 1.1 nm,[2] and 3.3 ± 0.7 nm.[3] This forms an interesting point for further investigations because the size distribution of perovskite NCs in the ink can strongly influence their radiative recombination behavior.

Firstly, if the NC size is smaller than the Bohr diameter, quantum confinement effects separate the energy levels to discrete states and widen the band gap, thereby blue-shifting the photoluminescence wavelength.[4-6] Secondly, crystal surfaces (grain boundaries) act as defect sites and may form shallow traps which compete with radiative recombination,[7,8] this becomes more prominent at smaller NC sizes. Third, strong spatial confinement of excitons in NCs can inhibit dissociation of electrons and holes and thereby increase radiative recombination.[9] Fourth, the surface coverage and roughness of the perovskite thin film layer is dependent on the shape and size, as well as the size distribution of the nanocrystals; thus, a uniform and pin-hole free film is ideal for device applications.[10-12] Finally, a distribution of NCs of different sizes can result in funneling of electrons from NCs of smaller size (i.e. larger bandgap) to larger size (i.e. smaller bandgap),[13] which would localize the recombination, increasing the luminescence quantum yield at low excitation power.[14] However, funneling of electrons can also lead to long-term electrical stress, which may degrade the device.[15]

To investigate the effect of NC size distribution on the electroluminescence (EL) achieved from $CH_3NH_3PbBr_3$ NC-based LEDs, adaptations of the LARP

technique (see Chapter 4), were employed to obtain different types of NC size distributions. A single mode size distribution was prepared by lowering the amount of anti-solvent (toluene) used in the NC precipitation step. A split bimodal size distribution was achieved by adding a polar solvent (1-butanol) along with lowering of the toluene amount. The concentration of the NC inks for these two types of size distributions were adjusted to be similar to that of the narrow bimodal size distribution, by controlling the amount of solvent (toluene) in the NC purification step (conc.=7.5 ± 0.5 mg $mL^{-1}$). Thereafter, the phase purity of synthesized $CH_3NH_3PbBr_3$ NC inks was verified, and the influence of the size distribution on NC thin film formation, optical properties and device LED performance were examined.

## 5.2 Materials and Synthesis Protocols

### 5.2.1 Materials

Methylammonium bromide (Dyesol), lead bromide (TCI), *N*,*N*-dimethylformamide (DMF; Sigma Aldrich; anhydrous, 99.8%), toluene (Sigma Aldrich; anhydrous, 99.8%), 1-butanol (Sigma Aldrich; anhydrous, 99.8%), *n*-octylamine (Aldrich; 99%), and oleic acid (Fluka; Ph. Eur) were used to prepare the perovskite NCs. All chemicals were used as received, without any further purification. Poly(3,4-ethylenedioxythiophene)-poly(styrenesulfonate) (PEDOT:PSS; Heraeus, Al 4083), 2,4,6-Tris[3-(diphenylphosphinyl)phenyl]-1,3,5-triazine (PO-T2T; Lumtec), Ca, and Al, were used as hole-transporting layer (HTL), electron-transporting layer (ETL), and top electrodes, respectively. The electron transport and top electrode materials were stored and handled in Ar atmosphere. UV curing adhesive (Lumtec; epoxy resin/polymer) was used to encapsulate the LEDs.

### 5.2.2 Synthesis of NCs with Different Size Distribution

**Narrow Bimodal Size Distribution.** The standard procedure described in Chapter 4 was followed. Briefly, 250 µL precursor solution was prepared from 1 mol $L^{-1}$ stock solutions of $CH_3NH_3Br$ and $PbBr_2$ in DMF, in 1.15:1 molar ratio (9.6 mg or 0.0863 mmol $CH_3NH_3Br$ and 27.5 mg or 0.075 mmol $PbBr_2$). Separately, *n*-octylamine (12.4 µL; 0.075 mmol) and oleic acid (500 µL; 1.58 mmol) were pre-mixed in 5 mL toluene. Subsequently, the precursor solution was swiftly injected into the toluene-ligand mixed solution under vigorous stirring. The reaction was continued for 1 min, after which the obtained colloidal NC solution was centrifuged for 5 min at 6000 rpm. The supernatant phase, containing unreacted precursors and excess ligands, was discarded. Next, the precipitated NCs were re-dispersed in 1 mL toluene and centrifuged again for 5 min at 2000 rpm. The resulting supernatant phase was used as NC ink for subsequent studies and LED device fabrication.

**Single Mode Size Distribution.** The precursor solution was prepared similar to the standard procedure, and the precursor-ligand ratios, reaction conditions and centrifugation speeds left unchanged. The amount of toluene in the pre-mix solution, however, was reduced from 5 mL to 3 mL. Also, the first NC precipitate was re-dispersed in 1.5 mL toluene to achieve a similar NC ink concentration as the standard procedure.

**Split Bimodal Size Distribution.** To achieve a split bimodal size distribution, 1-butanol was introduced as an additional precipitation agent during the NC synthesis. Here, 0.2 mL of 1-butanol was added to 2 mL of toluene in which the ligands are pre-mixed. The ligand-precursor ratios, and other reaction conditions remained unchanged. The NC purification protocol was similar to that used for the single mode size distribution.

## 5.3 Results and Discussion

### 5.3.1 Size Distribution Analysis

As discussed in Section 5.1, the size distribution of NCs in the NC inks can critically affect the radiative recombination in the formed NC thin films due to its influence on the trap density and film morphology. In addition, the smallest NCs in a size distribution could have larger band gaps due to quantum confinement which could funnel energy to the larger crystals with smaller band gaps. Various synthesis parameters such as the reaction temperature,[16] type of ligands,[17] amount of different solvents used in the synthesis,[2] etc. can be adjusted to modulate the NC sizes. Herein, two synthesis parameters were varied. Firstly, the amount of anti-solvent (toluene) used as anti-solvent to precipitate the NCs, was varied to influence the nucleation and growth of the NCs. By lowering the amount of toluene, the nucleation is increased, similar to the classical nucleation theory described by La Mer.[18] Moreover, as the ligand amount was kept constant, decrease in toluene volume also increases the ligand concentration in the solution, aiding NC capping and thereby restricting NC growth and agglomeration. Thus, a single mode size distribution centered at ~12 nm was achieved (Figure 5.1). The NC size distribution in the $CH_3NH_3PbBr_3$ NC inks were extracted from small-angle X-ray scattering (SAXS) measurements.

Secondly, besides lowering the toluene amount, a small amount of polar 1-butanol was introduced to the reaction mixture. The result of this experiment was a split bimodal size distribution with two discrete modes; the first mode was centered at approximately 16 nm, whereas the second mode displayed an average size of 70 nm, with almost no particles in the range 30 to 45 nm (Figure 5.1). The formation of the second mode is likely due to the partial removal of ligands by the polar solvent, leading to NC growth. In order to obtain NC inks of similar concentration, more toluene was used during NC purification to achieve a NC

ink concentration similar to that obtained for the standard narrow bimodal sample with modes at ~6nm and ~18 nm (concentration = 7.5 ± 0.5 mg $mL^{-1}$).

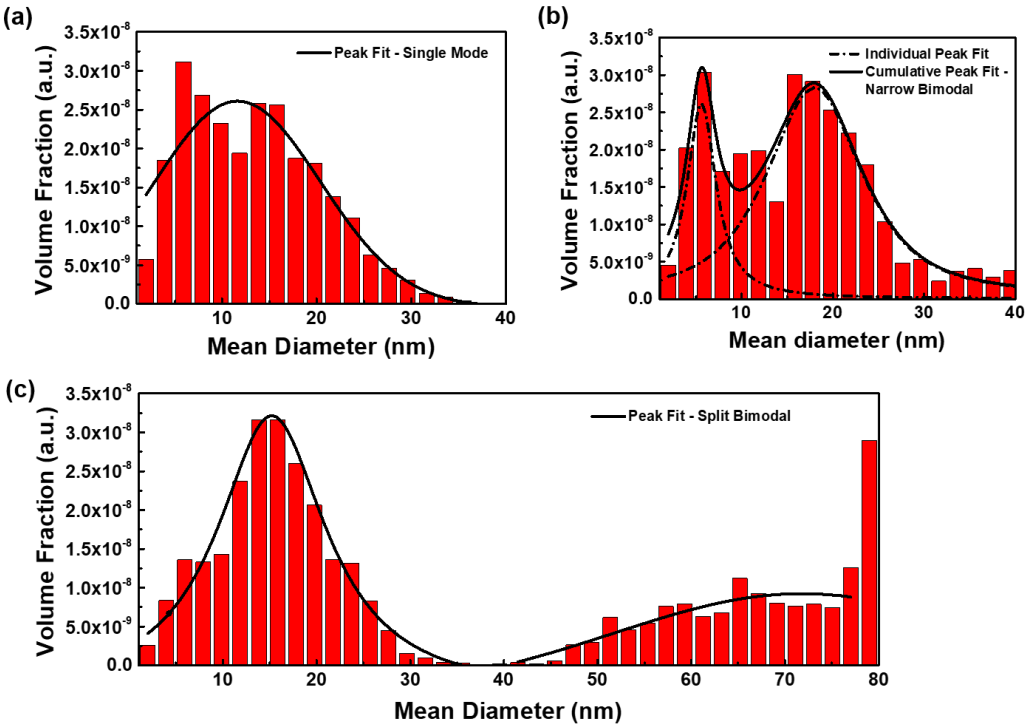


**Figure 5.1** Nanocrystal size distributions extracted from SAXS curves, depicted as volume fraction versus the mean particle diameter. (a) Single mode distribution; (b) narrow bimodal distribution; (c) split bimodal distribution. The peak fitting was performed using pseudo-Voigt profiles.

### 5.3.2 Structural and Topographical Characterization

The NC phase purity was confirmed using X-ray diffraction (XRD). All the characteristic peaks of the cubic perovskite phase were observed;[19] no additional peaks of secondary phases were detected for NC inks of all three size distributions (Figure 5.2).

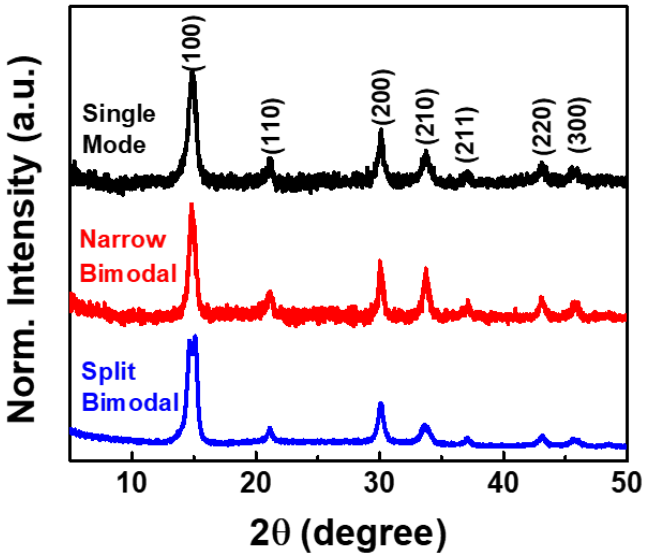


**Figure 5.2** XRD patterns obtained from drop casted $CH_3NH_3PbBr_3$ NC inks films on glass substrates.

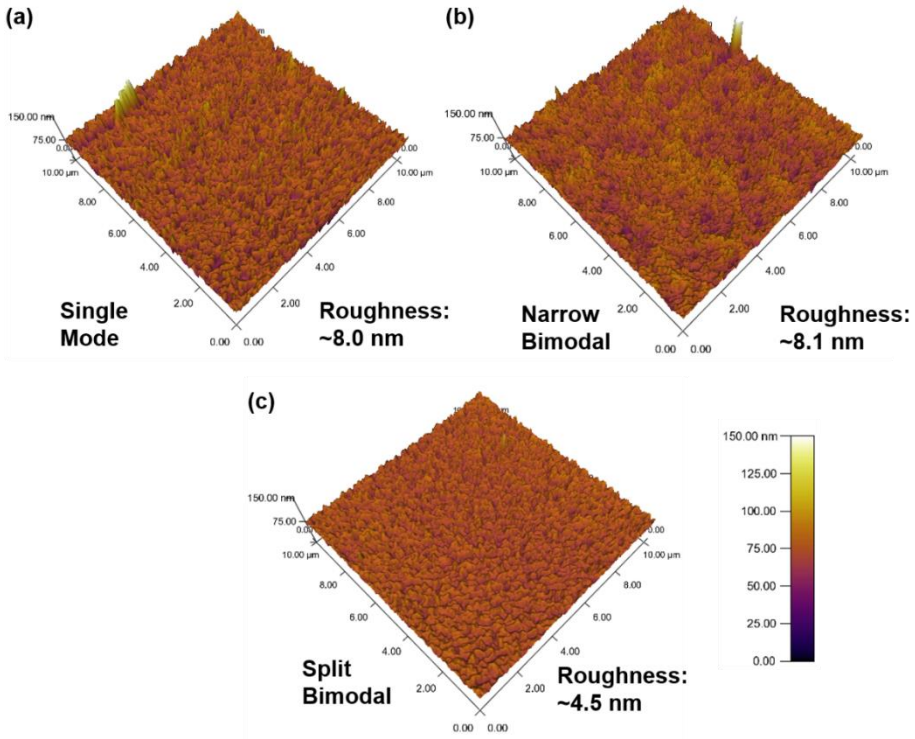


**Figure 5.3** 3D views of the AFM images and the corresponding rms roughness values for the (a) single mode, (b) narrow bimodal, and (c) split bimodal $CH_3NH_3PbBr_3$ NC size distributions (scan area = 100 $\mu m^2$).

To examine the surface topography of the NC films, spin coated thin NC films were measured using atomic force microscopy (AFM; Figure 5.3). A clear improvement in the surface coverage is observed for the split bimodal size distribution compared to the single mode and narrow bimodal size distributions, as evidenced from the decreased surface roughness. The root mean square (rms) roughness of the former is approximately 4.5 nm, as opposed to ca. 8 nm and 8.1 nm roughness for single mode and narrow bimodal size distributions, respectively.

### 5.3.3 Optical Characterization

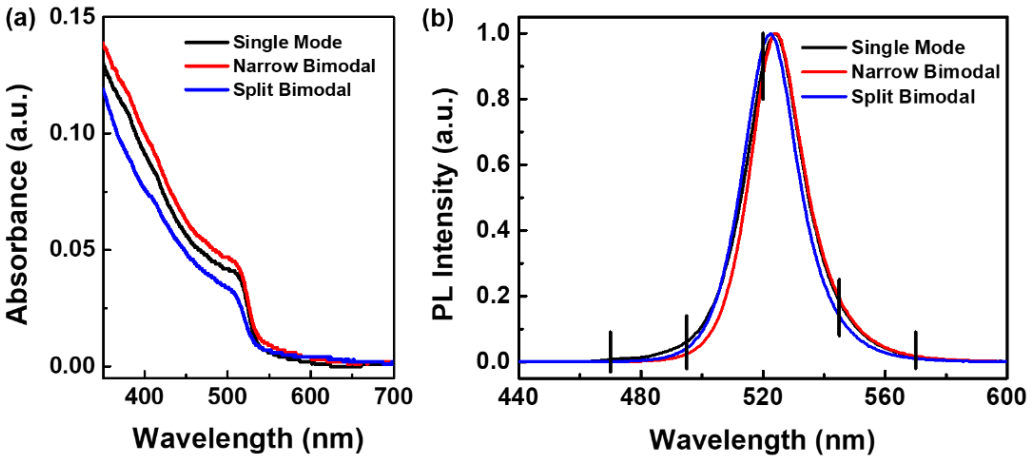


**Figure 5.4** Steady-state optical characteristics (a) absorbance and (b) PL spectra of NC inks of different size distributions. The emission wavelengths selected for TRPL measurements are marked with vertical black lines.

Optical characterization was conducted on thin films of the NC inks spin coated on glass substrates. Inks of all three distributions showed similar light absorption characteristics, without additional excitonic absorption peaks related to 2D or quasi-2D phases, (Figure 5.4-a) confirming the single-phase nature of the samples displayed in the XRD patterns. The absorption edge of ca. 535 nm for the NC inks corresponds to a band gap of ~2.3 eV. The photoluminescence spectra displayed a narrow emission peak (FWHM: 21-22 nm) with minimal shift

in the peak position, ca. 522.5-524 nm (Figure 5.4-b). As the majority of NCs in all size distributions have diameter larger than the reported Bohr diameters for $CH_3NH_3PbBr_3$ (ca. 3-6 nm),[4,6,20,21] no drastic shifts in the PL peak position are expected. However, the smaller diameter NCs (≤ 6 nm) is likely to display some confinement effects.[5,6] The latter was detected as small wavelength shifts at the base of the PL emission profile.

To elucidate the effect of the various NC sizes on the radiative recombination in the NC inks of different size distributions, time-resolved PL decay curves were obtained at different wavelengths within the PL emission profile (Figure 5.5 a-c). Five wavelengths, viz. 470 nm, 495 nm, 520 nm, 545 nm and 570 nm, were selected (indicated in Figure 5.4-b) for the wavelength-dependent measurements. The curves were fitted using a biexponential decay function, $I(t) = A_1 e^{\frac{-t}{\tau_1}} + A_2 e^{\frac{-t}{\tau_2}}$ where $\tau_1$, and $\tau_2$ represent the lifetimes for the different types of PL decays detected in the NC films and $A_1$ and $A_2$, are the respective decay amplitudes. The average lifetime is calculated as $\tau_{avg} = A_1\tau_2 + A_2\tau_2$ (Table 5.1). The fit convergence is represented by $R^2$, the closer the $R^2$value is to 1, the better the fit. The average PL lifetimes for the different NC size distributions were plotted as a function of emission wavelength (Figure 5.6).

PL decay curves at emission wavelengths of 470 and 495 nm, essentially probe band gaps of ~2.6 and ~2.5 eV, respectively. Previous studies on $CH_3NH_3PbBr_3$ NCs have shown that these PL emissions are exhibited by small NCs of < 2 nm and < 3 nm diameter, respectively, due to quantum confinement effects which widens the band gap.[16] At these wavelengths, the average PL lifetimes were very short, 3-9 ns, as the trap-assisted recombination component, $A_1$, was larger than bimolecular recombination component, $A_2$, likely due to the high surface-to-volume ratio for the small NCs. Moreover, the small NCs form only a small volume of the NCs in the different inks and most of the NCs have sizes beyond the quantum confinement regime. So, energy transfer (funneling) from the

smaller NCs with higher band gap to the larger NCs with comparatively smaller band gap, is likely, similar to observations with inorganic semiconductor NCs.[13,22,23]

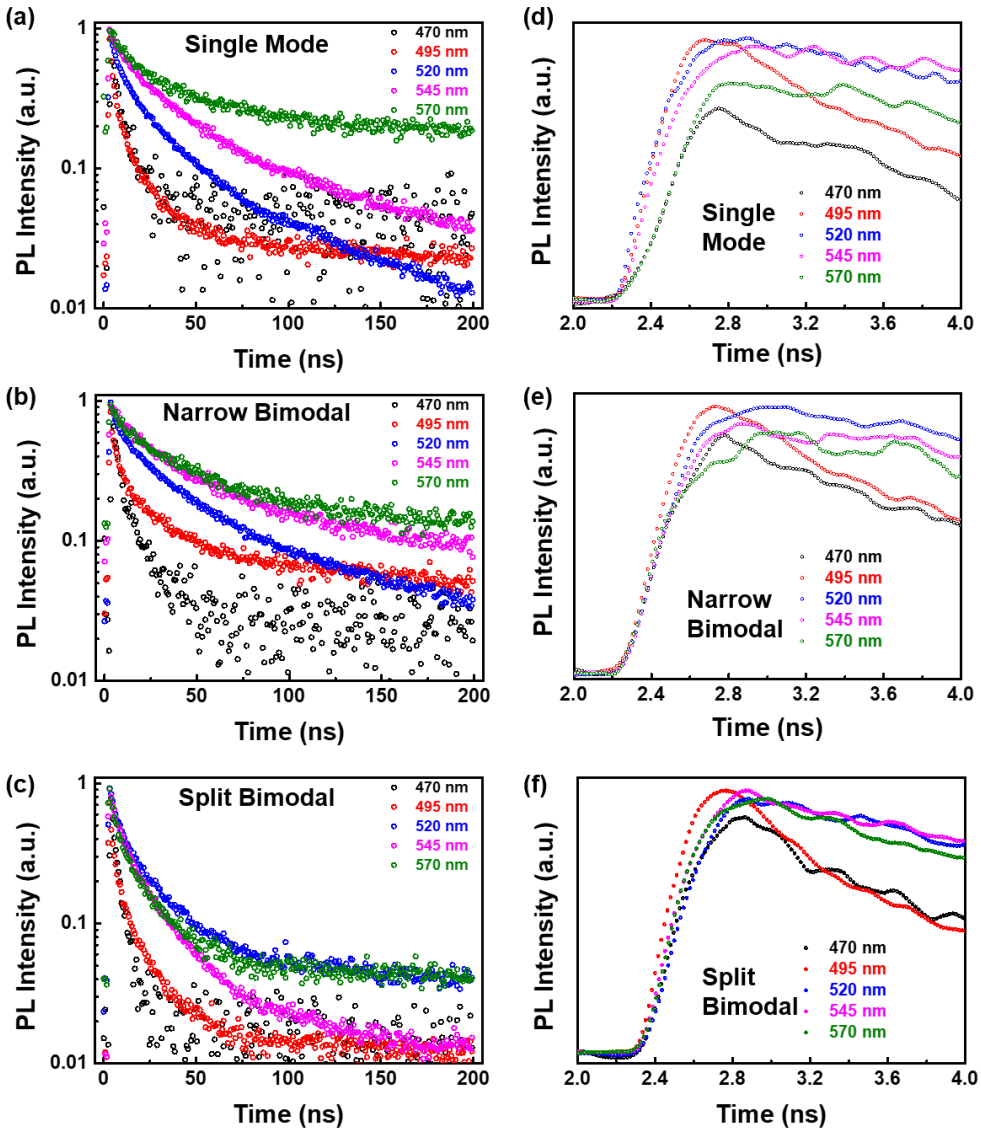


**Figure 5.5** (a-c) Normalized TRPL decay curves obtained at emission wavelengths 470, 495, 520, 545, and 570 nm, respectively, for the spin-coated NC inks with the different NC size distributions. (d-f) Zoom-in of the PL intensities at the first few ns, after excitation by the pulse laser, which illustrate the rise times at the different emission wavelengths.

**Table 5.1** Lifetimes obtained from the bi-exponential fitting of the TRPL decay curves at various PL emission wavelengths – 470 nm, 495 nm, 520 nm, 545 nm and 570 nm, for $CH_3NH_3PbBr_3$ inks with (a) single mode, (b) narrow bimodal, and (c) split bimodal NC size distributions.

**(a) Single Mode**

| **Wavelength (nm)** | $A_1$ **(%)** | $\tau_1$ **(ns)** | $A_2$ **(%)** | $\tau_2$ **(ns)** | $\tau_{avg}$ **(ns)** | $R^2$ |
|---|---|---|---|---|---|---|
| **470** | 0.60 | 1.73 | 0.40 | 9.49 | 4.81 | 0.938 |
| **495** | 0.70 | 1.54 | 0.30 | 11.96 | 4.69 | 0.996 |
| **520** | 0.54 | 4.6 | 0.46 | 30.47 | 16.42 | 0.999 |
| **545** | 0.41 | 7.76 | 0.59 | 40.84 | 27.38 | 0.998 |
| **570** | 0.47 | 8.46 | 0.53 | 42.80 | 26.73 | 0.985 |

**(b) Narrow Bimodal**

| **Wavelength (nm)** | $A_1$ **(%)** | $\tau_1$ **(ns)** | $A_2$ **(%)** | $\tau_2$ **(ns)** | $\tau_{avg}$ **(ns)** | $R^2$ |
|---|---|---|---|---|---|---|
| **470** | 0.65 | 1.99 | 0.35 | 11.17 | 5.19 | 0.978 |
| **495** | 0.69 | 2.08 | 0.31 | 23.55 | 8.74 | 0.990 |
| **520** | 0.45 | 4.72 | 0.55 | 37.80 | 23.01 | 0.998 |
| **545** | 0.37 | 8.21 | 0.63 | 44.26 | 30.99 | 0.995 |
| **570** | 0.39 | 7.73 | 0.61 | 43.86 | 29.88 | 0.988 |

**(c) Split Bimodal**

| **Wavelength (nm)** | $A_1$ **(%)** | $\tau_1$ **(ns)** | $A_2$ **(%)** | $\tau_2$ **(ns)** | $\tau_{avg}$ **(ns)** | $R^2$ |
|---|---|---|---|---|---|---|
| **470** | 0.56 | 1.15 | 0.44 | 5.58 | 3.09 | 0.984 |
| **495** | 0.70 | 1.08 | 0.30 | 10.63 | 3.91 | 0.996 |
| **520** | 0.52 | 3.57 | 0.48 | 22.17 | 12.48 | 0.998 |
| **545** | 0.52 | 3.92 | 0.48 | 20.02 | 11.63 | 0.999 |
| **570** | 0.58 | 3.37 | 0.42 | 18.25 | 9.65 | 0.997 |

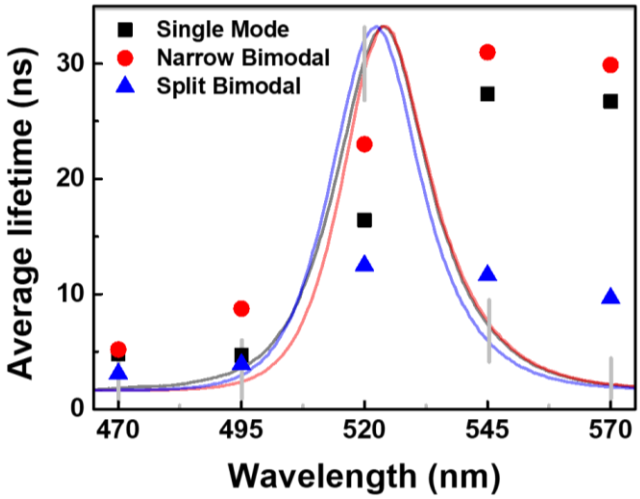


**Figure 5.6** Average PL lifetimes at the different probed wavelengths (represented by the grey vertical lines) within the PL emission profile for the single mode (black squares), narrow bimodal (red circles), and split bimodal (blue triangles) size distribution NC inks.

The longer rise times for the 520 nm (~2.38 eV) PL emission, compared to the 495 nm emission gives a clear indication of energy funneling in the NC inks with all the three size distributions (Figure 5.5 d-f). This also reflects as increase in the long-lived PL lifetimes at 520 nm compared to 470 and 495. In addition, as the NC size increases, the surface-to-volume ratio decreases, and therefore the contribution from surface traps also decreases, as reflected in the lower $A_1$ values (~0.5), at these wavelengths compared to the values at 470 and 495 nm emission (~0.7). Together, this led to an increase in average PL lifetime at 520 nm, which is close to the typical emission observed from the NC inks.

The PL lifetime continued to increase at longer wavelength for the single mode and narrow bimodal distributions which can be correlated to the funneling evident in these two distributions (rise times for 545 nm are longer than 520 nm). In contrast, the similar rise times at 520 and 545 nm wavelengths in case of split bimodal distribution indicate absence of funneling from NCs with ~2.38 eV band gap to ~2.27 eV band gap. The overall shorter life times for the split bimodal

distribution could be related to the reduction in funneling due to the lower volume of NCs in the quantum confined regime in this distribution compared to the single mode and narrow bimodal distribution.

Finally, the average lifetimes near the single crystalline band gap of $CH_3NH_3PbBr_3$ (~2.17 eV, ca. 570 nm wavelength emission),[24,25] were investigated for the NC inks with the different NC size distributions. Here, the average lifetime is similar to that at 545 nm wavelength for all three NC size distributions. The rise time curves implied that there was funneling until the smallest band gap for the single mode and narrow bimodal distributions, resulting in long life times at 570 nm. For split bimodal, no funneling was detected at 570 nm and average PL lifetime was also short. Interestingly, the large diameter NCs in the second half of the split bimodal distribution does not seem to play any significant role in the radiative recombination dynamics.

### 5.3.2 LED Characterization

To investigate the effect of the different NC size distributions on the EL performance, LEDs were fabricated with the NC inks (conc. 7.5 ± 0.5 mg $mL^{-1}$) forming the emission layer. The device stack employed was ITO/ PEDOT:PSS/ $CH_3NH_3PbBr_3$ NC/ PO-T2T/ Ca/ Al. The current volatge characterisitics, luminescence intensity, and turn-on voltages, were similar for all three cases, as illustrated in Figure 5.7-a. A single EL emission peak with maximum centred at 521 ± 1 nm was obtained in case of all three NC size distributions(Figure 5.7-b). The current efficiency improved for the NC ink with the split bimodal distribution compared to the single mode and split bimodal size distributions, which consequently led to an improvement in EQE (Figure 5.7-c,d). The device performance comparison is summarized in Table 5.2.

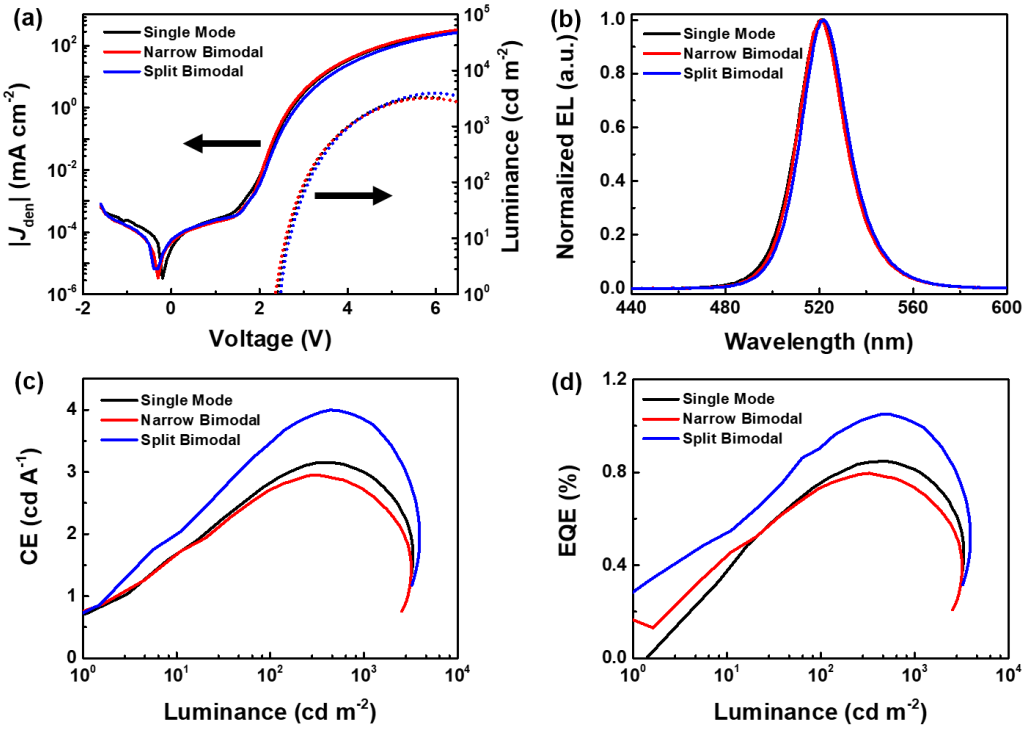


**Figure 5.7** LED characteristic curves for the single mode (black), narrow bimodal (red) and split bimodal (blue) distributions of the $CH_3NH_3PbBr_3$ NCs (a) J-V-L curves; solid lines depict current density versus voltage whereas the dotted lines depict luminance versus voltage. (b) EL spectra. (c) CE versus luminance. (d) EQE versus luminance.

**Table 5.2** Comparison of LED characteristics for the different $CH_3NH_3PbBr_3$ NC size distributions. Specifically, turn-on voltage ($V_T$, defined as the voltage at which 1 cd $m^{-2}$ luminance is achieved), maximum current efficiency (CE), maximum power efficiency (PE), maximum external quantum efficiency (EQE), maximum luminance ($L_{max}$), and EL peak positions are tabulated.

| Size Distribution | $V_T$ (V) | Max CE (cd $A^{-1}$) | Max PE (lm $W^{-1}$) | EQE (%) | $L_{max}$ (cd $m^{-2}$) | EL Peak (nm) |
|---|---|---|---|---|---|---|
| **Single Mode** | 2.4 | 3.15 | 2.96 | 0.85 | 3328 | 521.1 |
| **Narrow Bimodal** | 2.4 | 2.95 | 2.85 | 0.80 | 3193 | 521.0 |
| **Split Bimodal** | 2.5 | 4.12 | 3.68 | 1.05 | 3934 | 522.3 |

The higher current efficiency for the split bimodal distribution NC inks is likely related to the slight increase in luminance observed, as the J-V curves for the inks of all three size distributions display similar (almost overlapping) curves. It is noted, however, that luminance drop at higher voltage is less severe in case of the NC ink with split bimodal size distribution compared to the single mode and narrow bimodal size distributions.

Besides luminescence intensity and EQE, operational stability is a pre-requisite for practical device application. The poor moisture stability of perovskite materials is well known.[26-28] This can be overcome by preparing the LEDs inside an Ar glove box and encapsulating the devices prior to testing the LED under ambient conditions. However, other factors such as thermal instability of the $CH_3NH_3PbBr_3$ and the organic transport layers (i.e. thermalization during device operation due to current flow),[29], as well as ion migration between the different layers in the device stack,[30] can lead to device degradation.

These factors can be influenced by the NC size distribution because of two reasons. Firstly, smaller sized NCs would lead to more grain boundaries and thereby, more defect states (trap states). [31] The increase in defect states can increase ion migration issues as well as the trap-assisted non-radiative recombination can aggravate device heating problems. Secondly, funneling would localize the recombination at the lower band gap NCs, which can decrease the operating voltage required to attain high luminance,[14] but could also localize heating in the device, accelerating material degradation. To compare the stability of the LEDs made from inks with different size distributions of $CH_3NH_3PbBr_3$ NCs, multiple voltage sweep and constant current operation tests were conducted (see experimental details in Chapter 3).

Under repeated voltage sweeps from -1.5 V to 4 V, the luminance declined for all the devices with each consecutive run (Figure 5.8 a-c). Nonetheless, the

luminance drop observed for the split bimodal distribution is smaller compared to the single mode and narrow bimodal size distributions.

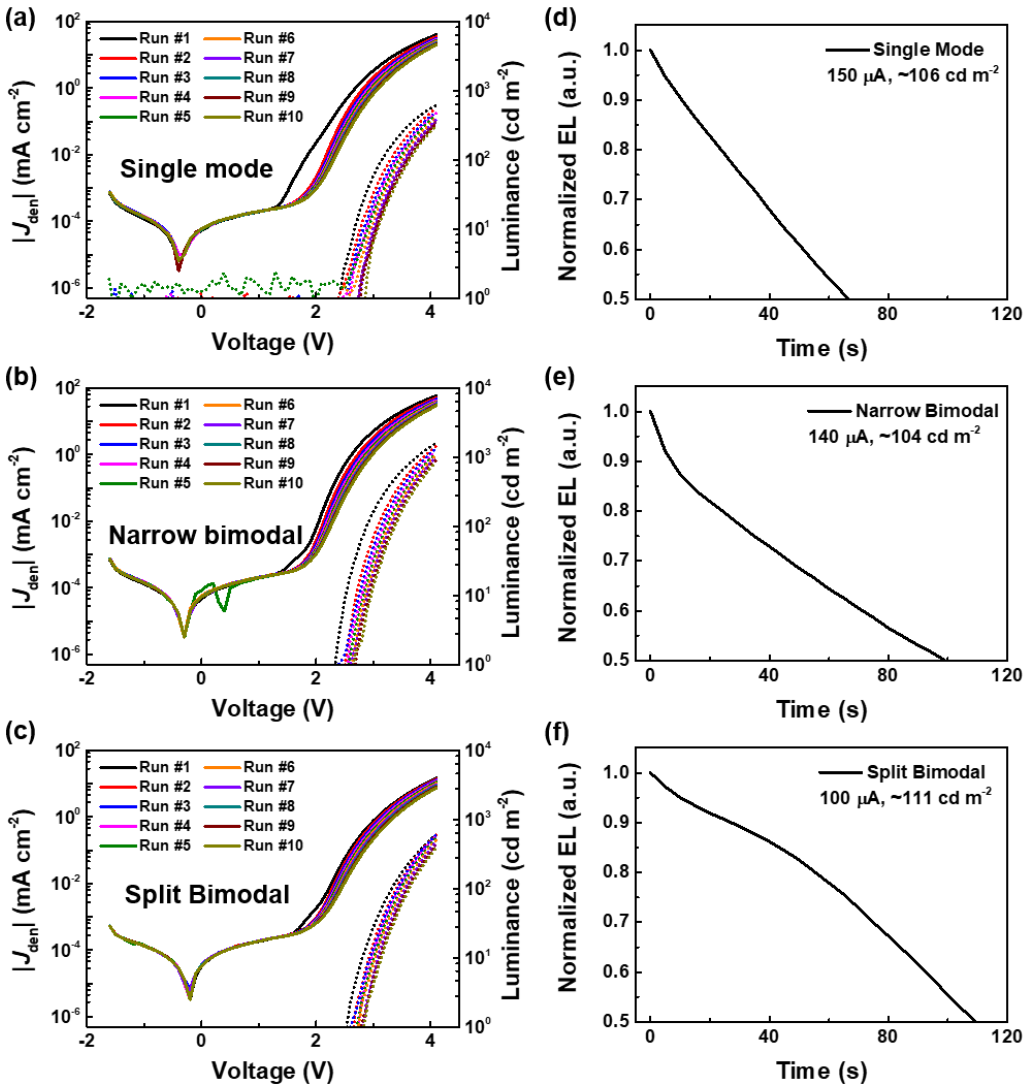


**Figure 5.8** Device stability tests. (a-c) J-V-L curves from multiple voltage sweeps and (d-f) Normalized EL versus device operation time at constant current, for the single mode, narrow bimodal, and split bimodal size distributions, respectively.

Under constant current operation (Figure 5.8 d-f), the single mode size distribution yielded the worst performance, with a luminance half-life time (i.e. time necessary to reduce luminance to half its initial value) of just 67 s. The bimodal distributions displayed better stability: the narrow bimodal device

displayed a half-life time of 99 s, while the split bimodal sample endured 109 s before the luminance dropped by 50%.

The shorter luminance half-life in case of single mode size distribution of NCs compared to the narrow bimodal distribution can be correlated to the higher trap-assisted recombination observed from the TRPL studies (Table 5.1), which indicated more defects were present in the former. In case of the split bimodal distribution, absence of funneling at 545 and 570 nm wavelengths, (Figure 5.6) may have reduced the heating effects. This is corroborated by the lower current required to attain the 100 cd $m^{-2}$ luminance for this NC size distribution (Figure 5.8 d-f), and the slower decay of luminance at high voltages (Figure 5.7 a), as well as under repeated voltage sweeps (Figure 5.8 a-c). Thus, quick recombination of the electron-hole pair (indicated by the short radiative recombination lifetimes) for the split bimodal NC size distribution was demonstrated to be beneficial for increased device stability.

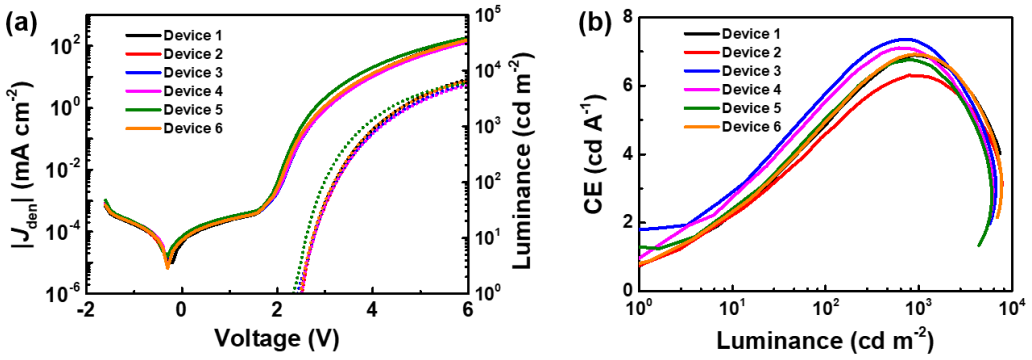


**Figure 5.9** (a) J-V-L curves and (b) CE versus luminance curves for devices made from higher concentration $CH_3NH_3PbBr_3$ NCs inks with a split bimodal NC size distribution.

Since the split bimodal distribution showed the best stability and performance, NC inks of higher concentration, ~12 mg $mL^{-1}$ were prepared. A higher ink concentration was postulated to attain thicker and denser NC film, thereby enhancing the EL brightness. Subsequent device fabrication demonstrated LEDs

with a max. luminance > 7700 cd $m^{-2}$ and max. CE > 7 cd $A^{-1}$ (max. EQE = 1.89%) (Figure 5.9).

## 5.4 Conclusion

Three types of $CH_3NH_3PbBr_3$ NC inks exhibiting a single mode, narrow bimodal, and split bimodal size distributions, respectively, were synthesized. The different NC size distributions were achieved by manipulating two synthesis parameters, (1) varying the quantity of anti-solvent (toluene) and (2) introducing an aliphatic alcohol (1-butanol) during the NC formation, while ensuring that the inks have similar concentrations. The NC inks displayed almost identical steady-state optical characteristics; only minor deviations were observed in the steady state PL. However, the time-resolved PL measurements at various wavelengths within the PL emission profile revealed significant differences in the PL decay lifetimes. The average lifetime was more homogenous for the split bimodal size distribution wherein the longest decay time was ca. 12.5 ns and funneling was not observed at 545 and 570 nm wavelengths. The NC inks with the aforementioned size distribution also displayed the lowest surface roughness upon film formation as measured by AFM. The fast radiative recombination and smooth NC film resulted in better LED efficiency and stability for the NC ink with split bimodal NC size distribution compared to the single mode and narrow bimodal distributions. Subsequently, NC inks of higher concentration bearing the split bimodal NC size distribution were prepared to further improve the luminance and thereby the efficiency of the LEDs.

## 5.5 References

1 Xing, J. *et al.* High-Efficiency Light-Emitting Diodes of Organometal Halide Perovskite Amorphous Nanoparticles. *ACS Nano* **10**, 6623-6630, doi:10.1021/acsnano.6b01540 (2016).

2 Huang, H. *et al.* Emulsion Synthesis of Size-Tunable $CH_3NH_3PbBr_3$ Quantum Dots: An Alternative Route toward Efficient Light-Emitting Diodes. *ACS Applied Materials & Interfaces* **7**, 28128-28133, doi:10.1021/acsami.5b10373 (2015).

3 Zhang, F. *et al.* Brightly Luminescent and Color-Tunable Colloidal $CH_3NH_3PbX_3$ (X = Br, I, Cl) Quantum Dots: Potential Alternatives for Display Technology. *ACS Nano* **9**, 4533-4542, doi:10.1021/acsnano.5b01154 (2015).

4 Sichert, J. A. *et al.* Quantum Size Effect in Organometal Halide Perovskite Nanoplatelets. *Nano Letters* **15**, 6521-6527, doi:10.1021/acs.nanolett.5b02985 (2015).

5 Hassan, Y. *et al.* Structure-Tuned Lead Halide Perovskite Nanocrystals. *Adv Mater* **28**, 566-573, doi:10.1002/adma.201503461 (2016).

6 Kumar, P., Muthu, C., Nair, V. C. & Narayan, K. S. Quantum Confinement Effects in Organic Lead Tribromide Perovskite Nanoparticles. *The Journal of Physical Chemistry C* **120**, 18333-18339, doi:10.1021/acs.jpcc.6b06545 (2016).

7 Kim, J., Lee, S.-H., Lee, J. H. & Hong, K.-H. The Role of Intrinsic Defects in Methylammonium Lead Iodide Perovskite. *The Journal of Physical Chemistry Letters* **5**, 1312-1317, doi:10.1021/jz500370k (2014).

8 Wu, X. *et al.* Trap States in Lead Iodide Perovskites. *Journal of the American Chemical Society* **137**, 2089-2096, doi:10.1021/ja512833n (2015).

9 Cho, H. *et al.* Overcoming the electroluminescence efficiency limitations of perovskite light-emitting diodes. *Science* **350**, 1222-1225, doi:10.1126/science.aad1818 (2015).

10 Yu, J. C. *et al.* Enhancing the Performance and Stability of Perovskite Nanocrystal Light-Emitting Diodes with a Polymer Matrix. *Advanced Materials Technologies*, n/a-n/a, doi:10.1002/admt.201700003 (2017).

11 Yantara, N. *et al.* Inorganic Halide Perovskites for Efficient Light-Emitting Diodes. *The Journal of Physical Chemistry Letters* **6**, 4360-4364, doi:10.1021/acs.jpclett.5b02011 (2015).

12 Salim, T. *et al.* Perovskite-based solar cells: impact of morphology and device architecture on device performance. *Journal of Materials Chemistry A* **3**, 8943-8969, doi:10.1039/C4TA05226A (2015).

13 Klar, T. A., Franzl, T., Rogach, A. L. & Feldmann, J. Super-Efficient Exciton Funneling in Layer-by-Layer Semiconductor Nanocrystal Structures. *Advanced Materials* **17**, 769-773, doi:10.1002/adma.200401675 (2005).

14 Quan, L. N. *et al.* Tailoring the Energy Landscape in Quasi-2D Halide Perovskites Enables Efficient Green-Light Emission. *Nano Letters* **17**, 3701-3709, doi:10.1021/acs.nanolett.7b00976 (2017).

15 Zhao, L. *et al.* Electrical Stress Influences the Efficiency of CH3NH3PbI3 Perovskite Light Emitting Devices. *Advanced Materials*, n/a-n/a, doi:10.1002/adma.201605317 (2017).

16 Huang, H., Susha, A. S., Kershaw, S. V., Hung, T. F. & Rogach, A. L. Control of Emission Color of High Quantum Yield CH3NH3PbBr3 Perovskite Quantum Dots by Precipitation Temperature. *Adv Sci (Weinh)* **2**, 1500194, doi:10.1002/advs.201500194 (2015).

17 Pan, A. *et al.* Insight into the Ligand-Mediated Synthesis of Colloidal $CsPbBr_3$ Perovskite Nanocrystals: The Role of Organic Acid, Base, and Cesium Precursors. *ACS Nano* **10**, 7943-7954, doi:10.1021/acsnano.6b03863 (2016).

18 LaMer, V. K. & Dinegar, R. H. Theory, Production and Mechanism of Formation of Monodispersed Hydrosols. *Journal of the American Chemical Society* **72**, 4847-4854, doi:10.1021/ja01167a001 (1950).

19 Poglitsch, A. & Weber, D. Dynamic disorder in methylammoniumtrihalogenoplumbates (II) observed by millimeter -

wave spectroscopy. *The Journal of Chemical Physics* **87**, 6373-6378, doi:10.1063/1.453467 (1987).

20 Tanaka, K. *et al.* Comparative study on the excitons in lead-halide-based perovskite-type crystals CH3NH3PbBr3 CH3NH3PbI3. *Solid State Communications* **127**, 619-623, doi:10.1016/S0038-1098(03)00566-0 (2003).

21 Koutselas, I. B., Ducasse, L. & Papavassiliou, G. C. Electronic properties of three- and low-dimensional semiconducting materials with Pb halide and Sn halide units. *Journal of Physics: Condensed Matter* **8**, 1217 (1996).

22 Xu, F. *et al.* Efficient Exciton Funneling in Cascaded PbS Quantum Dot Superstructures. *ACS Nano* **5**, 9950-9957, doi:10.1021/nn203728t (2011).

23 Akhavan, S., Cihan, A. F., Bozok, B. & Demir, H. V. Nanocrystal Skins with Exciton Funneling for Photosensing. *Small* **10**, 2470-2475, doi:10.1002/smll.201303808 (2014).

24 Shi, D. *et al.* Low trap-state density and long carrier diffusion in organolead trihalide perovskite single crystals. *Science* **347**, 519-522, doi:10.1126/science.aaa2725 (2015).

25 Saidaminov, M. I. *et al.* High-quality bulk hybrid perovskite single crystals within minutes by inverse temperature crystallization. *Nature Communications* **6**, 7586, doi:10.1038/ncomms8586 (2015).

26 Burschka, J. *et al.* Sequential deposition as a route to high-performance perovskite-sensitized solar cells. *Nature* **499**, 316-319, doi:10.1038/nature12340 (2013).

27 Niu, G. *et al.* Study on the stability of CH3NH3PbI3 films and the effect of post-modification by aluminum oxide in all-solid-state hybrid solar cells. *Journal of Materials Chemistry A* **2**, 705-710, doi:10.1039/C3TA13606J (2013).

28 Yip, H.-L. & Jen, A. K. Y. Recent advances in solution-processed interfacial materials for efficient and stable polymer solar cells. *Energy*

*& Environmental Science* **5**, 5994-6011, doi:10.1039/C2EE02806A (2012).

29 Kulbak, M. *et al.* Cesium Enhances Long-Term Stability of Lead Bromide Perovskite-Based Solar Cells. *The Journal of Physical Chemistry Letters* **7**, 167-172, doi:10.1021/acs.jpclett.5b02597 (2016).

30 Back, H. *et al.* Achieving long-term stable perovskite solar cells via ion neutralization. *Energy & Environmental Science* **9**, 1258-1263, doi:10.1039/C6EE00612D (2016).

31 Wo, S., Headrick, R. L. & Anthony, J. E. Fabrication and characterization of controllable grain boundary arrays in solution-processed small molecule organic semiconductor films. *Journal of Applied Physics* **111**, 073716, doi:10.1063/1.3698203 (2012).

# Chapter 6

# Comparison of Methylammonium and Formamidinium Lead Bromide Perovskites Focused on LED Application

*In this chapter, formamidinium lead bromide perovskite ($FAPbBr_3$) nanocrystal (NC) inks were synthesized using the protocol optimized for methylammonium lead bromide ($MAPbBr_3$) NC inks (as described in the previous chapter). Thereafter, the optical and structural properties and LED performances of the NCs were compared. Despite the higher luminance for the $FAPbBr_3$-based LEDs compared to $MAPbBr_3$-based LEDs, the efficiencies were lower; possibly due to the poor charge injection into the $FAPbBr_3$ NCs. Subsequently, the $FAPbBr_3$ NC synthesis was optimized by varying the ligand amount whereby a quasi-2D phase was formed in the NC ink. Charge funneling from the higher band gap quasi-2D to the lower band gap 3D phase improved the carrier injection in $FAPbBr_3$-based LEDs and increased the device efficiency exceptionally. Similar improvements, however, could not be achieved when a similar protocol was used for $MAPbBr_3$ NCs, emphasizing that the synthesis optimization needs to be material-specific.*

## 6.1 Introduction

The formation of the three-dimensional cubic perovskite crystal structure $ABX_3$ requires that the radius of the A, B and X ions, $r_A$, $r_B$, and $r_X$, respectively, satisfy the Goldschmidt tolerance factor, $0.9 < t < 1.0$, wherein, $t = r_A + r_X / \sqrt{2}(r_B + r_X)$.[1] Theoretically, there are many organic cations such as methylammonium $[CH_3NH_3]^+$, hydrazinium $[H_3N–NH_2]^+$, formamidinium $[CH(NH_2)_2]^+$, azetidinium $[(CH_2)_3NH_2]^+$ , imidazolium $[C_3N_2H_5]^+$, etc. which can satisfy this condition.[1,2] However, due to the experimental challenges in preparing the different compounds, only two organic cations, methylammonium $[CH_3NH_3]^+$ and formamidinium $[CH(NH_2)_2]^+$, are currently studied extensively.

Both these cations have shown exceptional photovoltaic performances, and a methylammonium-formamidinium mixed cation perovskite solar cell holds the current record for highest certified power conversion of ~20%.[3,4] Due to difficulties in stabilizing the formamidinium lead iodide perovskite phase at room temperature, methylammonium cations remained more popular in the photovoltaic field.[5] Consequently, when researchers started developing perovskite-based light emitting diodes (LEDs), the first reports were based on methylammonium cations.[6-10] For the LED applications, however, bromide perovskites, which typically give green luminescence, are extensively investigated rather than the larger band gap (red and near IR luminescence) iodide perovskites. Since the formamidinium cations can also form stable bromide perovskite structures at room temperature, formamidinium-based LEDs were also reported soon enough.[11-13] Moreover, the higher thermal stability of formamidinium-based systems compared to the methylammonium based ones, have led to an increase in interest in the former.[13-15] In this chapter, the effect on replacing methylammonium with formamidinium in the NC ink synthesis protocol optimized in Chapter 5, on the optical properties and crystal structure of the NCs and subsequently their LED performances, were investigated.

## 6.2 Materials and Synthesis Protocol

### 6.2.1 Materials

Methylammonium bromide (Dyesol), formamidinium bromide (Dyesol), lead bromide (TCI), *N*,*N*-dimethylformamide (DMF; Sigma Aldrich; anhydrous, 99.8%), toluene (Sigma Aldrich; anhydrous, 99.8%), 1-butanol (Sigma Aldrich; anhydrous, 99.8%), *n*-octylamine (Aldrich; 99%), and oleic acid (Fluka; Ph. Eur) were used to prepare the perovskite NCs. All chemicals were used as received, without any further purification. Poly(3,4-ethylenedioxythiophene)-poly(styrenesulfonate) (PEDOT:PSS; Heraeus, Al 4083), 2,4,6-Tris[3-(diphenylphosphinyl)phenyl]-1,3,5-triazine (PO-T2T; Lumtec), Ca, and Al, were used as hole-transporting layer (HTL), electron-transporting layer (ETL), and top electrodes, respectively. The electron transport and top electrode materials were stored and handled in Ar atmosphere. UV curing adhesive (Lumtec; epoxy resin/polymer) was used to encapsulate the LEDs.

### 6.2.2 Synthesis and NC purification.

**Protocol 1:** Both $CH(NH_2)_2PbBr_3$ and $CH_3NH_3PbBr_3$ NCs were synthesized using the ligand-assisted reprecipitation (LARP) method. Herein, the protocol for achieving the split bimodal NC size distribution (described in Chapter 5) was followed. Briefly, $CH_3NH_3Br$ (0.086 mmol; 9.6 mg) or $CH(NH_2)_2PbBr_3$ (0.086 mmol; 10.7 mg) and lead bromide ($PbBr_2$; 0.075 mmol; 27.5 mg) precursors were dissolved in 250 µL DMF. This precursor solution was swiftly injected into 2 mL toluene under vigorous stirring, in which 12.4 µL of *n*-octylamine, 500 µL of oleic acid and 0.2 mL of 1-butanol were pre-mixed. The reaction, carried out at room temperature under ambient conditions (60% relative humidity), was continued for 1 min. The colloidal NC solutions obtained were then centrifuged for 5 min at 6000 rpm (10 mins in case of $CH(NH_2)_2PbBr_3$, to separate the supernatant and precipitated phases). After discarding the supernatant, the

precipitate was re-dispersed in 1 mL toluene. This dispersion was centrifuged for 5 min at 2000 rpm and the resulting supernatant phase was used as NC ink for subsequent studies and LED device fabrication.

**Protocol 2:** The LARP method is also used for this synthetic protocol; where the ligand and precursor concentrations are adjusted and the purification process is also slightly modified. Briefly, 0.2 mmol of FABr and 0.1 mmol of $PbBr_2$ were dissolved in 250 µL of DMF and subsequently 150 µL was added dropwise into a vigorously stirred solution containing 5 mL toluene, 5-50 µL *n*-octylamine (*n*-octylamine:$PbBr_2$ varied from 3:1 to 10:1), 0.3 mL oleic acid, and 2 mL 1-butanol. After reaction, the NC solution was purified by first centrifugation for 10 mins at 14680 rpm, after which the supernatant phase was discarded and the precipitate re-dispersed in 1 mL of toluene. In the second centrifugation step, the re-dispersed NCs were centrifugated at 3750 rpm. The resultant supernatant phase formed the NC ink.

## 6.3 Results and Discussion

### 6.3.1 Comparison of Optical Properties and Crystal Structure

The fundamental optical properties and crystal structure of the lead bromide perovskite NCs synthesized from $CH_3NH_3Br$ and $CH(NH_2)_2Br$ precursors, using Protocol 1 optimized for $CH_3NH_3PbBr_3$ NC synthesis (Chapter 5), were compared. The absorption spectra revealed an absorption edge around 536-537 nm for both $CH_3NH_3PbBr_3$ (denoted as $MAPbBr_3$) and $CH(NH_2)_2PbBr_3$ (denoted as $FAPbBr_3$) NC thin films (Figure 6.1-a), corresponding to an optical band gap of ~2.3 eV. The PL peak maxima wavelength for $FAPbBr_3$ were red-shifted (529.5 nm) compared to $MAPbBr_3$ (523 nm), similar to previous reports, indicating the band gap is slightly smaller for the former (Figure 6.1-b). The narrow PL emission, full width half maximum (FWHM) of 21.6 nm and 21.9 nm

for $MAPbBr_3$ and $FAPbBr_3$, respectively, confirm the formation of NCs of high color purity in both cases.

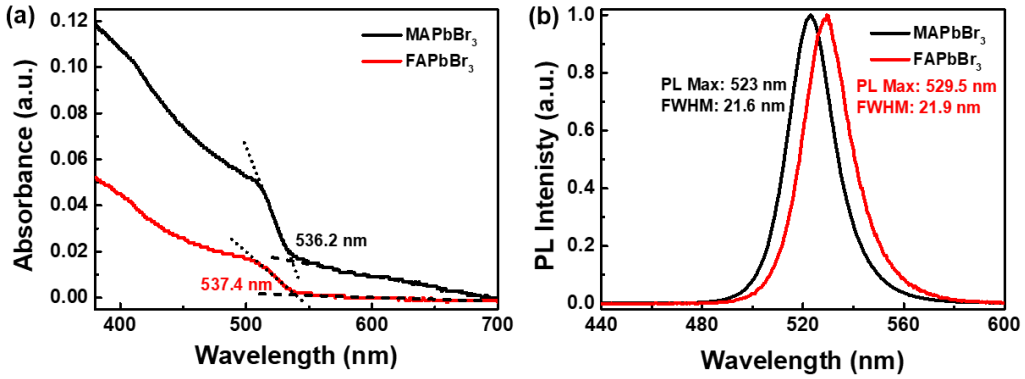


**Figure 6.1** (a) Absorbance and (b) PL spectra of $MAPbBr_3$ (black) and $FAPbBr_3$ (red) NC thin films, respectively. The intersection of the dashed and dotted lines in (a) indicates the absorption edge wavelength.

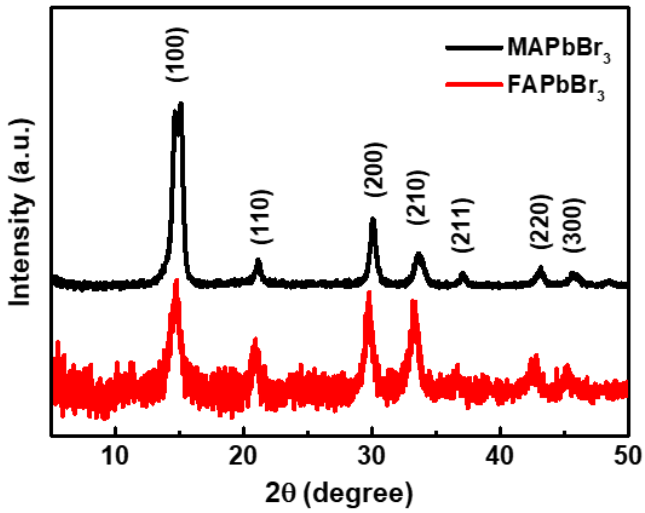


**Figure 6.2** Comparison of XRD diffraction patterns of $MAPbBr_3$ (black) and $FAPbBr_3$ (red) NC films, respectively.

The crystal structure for the two NC inks were analyzed by X-ray diffraction (XRD) (Figure 6.2). The major diffraction peaks, correspond to the (100), (110), (200), (210), (211), (220), and (300) lattice planes, for both the $MAPbBr_3$ and $FAPbBr_3$ NCs, confirming the Pm-3m cubic perovskite structure for both.[14,16]

### 6.3.2 LED Characterization

LEDs were fabricated by spin coating the NC inks to form compact emission layers on top of ITO/PEDOT:PSS, which act as anode and HTL, respectively. Subsequently, thin layers of PO-T2T (ETL) and Ca/Al were evaporated (cathode) to complete the device stack. A similar device architecture was used for LED fabrication in Chapter 5.

Similar to the PL emission, the EL emission from $FAPbBr_3$, was red-shifted compared to $MAPbBr_3$ emission (Figure 6.3). Furthermore, the EL peak of $FAPbBr_3$ (532.2 nm) was more red-shifted than its PL peak (529.5 nm), indicating that the electronic band gap is smaller than the optical band gap. In the case of $MAPbBr_3$, as described in previous Chapters, the EL peak differs < 1 nm from the PL peak, such that the electronic and optical band gaps are near-identical.

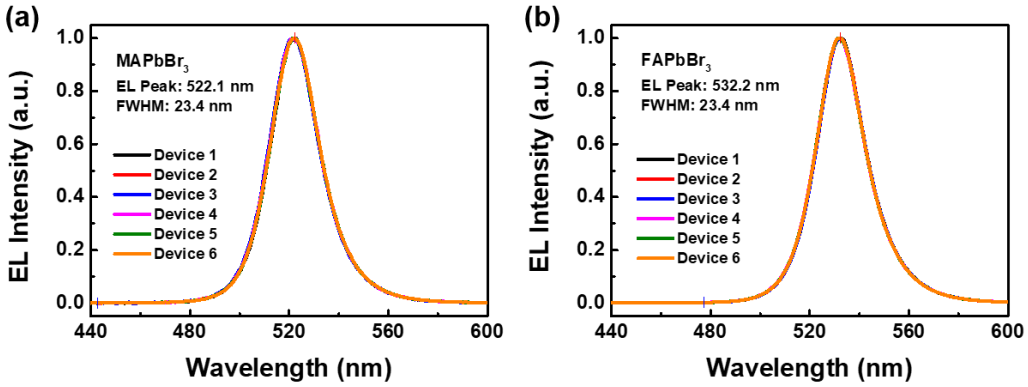


**Figure 6.3** EL as function of emission wavelength for LEDs based on (a) $MAPbBr_3$ and (b) $FAPbBr_3$ emission layers.

As seen from the J-V-L curves (Figure 6.4-a,b), both $MAPbBr_3$ and $FAPbBr_3$ based LEDs display good diode behavior implying good surface coverage of the respective NC thin films. However, the current density at the turn-on condition (when a luminance of 1 cd $m^{-2}$ is achieved), is higher (~0.5 mA $cm^{-2}$) for $FAPbBr_3$ compared to $MAPbBr_3$ (~0.1 mA $cm^{-2}$) as depicted in the luminance versus

current density curves (Figure 6.4-c,d). In addition, the lower turn-on voltage expected for $FAPbBr_3$ from the lower band gap indicated in the EL and PL spectra, was not observed; both $MAPbBr_3$ and $FAPbBr_3$ based LEDs turned on at approx. 2.4 V. These results indicate poorer charge injection in the $FAPbBr_3$ based LEDs compared to the $MAPbBr_3$ based LEDs.

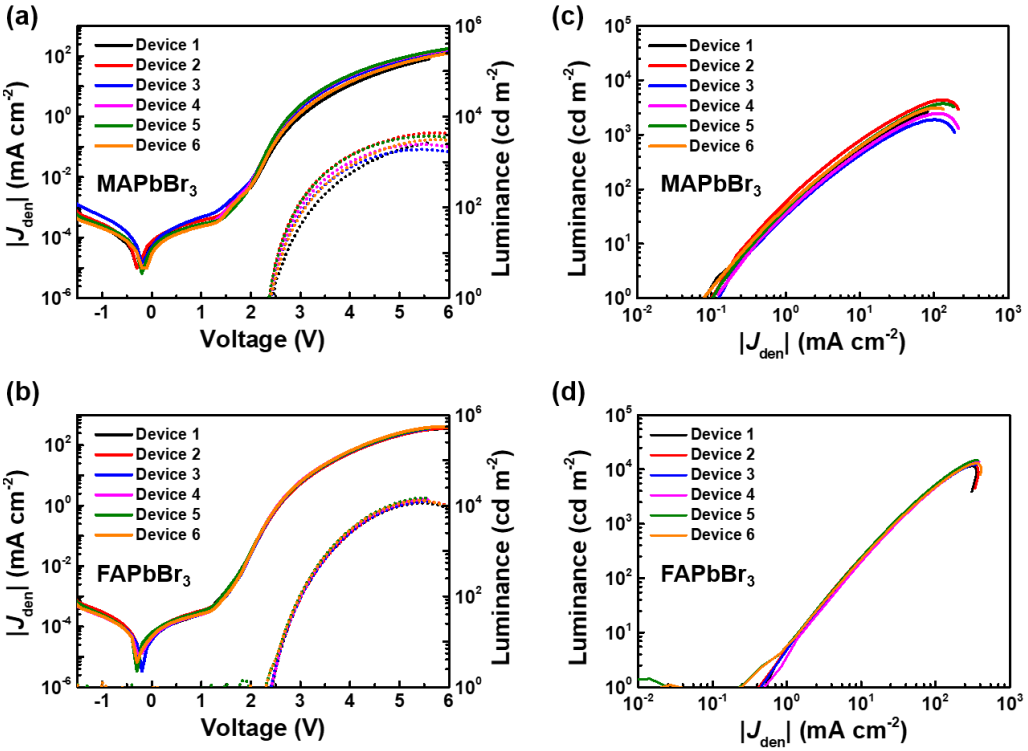


**Figure 6.4** (a,b) J-V-L and luminance versus current density curves, respectively, of $MAPbBr_3$-based LEDs. (c,d) J-V-L and luminance versus current density curves, respectively, of $FAPbBr_3$-based LEDs.

The luminance drop-off at high voltages during voltage sweep measurements is related device heating at high current densities.[6] A comparison of the J-V-L curves (Figure 6.4-a,b) shows that the slope of the L-V curve starts to decline at lower voltages for $MAPbBr_3$ compared to $FAPbBr_3$.and the current densities were much lower for $MAPbBr_3$ devices compared to $FAPbBr_3$ devices. This evidences the higher thermal stability of $FAPbBr_3$ compared to $MAPbBr_3$. The superior thermal stability.is most likely the reason why higher luminance could be attained

with $FAPbBr_3$ (> 10,000 cd $m^{-2}$) compared to that with $MAPbBr_3$ emission layer (~4,000 cd $m^{-2}$).

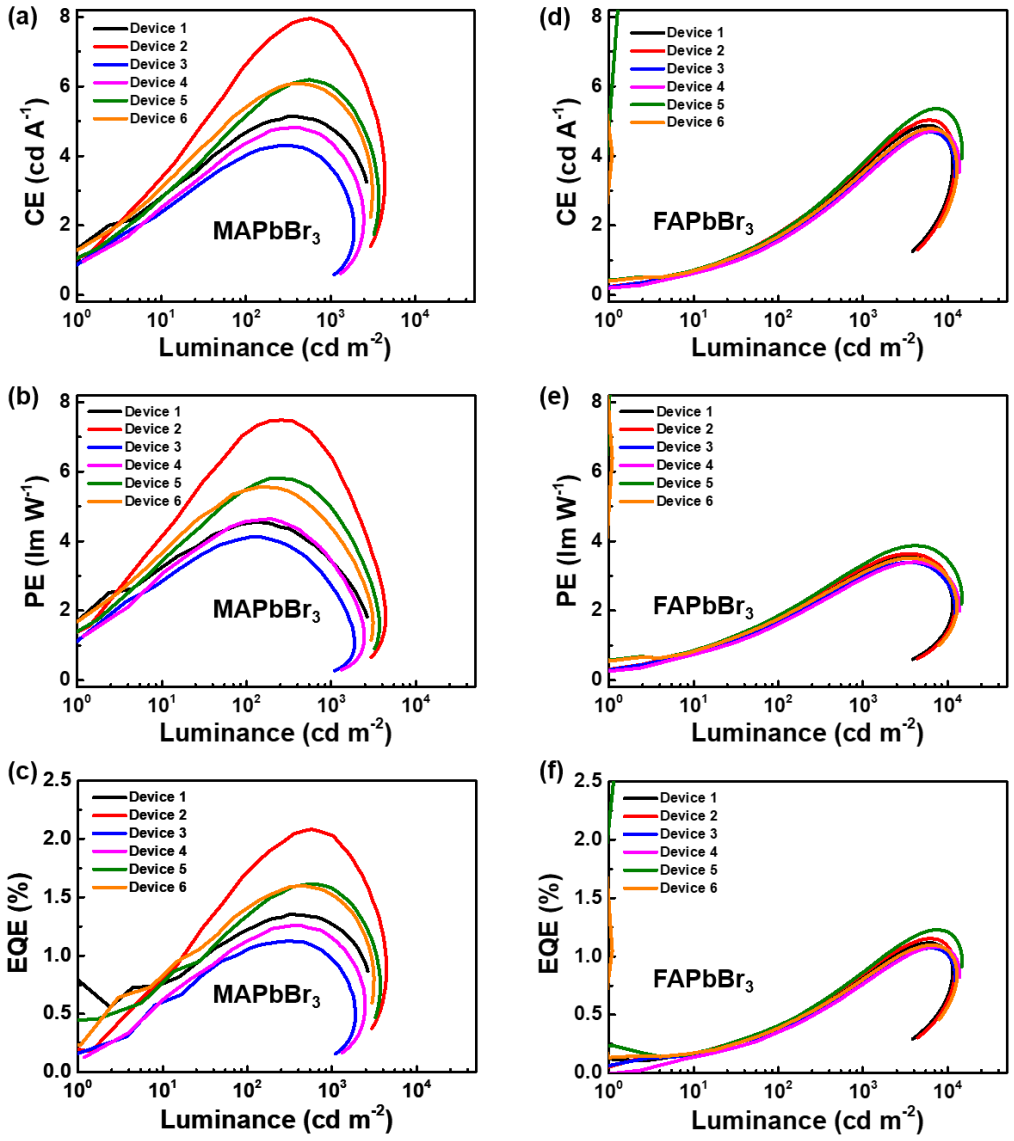


**Figure 6.5** (a-c) CE, PE, and EQE versus luminance for $MAPbBr_3$-based LEDs, (d-f) CE, PE, and EQE versus luminance for $FAPbBr_3$-based LEDs.

An additional advantage of employing $FAPbBr_3$-based LEDs over $MAPbBr_3$-based diodes, is that the highest device efficiencies are attained at higher luminance. The current efficiency (CE) and power efficiency (PE), and thereby

the overall external quantum efficiency (EQE), was achieved at luminance > 5,000 cd $m^{-2}$ for $FAPbBr_3$-based LEDs, whereas it was < 1000 cd $m^{-2}$ for $MAPbBr_3$-based LEDs (Figure 6.5). Hence, $FAPbBr_3$ is favorable for lighting applications which require a brightness ≥ 2000 cd $m^{-2}$.[17] However, for display applications, where a luminance of 200 cd $m^{-2}$ is sufficient, $MAPbBr_3$-based LEDs can operate at higher efficiencies compared to $FAPbBr_3$-based LEDs.

To summarize, despite the higher efficiencies achieved with $MAPbBr_3$, $FAPbBr_3$ showed more favorable attributes such as higher thermal stability and higher luminance. The drawback for $FAPbBr_3$ was the higher current densities required to achieve turn-on condition in the $FAPbBr_3$-based LEDs compared to the $MAPbBr_3$-based LEDs. Since the same device stack was used for both $MAPbBr_3$ and $FAPbBr_3$, the injection problem is most likely due to the $FAPbBr_3$ NCs and not the transport layers. Hence, attempts were made to optimize the synthesis of $FAPbBr_3$ NCs, mainly by varying the ligand (*n*-octylamine) concentration used in the synthesis.

### 6.3.3 Optimization of $FAPbBr_3$ NC synthesis

* This was a collaborative project wherein my contribution was the steady-state optical characterization.

Herein, the ratio of *n*-octylamine (OA) to $PbBr_2$ was varied as 3:1, 4:1, 5:1, 7:1, and 10:1 during synthesis, as described in Protocol 2 (see section 6.2.2). Steady-state absorption spectroscopy of the NC films reveal an absorption peak around 427 to 432 nm (band gap ≈ 2.9 eV) attributed to the quasi-2D phases,[18] for all the OA:$PbBr_2$ ratios (Figure 6.6-a). The quasi-2D phase refers to the layered perovskite phase, $(OA)_2(FA)_{n-1}Pb_nBr_{3n+1}$ with $n$ = 2, 3, 4, etc. denoting the number of $Pb^{2+}Br_6^-$ layers sandwiched between two octylammonium bromide layers.[19] The excitonic absorption peak wavelength at approx. ~430 nm corresponds well with the $n$=2 quasi-2D phase.[20-22] At increased ligand-to-precursor ratios, the intensity of the corresponding quasi-2D phase excitonic

absorption peak also increased, with a concurrent decrease in the intensity at the absorbance edge originating from the 3D $FAPbBr_3$ NC phase at the 537-538 nm (band gap ≈ 2.3 eV).This signifies increase in the quasi-2D phases with increase in OA:$PbBr_2$ ratio.

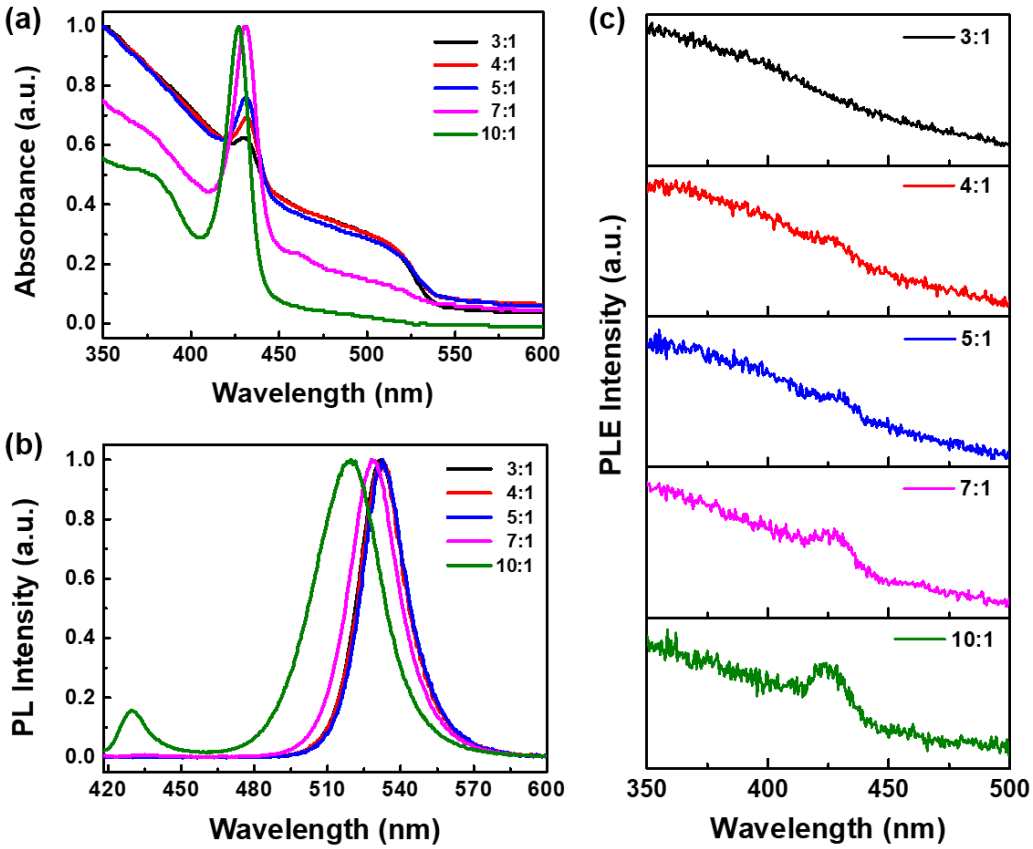


**Figure 6.6** (a) Absorbance, (b) PL, and (c) PLE spectra of spin-coated $FAPbBr_3$ NC thin films synthesized using OA:$PbBr_2$ ratios of 3:1 (black), 4:1 (red), 5:1 (blue), 7:1 (magenta), and 10:1 (olive).

The PL emission from the NC films with the different OA:$PbBr_2$ ratios exhibited maxima around 532 - 519 nm, all within the green-light emitting regime evidencing that that the emission is predominantly from the 3D phase (Figure 6.6-b). However, the wavelength shift of the PL maximum from 532 nm for the 3:1, 4:1 and 5:1 ratio samples to 528 nm and 519 nm for the 7:1, and 10:1 ratio, respectively, as well as the clear additional peak at ~430 nm for the 10:1, signified

the larger contribution from the quasi-2D phases at higher OA:$PbBr_2$ ratios. In fact, for all OA:$PbBr_2$ ratios except 3:1, there was a contribution from the quasi-2D phase on the PL emission wavelength corresponding to the 3D phase as indicated from the photoluminescence excitation (PLE) spectroscopic measurements. The PLE spectra at the maximum PL emission wavelength, showed a peak at ~430 nm for all ratios except 3:1(Figure 6.6-c). This suggests the electron funneling from the larger band gap quasi-2D phase to the lower band gap 3D phase, which could be useful for improving the charge injection to the 3D phase for LED application.

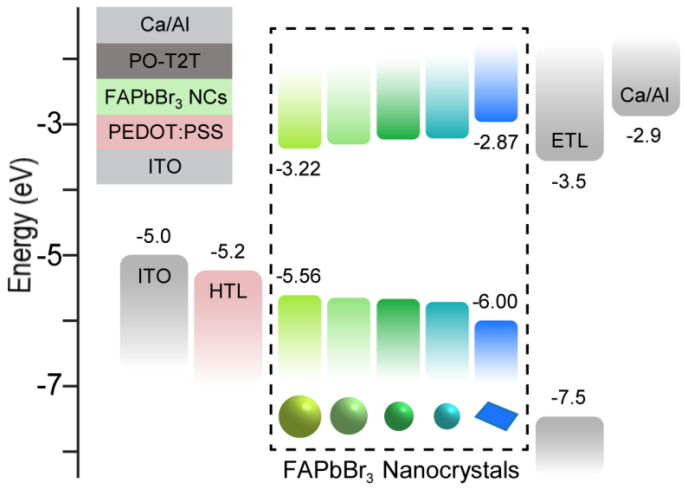


**Figure 6.7** Schematic diagram of the flat band energy levels of the LED device stack. Proposed energy funneling from quasi-2D nanoplatelet to 3D NCs depicted within the dashed rectangle.

Moreover, the size distribution of the NCs is expected to facilitate the energy transfer from the quasi-2D phase to the smallest NCs within the size distribution. This is followed progressively by funneling to the population of larger NCs of narrower band gap, thereby creating an energy cascade (Figure 6.7). The funneling can help achieve high luminance at low excitation powers intensities, as the excited states can be concentrated at the lower bandgap regions.[23] Consequently, LEDs prepared from these NC inks (particularly the 4:1 and 5:1

ratios) turn-on at significantly lower current densities (and voltages) compared to the $FAPbBr_3$-based LEDs reported in Section 6.3.2. Furthermore, record device efficiencies of above 13% EQE and intense luminance exceeding 50,000 cd $m^{-2}$ were obtained (Figure 6.8).

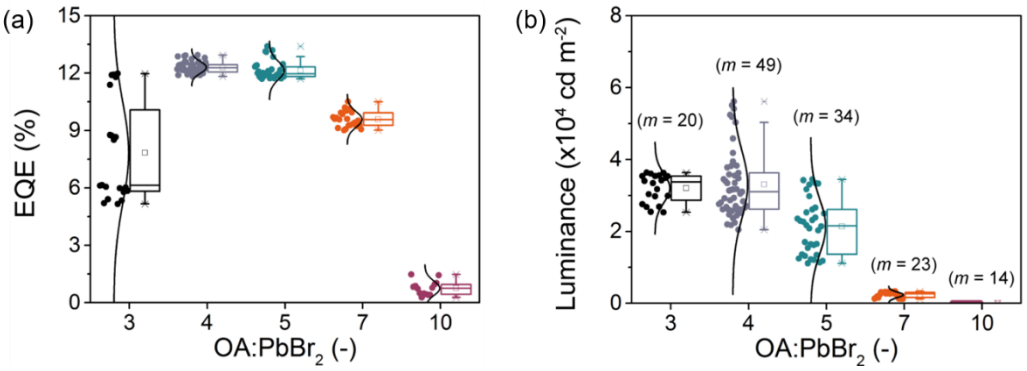


**Figure 6.8** Luminance, EQE, current efficiency, power efficiency values shown as box plots for LED devices (m is number of devices measured) based on different $OA:PbBr_2$ ratios. Each measured device is represented by filled circles with a normal distribution. The squares and crosses represent the median values and outliers, whereas the error bars represent the minimum and maximum values. Lower and upper bars within the box, represent the first and third quartile (Q1 and Q3), respectively.

To investigate whether energy cascading and efficiency improvements similar to $FAPbBr_3$ NCs, can be achieved with $MAPbBr_3$ NC-based LEDs, inks were synthesized according to the protocol optimized for $FAPbBr_3$.

### 6.3.4 Replacement of MA with FA in the protocol for $FAPbBr_3$ NC synthesis

Herein, the $MAPbBr_3$ NCs were synthesized by using a 1.15:1 ratio of precursors ($CH_3NH_3Br:PbBr_2$), $OA:PbBr_2$ ratio of 5:1, and all other synthesis parameters as per Protocol 2. Additionally, $MAPbBr_3$ NCs were also synthesized with 2:1 ratio of $CH_3NH_3Br:PbBr_2$ for the sake of exact comparison with the $FAPbBr_3$ NC synthesis in Protocol 2.

Similar to the $FAPbBr_3$ synthesis, a quasi-2D phase, presumably, $(OA)_2(MA)_{n-1}Pb_nBr_{3n+1}$ ($n$=2), was formed during the $MAPbBr_3$ synthesis, with an excitonic absorption peak at ~430 nm (Figure 6.9-a).[20-22] The quasi-2D peak was more discernible for the $MAPbBr_3$ NC prepared from the 1.15:1 than the 2:1 precursor ratio; the latter, which could hardly be detected. The overall absorbance, however, was extremely low for the 2:1 ratio. The low intensity of the absorption curve for 2:1 ratio could be indicative of the reduction of the total number of NCs in the film, and hence low NC ink concentration (as all the inks were spin coated under same conditions). As mentioned in Chapter 4, this could be because the excess $CH_3NH_3Br$ precursor molecules can compete with the ligands to passivate the NC surface, thereby effectively reducing the surface binding sites occupied by ligands.[24] Hence, colloidal stability and therefore NC ink concentration is diminished. Hence, only the 1.15:1 precursor ratio, which gave higher absorbance, was used for further structural and device studies.

The steady-state PL spectra for both $FAPbBr_3$ and $MAPbBr_3$ NCs are similar to ones prepared by Protocol 1, with a maximum PL intensity at 531 and 524 nm respectively (Figure 6.9-b), indicating emission from the 3D phase only. However, no peaks close to ~430 nm, were detected in the PLE spectra of the $MAPbBr_3$ NCs. This could indicate either that the funneling was not significant enough to be detected in steady-state measurements, or that a gradient band gap reduction required to facilitate the energy transfer; was not formed between the quasi-2D phase and the 3D $MAPbBr_3$ NCs.

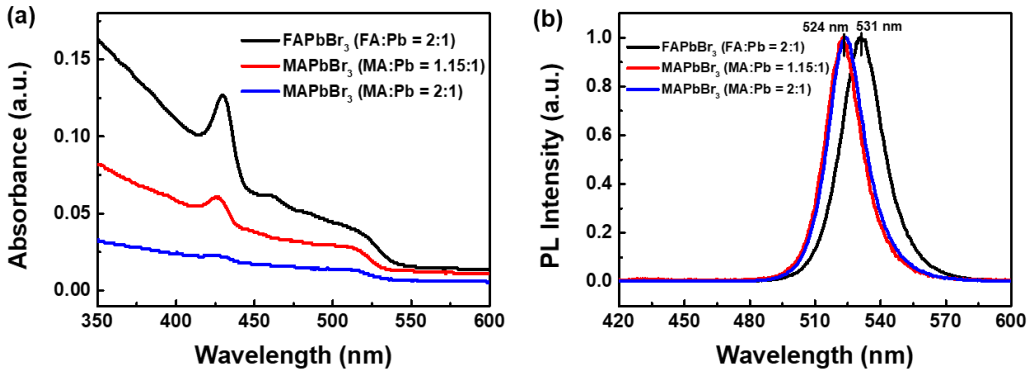


**Figure 6.9** (a) Absorbance and (b) PL spectra of spin-coated thin films of $FAPbBr_3$ NC (FA:Pb = 2:1, black), $MAPbBr_3$ NC (MA:Pb = 1.15:1, red), and $MAPbBr_3$ NC (MA:Pb = 2:1, blue) inks, respectively, synthesized using OA:$PbBr_2$ ratio of 5:1 (Protocol 2)

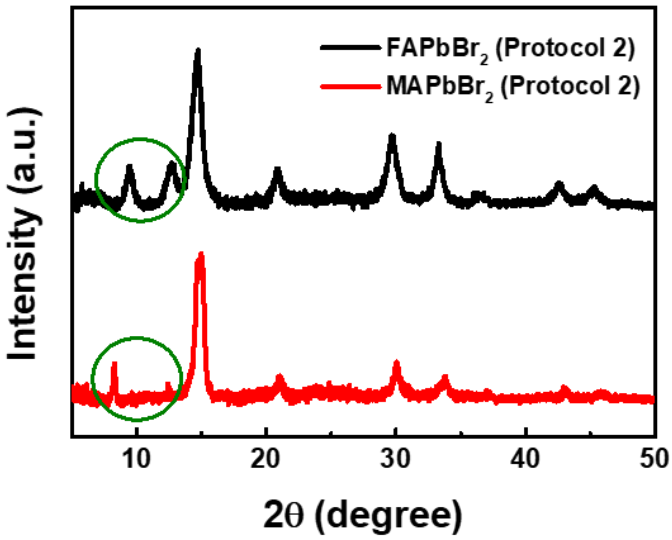


**Figure 6.10** XRD patterns of thin films of $FAPbBr_3$ NC (black), $MAPbBr_3$ NC (red) synthesized using OA:$PbBr_2$ ratio of 5:1 (Protocol 2).

The formation of the quasi-2D phase was further confirmed by XRD, where additional peaks at $2\theta = 8.28°$ and 12.42° in the $MAPbBr_3$ diffraction pattern and $2\theta = 9.46°$ and 12.72° in the $FAPbBr_3$ NC diffraction pattern are lower than $2\theta$ the values observed for their respective 3D cubic perovskite phases (Figure 6.10).

Subsequently, LEDs were fabricated from both the $MAPbBr_3$ and $FAPbBr_3$ NC inks employing the same device stack used with NC inks synthesized by Protocol 1, specifically, ITO/PEDOT:PSS/perovskite layer/PO-T2T/Ca/Al. The current density-voltage (J-V) characteristics of the $MAPbBr_3$ devices exhibited higher leakage current than the $FAPbBr_3$ devices (Figure 6.11-a), indicating poor charge injection in the $MAPbBr_3$-based LEDs. This is further confirmed by the higher turn-on voltage of 2.7 V for the $MAPbBr_3$-based LEDs which is 0.4 V higher than the band gap of ~2.3 eV. In contrast, the $FAPbBr_3$-based LEDs displayed turn-on voltages of 2.3 V. Moreover, the $FAPbBr_3$-based LEDs showed luminance > 7500 cd $m^{-2}$ and current efficiency of ~34 cd $A^{-1}$ compared to ~40 cd $m^{-2}$ luminance and close to 1.5 cd $A^{-1}$ current efficiency in $MAPbBr_3$-based LEDs (Figure 6.11-d). Thus, while the 2D phase formation was improved the performance of $FAPbBr_3$-based LEDs, it seems to have a detrimental effect on the $MAPbBr_3$-based LEDs.

For both $MAPbBr_3$ and $FAPbBr_3$, the EL emission peaks (Figure 6.11-b) coincide well with PL emission peaks (Figure 6.9-b), confirming that luminance is only originating from the 3D phase. Hence, the electrons injected into the quasi-2D phase would either funnel to the 3D phase or recombine non-radiatively. The $FAPbBr_3$-based LEDs displayed considerably lower current density at the turn-on voltage for the NCs prepared by synthesis Protocol 2 (~0.03 mA $cm^{-2}$) than Protocol 1 (~0.5 mA $cm^{-2}$), as expected from energy funneling from 2D to 3D (Figure 6.11-c, Figure 6.4-c,d). However, for the $MAPbBr_3$-based LEDs similar current densities at turn-on were obtained for NCs prepared by Protocol 1 (~0.1 mA $cm^{-2}$) and 2 (~0.12 mA $cm^{-2}$) and, respectively. So, the quasi-2D phase in the $MAPbBr_3$ case, likely result in non-radiative recombination only. In addition, both funneling (due to concentration of charges) and non-radiative recombination would increase self-heating during device operation. This is demonstrated by the luminance drop-off at lower current densities, ~10 mA $cm^{-2}$ for $MAPbBr_3$-based

LEDs and ~50 mA $cm^{-2}$ for $FAPbBr_3$-based LEDs for Protocol 2 compared to that at ~100 mA $cm^{-2}$ and ~300 mA $cm^{-2}$, respectively for Protocol 1.

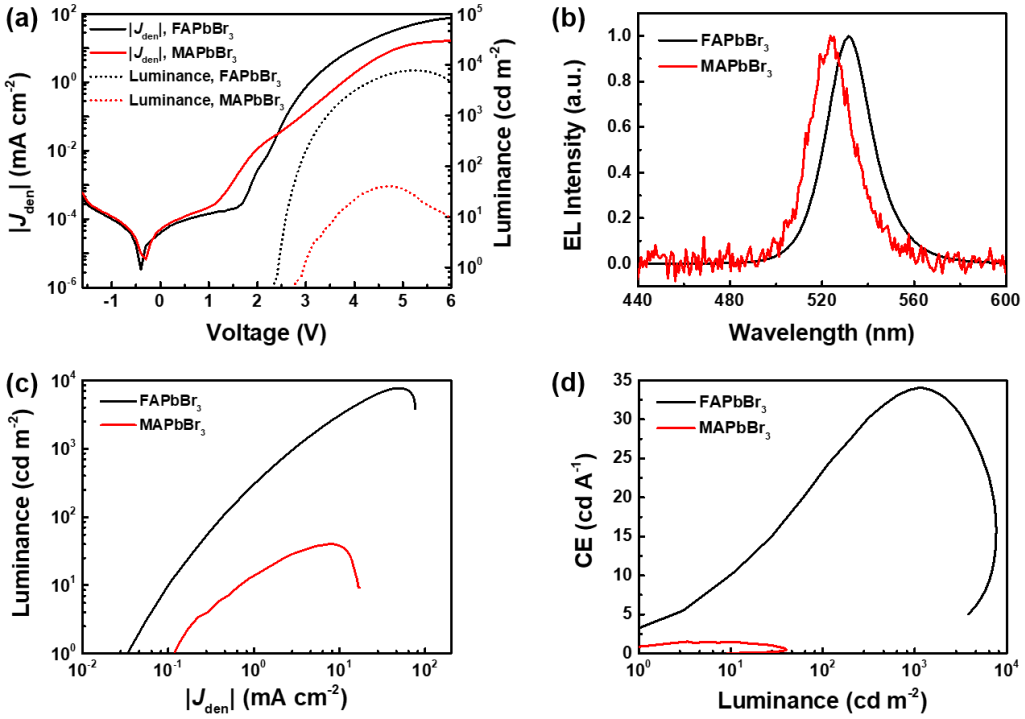


**Figure 6.11** LED Characterization: (a) Current density -voltage-luminance (J-V-L) curves, (b) EL spectra, (c) luminance versus current density, and (d) current efficiency (CE) versus luminance of $FAPbBr_3$-based LED (black) compared to $MAPbBr_3$-based LED (red) when NC synthesis protocol 2 was used.

Overall, the $FAPbBr_3$ NCs demonstrated higher radiative luminance and higher thermal stability compared to the $MAPbBr_3$ NCs, irrespective of the synthetic protocol However, optimization of the ligand to precursor ratio was crucial for attaining device turn-on at low voltages and low current densities for $FAPbBr_3$ NC-based LEDs. Moreover, the optimization for $FAPbBr_3$ NCs was unfavorable for $MAPbBr_3$ NCs; the $MAPbBr_3$ NC-based LED based on synthesis Protocol 1 outperformed the one based on synthesis Protocol 2 for all device metrics – higher luminance, lower turn-on voltage, and current density, higher device efficiencies. Hence, the critical role of material-specific NC synthesis

optimization in achieving good device performance is established unequivocally.

## 6.4 Conclusion

In conclusion, two synthesis protocols were used to prepare $MAPbBr_3$ and $FAPbBr_3$ NCs and their steady-state optical properties, crystal structures, and LED performances were analyzed. The intrinsic optical properties of the NCs, e.g. optical band gap, were not significantly affected, by the changes in synthesis protocols. However, the excess ligands used in synthesis Protocol 2 resulted in the formation of quasi-2D nanoplatelets, as evidenced by the XRD diffraction peaks at low 2θ angles and excitonic absorption peaks at ~430 nm. In case of $FAPbBr_3$, energy transfer from the quasi-2D phase to the 3D phase (funneling) was detected. This improved the performance of $FAPbBr_3$-based LEDs tremendously, with current efficiencies increasing from 5 cd $A^{-1}$ (Protocol 1) to 34 cd $A^{-1}$ (Protocol 2; ca. 7 times enhancement). In case of $MAPbBr_3$-based LEDs no funneling was detected. In fact, the LED performance diminished in terms of both luminance and efficiency when NCs were prepared via synthesis Protocol 2. This indicates that while ligand optimization plays a crucial role in the LED device operation, the optimization needs to be material specific. Moreover, $FAPbBr_3$ NCs displayed superior LED performances in terms of brightness, efficiency and thermal stability compared to $MAPbBr_3$ NCs. Hence, $FAPbBr_3$ NCs present a more robust and promising hybrid inorganic-organic hybrid perovskite system for LED applications.

## 6.5 References

1 Goldschmidt, V. M. Die Gesetze der Krystallochemie. *Naturwissenschaften* **14**, 477-485, doi:10.1007/bf01507527 (1926).

2 Kieslich, G., Sun, S. & Cheetham, A. K. Solid-state principles applied to organic-inorganic perovskites: new tricks for an old dog. *Chemical Science* **5**, 4712-4715, doi:10.1039/C4SC02211D (2014).

3 Green, M. A. *et al.* Solar cell efficiency tables (version 50). *Progress in Photovoltaics: Research and Applications* **25**, 668-676, doi:10.1002/pip.2909 (2017).

4 Grätzel, M. The Rise of Highly Efficient and Stable Perovskite Solar Cells. *Accounts of Chemical Research* **50**, 487-491, doi:10.1021/acs.accounts.6b00492 (2017).

5 Syzgantseva, O. A., Saliba, M., Grätzel, M. & Rothlisberger, U. Stabilization of the Perovskite Phase of Formamidinium Lead Triiodide by Methylammonium, Cs, and/or Rb Doping. *The Journal of Physical Chemistry Letters* **8**, 1191-1196, doi:10.1021/acs.jpclett.6b03014 (2017).

6 Tan, Z.-K. *et al.* Bright light-emitting diodes based on organometal halide perovskite. *Nature Nanotechnology* **9**, 687-692, doi:10.1038/nnano.2014.149 (2014).

7 Cho, H. *et al.* Overcoming the electroluminescence efficiency limitations of perovskite light-emitting diodes. *Science* **350**, 1222-1225, doi:10.1126/science.aad1818 (2015).

8 Huang, H. *et al.* Emulsion Synthesis of Size-Tunable $CH_3NH_3PbBr_3$ Quantum Dots: An Alternative Route toward Efficient Light-Emitting Diodes. *ACS Applied Materials & Interfaces* **7**, 28128-28133, doi:10.1021/acsami.5b10373 (2015).

9 Li, G. *et al.* Efficient Light-Emitting Diodes Based on Nanocrystalline Perovskite in a Dielectric Polymer Matrix. *Nano Letters* **15**, 2640-2644, doi:10.1021/acs.nanolett.5b00235 (2015).

10 Li, J., Bade, S. G. R., Shan, X. & Yu, Z. Single-Layer Light-Emitting Diodes Using Organometal Halide Perovskite/Poly(ethylene oxide) Composite Thin Films. *Advanced Materials* **27**, 5196-5202, doi:10.1002/adma.201502490 (2015).

11 Meng, L. *et al.* Pure Formamidinium-Based Perovskite Light-Emitting Diodes with High Efficiency and Low Driving Voltage. *Advanced Materials* **29**, 1603826-n/a, doi:10.1002/adma.201603826 (2017).

12 Perumal, A. *et al.* High brightness formamidinium lead bromide perovskite nanocrystal light emitting devices. *Scientific Reports* **6**, 36733, doi:10.1038/srep36733 (2016).

13 Eperon, G. E. *et al.* Formamidinium lead trihalide: a broadly tunable perovskite for efficient planar heterojunction solar cells. *Energy & Environmental Science* **7**, 982-988, doi:10.1039/C3EE43822H (2014).

14 Hanusch, F. C. *et al.* Efficient Planar Heterojunction Perovskite Solar Cells Based on Formamidinium Lead Bromide. *The Journal of Physical Chemistry Letters* **5**, 2791-2795, doi:10.1021/jz501237m (2014).

15 Arora, N. *et al.* Intrinsic and Extrinsic Stability of Formamidinium Lead Bromide Perovskite Solar Cells Yielding High Photovoltage. *Nano Letters* **16**, 7155-7162, doi:10.1021/acs.nanolett.6b03455 (2016).

16 Zhumekenov, A. A. *et al.* Formamidinium Lead Halide Perovskite Crystals with Unprecedented Long Carrier Dynamics and Diffusion Length. *ACS Energy Letters* **1**, 32-37, doi:10.1021/acsenergylett.6b00002 (2016).

17 Gaspar, D. J. & Polikarpov, E. *OLED fundamentals: materials, devices, and processing of organic light-emitting diodes*. (CRC Press, 2015).

18 Byun, J. *et al.* Efficient Visible Quasi-2D Perovskite Light-Emitting Diodes. *Advanced Materials* **28**, 7515-7520, doi:10.1002/adma.201601369 (2016).

19 Kenichiro, T. & Takashi, K. Bandgap and exciton binding energies in lead-iodide-based natural quantum-well crystals. *Science and Technology of Advanced Materials* **4**, 599 (2003).

20 Tabuchi, Y., Asai, K., Rikukawa, M., Sanui, K. & Ishigure, K. Preparation and characterization of natural lower dimensional layered

perovskite-type compounds. *Journal of Physics and Chemistry of Solids* **61**, 837-845, doi:10.1016/S0022-3697(99)00402-3 (2000).

21 Takeoka, Y., Asai, K., Rikukawa, M. & Sanui, K. Systematic Studies on Chain Lengths, Halide Species, and Well Thicknesses for Lead Halide Layered Perovskite Thin Films. *Bulletin of the Chemical Society of Japan* **79**, 1607-1613, doi:10.1246/bcsj.79.1607 (2006).

22 Calabrese, J. *et al.* Preparation and Characterization of Layered Lead Halide Compounds. *Journal of the American Chemical Society* **113**, 2328-2330, doi:DOI 10.1021/ja00006a076 (1991).

23 Quan, L. N. *et al.* Tailoring the Energy Landscape in Quasi-2D Halide Perovskites Enables Efficient Green-Light Emission. *Nano Letters* **17**, 3701-3709, doi:10.1021/acs.nanolett.7b00976 (2017).

24 Wang, L. *et al.* Scalable Ligand-Mediated Transport Synthesis of Organic-Inorganic Hybrid Perovskite Nanocrystals with Resolved Electronic Structure and Ultrafast Dynamics. *ACS Nano* **11**, 2689-2696, doi:10.1021/acsnano.6b07574 (2017).

# Chapter 7

# Conclusion & Research Outlook

*This Chapter summarizes the strategies explored in this project to optimize the colloidal organic-inorganic hybrid perovskite nanocrystals synthesis for light emitting diode (LED) applications, and the scientific insights gained therein. Some suggestions for further advancement of the perovskite LED field, including some preliminary studies in that respect, are also discussed.*

## 7.1 Summary and discussion

Highly luminescent organic-inorganic hybrid perovskite nanocrystals (NCs) can be efficiently prepared by colloidal synthesis methods, such as ligand assisted re-precipitation (LARP) and hot-injection methods. Herein, the NCs are precipitated from precursor solution by using solubility difference at high temperatures, or by use of anti-solvents, or both. However, the efficiencies of light emitting diodes (LEDs) based on NC inks prepared from the colloidal methods are still lagging behind those attained from direct thin film crystallization of the perovskite layer from precursor solutions, possibly due to inefficient charge transfer and non-uniformity of NC films. In this thesis, different reaction variables in the colloidal NC synthesis were varied to identify factors critical for improving the device performances. The main observations and interpretations are as follows:

- From the precursor molar ratio, $CH_3NH_3Br$:$PbBr_2$, variation study conducted in Chapter 4, it was found that slight excess of $CH_3NH_3Br$ (1.05:1 ratio) could enhance the photoluminescence (PL) intensity of $CH_3NH_3PbBr_3$ NC inks. However, higher ratios of $CH_3NH_3Br$:$PbBr_2$ deteriorates the colloidal stability and results in NC inks of poor quality (low NC concentration and low colloidal stability for 1.25:1 ratio). When excess of $CH_3NH_3^+$ cations are present during NC formation, they can compete with the long carbon chain ammonium cations from the ligands, to bind with the surface bromide ions on the NCs. The $CH_3NH_3^+$ ions are also capable of passivating the NC surface. In absence of steric barriers provided by the long carbon chains, however, the NCs are prone to aggregate, thereby reducing the colloidal stability of the NC ink. Since large crystals or aggregates generally exhibit lower luminance compared to NCs, the aggregates can conveniently be removed during NC purification, while the supernatant containing the dispersed NCs are used for device fabrication.

- The stability of the NC inks constitutes an intricate problem for LED fabrication. Highly stable inks (days and months) may, in fact, not be ideal for device fabrication applications, as high ligand concentrations (i.e. high steric shielding) are required to obtain such stability. These would be detrimental for charge injection, critical for electroluminescent applications, due to their insulating nature. Instead, NC inks are required in which the NC ligand capping is just sufficient to stabilize the solution until spin coating of the thin films. The inks used in the project start to precipitate within a day. Though counterintuitive, the low stability inks display the best performance.

- Besides the ink stability, the ink concentration is another important factor during LED fabrication. In dilute NC inks, the NCs can be separated enough to prevent aggregation at lower ligand concentration. These dilute inks, however, would produce films of poor surface coverage resulting in shunting of the diodes. In more concentrated inks, the number of interparticle interactions increase, decreasing the ink stability. Indeed, the most successful inks have NC concentrations in between these two extremes, such that precipitation does not occur prior to film formation, and full surface coverage is obtained. Moreover, the solvent used for dispersing the NCs also plays a key role. Generally, non-polar solvents with low vapor pressure and boiling point are preferred so that the NC inks can be uniformly coated on the substrate after which the solvent can be easily removed, e.g. solvents like toluene, heptane, octane. Solvents like hexane or chloroform, which have high vapor pressure, can be detrimental for film formation as the NCs tend to aggregate during/before film deposition due to the high solvent evaporation rate.

- Another significant observation was that the surface coverage and recombination kinetics are more important than the PL intensity for achieving high electroluminescence (EL) intensity. As discussed in Chapter 4, the

1.05:1 precursor ratio attained highest PL intensity. But, the highest contribution of the bimolecular recombination in the PL decay lifetimes and the highest NC density upon spin coating of the NC inks were achieved for the 1.15:1 ratio. Consequently, the highest EL and external quantum efficiency (EQE) was achieved for the 1.15:1 ratio compared to all other investigated precursor ratios.

- The surface coverage and recombination kinetics were further analyzed in Chapter 5 by preparing NC inks exhibiting different types of size distributions. Smooth NC films (root mean square roughness ~4 nm) and short PL decay times (tens of ns) were found to be beneficial for improving the operational stability of the LED device. Furthermore, NC inks in which energy funneling from the small NCs to large NCs was detected from TRPL studies, showed lower device stability compared to the inks in which funneling was less likely.

- Finally, in Chapter 6, I tried to extend the optimized protocol for $CH_3NH_3PbBr_3$ ($MAPbBr_3$) NC synthesis to form $CH(NH_2)_2PbBr_3$ ($FAPbBr_3$) NCs. However, devices based on $FAPbBr_3$ NCs from this protocol exhibited poor charge injection – high current densities were required to attain a luminance of 1 cd $m^{-2}$ (i.e. turn-on of LED), compared to the $MAPbBr_3$-based devices. Subsequently, a synthesis protocol optimized for $FAPbBr_3$ NCs, which demonstrated very good LED device performance (EQE ~13%) was applied to $MAPbBr_3$ NC synthesis. Here, funneling from quasi 2D to 3D NCs improved the charge injection for $FAPbBr_3$, but this approach resulted in $MAPbBr_3$-based devices with poor charge injection. Hence, the NC synthesis optimization for enhancing the LED performance needs to be material specific.

## 7.2 Strategies for Future work

### 7.2.1 Varying the ligands used for capping the NCs

The role of ligands in controlling the shape and size of the NCs, providing surface passivation for the NCs, and maintaining the colloidal stability is well-documented.[1-8] Typically, a combination of long chained aliphatic amines and carboxylic acids, for e.g., oleylamine and oleic acid, is used for colloidal synthesis of perovskite NCs. By varying the chain length of the amine or acid or both, various NC shapes and sizes were achieved,[2] while using branched-chain amines the colloidal stability could significantly be improved.[7] However, since these ligands are generally insulating in nature, controlling the ligand density control on the NC surface by purification cycles is critical for achieving high electroluminescence from these NCs.[9] Another possible strategy is to use shorter carbon chain ligands and whereby the colloidal stability may decrease but the electrical injection could improve. For example, octylamine (C8) has been reported as a suitable ligand which helps attain good PL and EL intensities,[10] and has been used as the capping ligand in the work reported in the previous chapters.

It was hypothesized that investigating ligands of different chain lengths could be a promising method to improve the perovskite LED device performance. Accordingly, the influence of several ligands – butylamine (C4), hexylamine (C6), octylamine (C8), dodecylamine (C12), and oleylamine (C18) – on the PL and EL of $CH_3NH_3PbBr_3$ NCs were compared. The NCs were synthesized as per the protocol described in Chapter 4, using a 1.15:1 molar ratio of $CH_3NH_3Br$: $PbBr_2$, with 0.075 mmol each of $PbBr_2$, and aliphatic amine, and 500 µL oleic acid.

Steady-state PL measurements (Figure 7.1-a) revealed that the PL emission peak and FWHM remained unchanged for butylamine, hexylamine, and octylamine.

However, the butylamine-capped NCs displayed poor ink stability and hence was excluded from further studies. The longer carbon chain ligands likely provide better spatial separation between NCs than the shorter carbon chain ligands, leading to more prominent quantum confinement effects. Accordingly, the blue-shift in the main PL peak position for dodecylamine and oleylamine correlates well with previous reports of perovskite nanoplatelets (2D and quasi-2D phases).[11,12] Interestingly, the maximum PL intensity position is more blue shifted when dodecylamine (C12) was used (~509 nm) compared to oleylamine (C18, ~515 nm). This is the possibly due to different ligand binding mechanism for the conjugated oleylamine compared to the aliphatic dodecylamine.

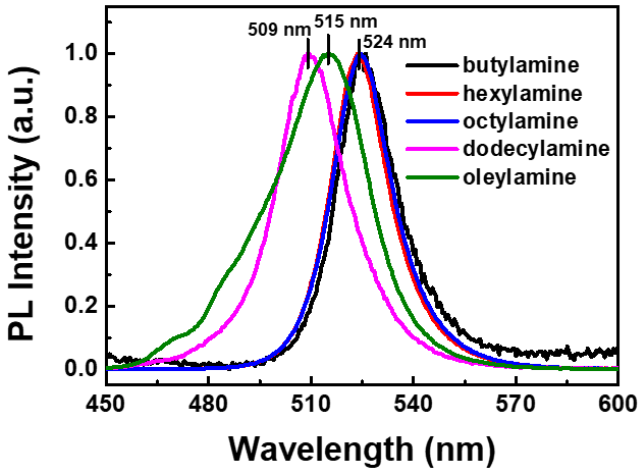


**Figure 7.1** Normalized PL spectra of $CH_3NH_3PbBr_3$ NCs when different capping ligands, butylamine (black), hexylamine (red), octylamine (blue), dodecylamine (magenta) and oleylamine (olive) are employed.

The J-V-L curves for the LEDs fabricated from the $CH_3NH_3PbBr_3$ NCs capped with hexylamine, octylamine, dodecylamine and oleylamine are depicted in Figure 7.2. The oleylamine capping resulted in very poor (almost negligible) luminance. This can be attributed to the resistive nature of oleylamine as evidenced by the high turn-on voltage and overall low current flowing through the device. The highest luminance was attained when octylamine was used, followed by hexylamine and dodecylamine. The same trend was observed in the

current efficiency curves of the LEDs (Figure 7.3). The performance improvement desired from the shorter hexylamine ligand compared to octylamine, was not achieved, however, the similar (low) turn-voltages in the two cases makes hexylamine is a promising candidate for further studies.

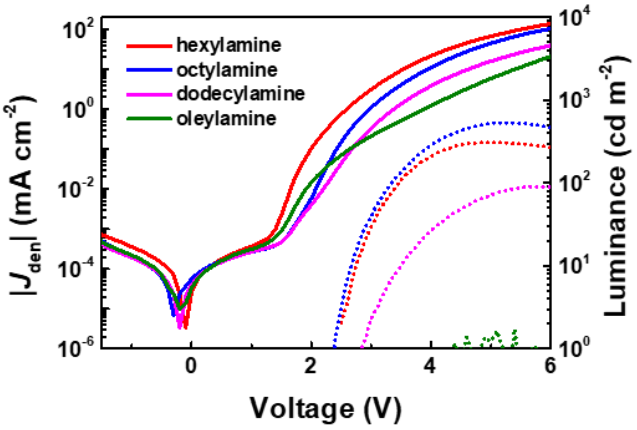


**Figure 7.2** J-V-L curves of LEDs fabricated from $CH_3NH_3PbBr_3$ NCs capped with hexylamine (red), octylamine (blue), dodecylamine (magenta) and oleylamine (olive).

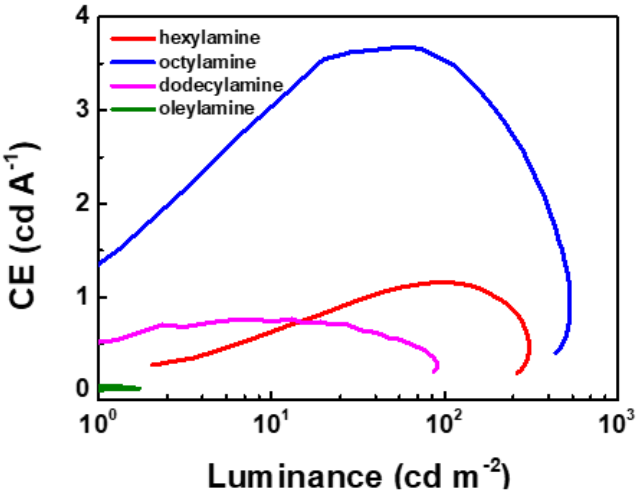


**Figure 7.3** Current efficiency (CE) versus luminance of LEDs fabricated from $CH_3NH_3PbBr_3$ NCs capped with hexylamine (red), octylamine (blue), dodecylamine (magenta) and oleylamine (olive).

In conclusion, both the PL and EL characterization of the hexylamine-capped

$CH_3NH_3PbBr_3$ NCs show promising results such as (1) single PL peak emission with narrow FWHM similar to that obtained with octylamine capped NCs and (2) turn-on voltage similar to the octylamine case, albeit at lower luminance. Hence, it shows some promise for improved device performance with optimization of the ligand amounts and synthesis conditions. For further improvements, we should probably look away from the conventional aliphatic ligands, to branched ligands, particularly entropic ligands, which are reported to be promising for chalcogenide quantum dots.[13,14] These ligands which have large high intramolecular entropy, reduce interdigitation between ligands and increase the solubility of the ligands. Moreover, the branched ligands show better electrical injection compared to its aliphatic counterparts. Thus, both chemical processing involved in the device fabrication may be simplified along with improvements in LED performance.

### 7.2.2 Modifications in the charge transport layers

Good band alignment of the charge transport layers with the active (absorption or emitter) layer is crucial for efficient performance of any optoelectronic device – for efficient charge extraction in case of photovoltaic devices and efficient charge injection in case of light emitting devices.[15,16] For LEDs, this means that the electron transport layer (ETL) should have a minimal energy barrier with the conduction band minimum (CBM) of the emitter layer as well as a good hole blocking ability (high barrier between valence band minimum (VBM) of emitter and VBM of the ETL). Similarly, the hole transport layer (HTL) should have minimal energy barrier with the VBM of the emitter and high barrier between CBM of emitter and CBM of HTL. Moreover, the charge injection needs to be balanced to optimize the radiative recombination; so, the charge carrier mobility and carrier concentration in the transport layers should be of the same order[16,17] (Figure 7.4). In addition, due to the inherent instability of perovskites in humid environments, transport layers which would protect the perovskite layer from

exposure to humid environments would be beneficial. In that respect, inorganic transport layers have significant advantage over organic transport layers.[18-20] Also, for long-term stability of the device, the chemical and thermal stability of the individual layers and the interfaces are critical.

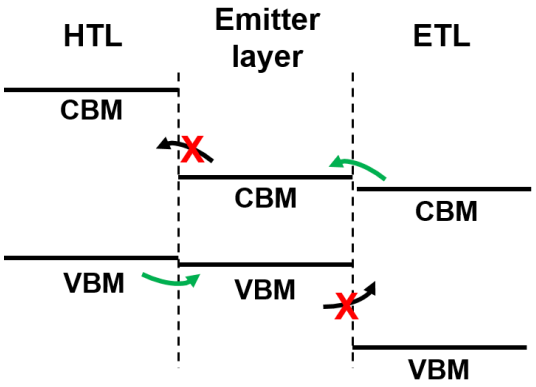


**Figure 7.4** Band alignment schematic for transport layers and emitter layer in LED.

In this thesis, the focus was on the emitter layer, hence, organic charge transport layers, commonly used for organic LEDs and perovskite LEDs, were employed for device fabrication. While they provided good carrier injection to the perovskite emitter layer (as evidenced by the low turn-on voltages in the devices), the organic transport layers can be detrimental for device stability. For instance, poly(3,4-ethylenedioxythiophene)-poly(styrenesulfonate) (PEDOT:PSS) was used as the HTL for all the fabricated LEDs. However, due to the acidic nature of PSS, the indium tin oxide (ITO) anode can be etched and indium containing species can diffuse into the PEDOT:PSS layer.[21] This process occurs even under $N_2$ atmosphere, and is accelerated at higher temperatures and when exposed to air.[21,22] Similarly, there are reports of diffusion of metal atoms into the organic transport layers (and chemical reactions with the organic molecules) during thermal evaporation of the top electrodes.[23,24]

In contrast, use of inorganic transport layers have shown significant improvements in device stability. For example, Shi et al. employed Mg-doped

inorganic transport layers such as MgZnO and MgNiO with energy levels that are well-aligned with the $CsPbBr_3$ quantum dots (QDs).[20] These LEDs could be operated continuously, without encapsulation at 30-50% relative humidity (RH) for 10 h under a bias of 10 V and still retained ~80% of the initial efficiency. More recently, Shan et al. reported LEDs with ITO/NiO/ $CsPbBr_3$ QDs/ZnO/Al device configuration, with balanced carrier concentration mobility and reasonable band alignment. These devices exhibited a low turn on voltage of ~2.4 V and retained 70% of the initial EL after operation for 1.75 h at 65% RH.[19]

Notably, inorganic transport layers, typically, metal oxides such as NiO, $WO_3$, ZnO, $SnO_2$, etc., are deposited via different processing techniques compared to the organic transport layers, most commonly by low-temperature radio frequency (RF) magnetron sputtering.[19,25-27] In this case, deposition parameters such as oxygen partial pressure, deposition rate, and substrate temperature, as well as plasma parameters like plasma density, discharge voltages, etc. can significantly affect the properties of the deposited film.[28] The metal oxide layers may also be prepared from solution processing methods, as demonstrated in case of perovskite solar cells.[18,22] However, the use of non-polar solvents which do not degrade the perovskite nanocrystals is critical when depositing transport layers on top of the perovskite layer.[18] Another possibility is to solution process the bottom layer and thermal evaporate the layer on top of the perovskite, as done with the inverted LED configurations, so as to minimize solvent compatibility issues.

Surprisingly, the current reports for perovskite LEDs in which both HTL and ETL are inorganic materials, are based on fully-inorganic perovskite, like $CsPbBr_3$ QDs,[19,20] which are capped by very long chain ligands like oleylamine that can restrict charge injection into the perovskite layer. Even in case of direct thin film crystallization, $CsPbBr_3$ is known to have poor surface coverage (due to the poor solubility of the inorganic perovskite precursors), hence, polymers are

generally used to improve the film formation.[29] However, this can also adversely affect charge injection and reduce the device efficiency. In fact, the highest efficiencies to-date have been achieved with the organic cation-based (FA (refer to Chapter 6) and MA[30]) lead halide perovskites, or mixed cation (Cs-MA) perovskites,[29] which can be more easily solution processed into uniform emitter films. Hence, retaining the hybrid perovskite layer as the emitting material would be beneficial for attaining the high device efficiencies. Moreover, as demonstrated in case of perovskite solar cells, the inorganic transport layers should be able to provide sufficient protection to the hybrid perovskite layer to prevent degradation from environmental factors, improving the device stability and negating the need for external encapsulation.[18] In addition, doping of metal oxide layers is a convenient route to achieve the desired band alignment as well as control the mobility and free carrier concentration in the transport layers.[20] A balanced charge injection would go a long way in preventing charge accumulation and thus reducing the heating effects during device operation. Therefore, use of inorganic transport layers with the efficient organic-inorganic hybrid perovskite layers could be the route to attain both high efficiency and high device stability for perovskite-based LEDs, paving the way towards commercialization.

## 7.3 References

1 Teunis, M. B., Johnson, M. A., Muhoberac, B. B., Seifert, S. & Sardar, R. Programmable Colloidal Approach to Hierarchical Structures of Methylammonium Lead Bromide Perovskite Nanocrystals with Bright Photoluminescent Properties. *Chemistry of Materials* **29**, 3526-3537, doi:10.1021/acs.chemmater.6b05393 (2017).

2 Pan, A. *et al.* Insight into the Ligand-Mediated Synthesis of Colloidal $CsPbBr_3$ Perovskite Nanocrystals: The Role of Organic Acid, Base, and

Cesium Precursors. *ACS Nano* **10**, 7943-7954, doi:10.1021/acsnano.6b03863 (2016).

3 Zhu, F. *et al.* Shape Evolution and Single Particle Luminescence of Organometal Halide Perovskite Nanocrystals. *ACS Nano* **9**, 2948-2959, doi:10.1021/nn507020s (2015).

4 Wang, L. *et al.* Scalable Ligand-Mediated Transport Synthesis of Organic-Inorganic Hybrid Perovskite Nanocrystals with Resolved Electronic Structure and Ultrafast Dynamics. *ACS Nano* **11**, 2689-2696, doi:10.1021/acsnano.6b07574 (2017).

5 Vybornyi, O., Yakunin, S. & Kovalenko, M. V. Polar-solvent-free colloidal synthesis of highly luminescent alkylammonium lead halide perovskite nanocrystals. *Nanoscale*, doi:10.1039/C5NR06890H (2015).

6 Pan, J. *et al.* Air-Stable Surface-Passivated Perovskite Quantum Dots for Ultra-Robust, Single- and Two-Photon-Induced Amplified Spontaneous Emission. *The Journal of Physical Chemistry Letters* **6**, 5027-5033, doi:10.1021/acs.jpclett.5b02460 (2015).

7 Luo, B. *et al.* Organolead Halide Perovskite Nanocrystals: Branched Capping Ligands Control Crystal Size and Stability. *Angew Chem Int Ed Engl* **55**, 8864-8868, doi:10.1002/anie.201602236 (2016).

8 Gonzalez-Carrero, S. *et al.* The Luminescence of $CH_3NH_3PbBr_3$ Perovskite Nanoparticles Crests the Summit and Their Photostability under Wet Conditions is Enhanced. *Small* **12**, 5245-5250, doi:10.1002/smll.201600209 (2016).

9 Li, J. *et al.* 50-Fold EQE Improvement up to 6.27% of Solution-Processed All-Inorganic Perovskite $CsPbBr_3$ QLEDs via Surface Ligand Density Control. *Advanced Materials* **29**, 1603885(1603881-1603889), doi:10.1002/adma.201603885 (2017).

10 Bakueva, L. *et al.* Size-tunable infrared (1000–1600 nm) electroluminescence from PbS quantum-dot nanocrystals in a

semiconducting polymer. *Applied Physics Letters* **82**, 2895-2897, doi:10.1063/1.1570940 (2003).

11 Tyagi, P., Arveson, S. M. & Tisdale, W. A. Colloidal Organohalide Perovskite Nanoplatelets Exhibiting Quantum Confinement. *The Journal of Physical Chemistry Letters* **6**, 1911-1916, doi:10.1021/acs.jpclett.5b00664 (2015).

12 Sichert, J. A. *et al.* Quantum Size Effect in Organometal Halide Perovskite Nanoplatelets. *Nano Letters* **15**, 6521-6527, doi:10.1021/acs.nanolett.5b02985 (2015).

13 Yang, Y., Qin, H. & Peng, X. Intramolecular Entropy and Size-Dependent Solution Properties of Nanocrystal–Ligands Complexes. *Nano Letters* **16**, 2127-2132, doi:10.1021/acs.nanolett.6b00737 (2016).

14 Yang, Y. *et al.* Entropic Ligands for Nanocrystals: From Unexpected Solution Properties to Outstanding Processability. *Nano Letters* **16**, 2133-2138, doi:10.1021/acs.nanolett.6b00730 (2016).

15 Mahmood, K., Sarwar, S. & Mehran, M. T. Current status of electron transport layers in perovskite solar cells: materials and properties. *RSC Advances* **7**, 17044-17062, doi:10.1039/C7RA00002B (2017).

16 Kulkarni, A. P., Tonzola, C. J., Babel, A. & Jenekhe, S. A. Electron Transport Materials for Organic Light-Emitting Diodes. *Chemistry of Materials* **16**, 4556-4573, doi:10.1021/cm049473l (2004).

17 Hughes, G. & Bryce, M. R. Electron-transporting materials for organic electroluminescent and electrophosphorescent devices. *Journal of Materials Chemistry* **15**, 94-107, doi:10.1039/B413249C (2005).

18 You, J. *et al.* Improved air stability of perovskite solar cells via solution-processed metal oxide transport layers. *Nat Nanotechnol* **11**, 75-81, doi:10.1038/nnano.2015.230 (2016).

19 Shan, Q. *et al.* All-inorganic quantum-dot light-emitting diodes based on perovskite emitters with low turn-on voltage and high humidity stability.

*Journal of Materials Chemistry C* **5**, 4565-4570, doi:10.1039/C6TC05578H (2017).

20 Shi, Z. *et al.* High-Efficiency and Air-Stable Perovskite Quantum Dots Light-Emitting Diodes with an All-Inorganic Heterostructure. *Nano Letters* **17**, 313-321, doi:10.1021/acs.nanolett.6b04116 (2017).

21 Jong, M. P. d., IJzendoorn, L. J. v. & Voigt, M. J. A. d. Stability of the interface between indium-tin-oxide and poly(3,4-ethylenedioxythiophene)/poly(styrenesulfonate) in polymer light-emitting diodes. *Applied Physics Letters* **77**, 2255-2257, doi:10.1063/1.1315344 (2000).

22 Kwon, U. *et al.* Solution-Processible Crystalline NiO Nanoparticles for High-Performance Planar Perovskite Photovoltaic Cells. *Scientific reports* **6**, 30759 (2016).

23 Dürr, A. C., Schreiber, F., Kelsch, M., Carstanjen, H. D. & Dosch, H. Morphology and thermal stability of metal contacts on crystalline organic thin films. *Advanced Materials* **14**, 961-963 (2002).

24 Hirose, Y. *et al.* Chemistry and electronic properties of metal-organic semiconductor interfaces: Al, Ti, In, Sn, Ag, and Au on PTCDA. *Physical Review B* **54**, 13748-13758 (1996).

25 Wood, V. & Bulović, V. Colloidal quantum dot light-emitting devices. *Nano Reviews* **1**, 5202, doi:10.3402/nano.v1i0.5202 (2010).

26 Wang, K.-C. *et al.* Low-Temperature Sputtered Nickel Oxide Compact Thin Film as Effective Electron Blocking Layer for Mesoscopic NiO/CH3NH3PbI3 Perovskite Heterojunction Solar Cells. *ACS Applied Materials & Interfaces* **6**, 11851-11858, doi:10.1021/am503610u (2014).

27 Chen, W. *et al.* Efficient and stable large-area perovskite solar cells with inorganic charge extraction layers. *Science* **350**, 944-948, doi:10.1126/science.aad1015 (2015).

28 Ellmer, K. Magnetron sputtering of transparent conductive zinc oxide: relation between the sputtering parameters and the electronic properties. *Journal of Physics D: Applied Physics* **33**, R17 (2000).

29 Zhang, L. Q. *et al.* Ultra-bright and highly efficient inorganic based perovskite light-emitting diodes. *Nature Communications* **8**, 15640, doi:10.1038/ncomms15640 (2017).

30 Xiao, Z. *et al.* Efficient perovskite light-emitting diodes featuring nanometre-sized crystallites. *Nature Photonics* **11**, 108-115, doi:10.1038/nphoton.2016.269 (2017).

# APPENDIX

**Table A1.** Comparison of the 1.15:1 precursor ratio $CH_3NH_3PbBr_3$ NC LED ( discussed in Chapter 4) with other $CH_3NH_3PbBr_3$ NC-based LEDs reported in literature.

| Morphology | Device Architecture | $V_T$ (V) | Max CE (cd $A^{-1}$) | Max PE (lm $W^{-1}$) | EQE (%) | $L_{max}$ (cd $m^{-2}$) | Publication (Month/Year) |
|---|---|---|---|---|---|---|---|
| NP (amorphous) | ITO/PEDOT:PSS/Pe/ TPBi/$Cs_2CO_3$/Al | 3.1 | 11.49 | 7.84 | 3.8 | 3515 | Jun 2016[1] |
| **NC** | **ITO/PEDOT:PSS/Pe/ B3PYMPM/Ca/Al** | **2.7** | **6.45** | **5.98** | **1.75** | **2721** | **This work** |
| NC | ITO/PEDOT:PSS/Pe/ TPBi/CsF/Al | 2.9 | 4.5 | 3.5 | 1.1 | 2503 | Dec 2015[2] |
| Nanoplatelet | ITO/PEDOT:PSS/Pe/ PVK:PBD/BCP/LiF/Al | 3.8 | n.r. | 1.0 | 0.48 | 10590 | Nov 2015[3] |

Footnotes to Table A3: $V_T$ is turn-on voltage, CE is current efficiency, PE is power efficiency, EQE is external quantum efficiency, $L_{max}$ is maximum luminance, Pe refers to the perovskite emitter, viz. $CH_3NH_3PbBr_3$, n.r. indicates the value is not reported. PEDOT:PSS = poly(3,4-ethylenedioxythiophene):polystyrene sulfonate ;TPBI = 2,2′,2″-(1,3,5-benzinetriyl)-tris(1-phenyl-1-H-benzimidazole); B3PYMPM = 4,6-bis(3,5-di(pyridin-3-yl)phenyl)-2-methylpyrimidine; PVK:PBD = (poly(9-vinylcarbazole):2-(4-biphenylyl)-5-phenyl-1,3,4-oxadiazole); and BCP = bathocuproine.


1 Xing, J. *et al.* High-Efficiency Light-Emitting Diodes of Organometal Halide Perovskite Amorphous Nanoparticles. *ACS Nano* **10**, 6623-6630, doi:10.1021/acsnano.6b01540 (2016).

2 Huang, H. *et al.* Emulsion Synthesis of Size-Tunable $CH_3NH_3PbBr_3$ Quantum Dots: An Alternative Route toward Efficient Light-Emitting Diodes. *ACS Applied Materials & Interfaces* **7**, 28128-28133, doi:10.1021/acsami.5b10373 (2015).

3 Ling, Y. *et al.* Bright Light-Emitting Diodes Based on Organometal Halide Perovskite Nanoplatelets. *Advanced Materials* **28**, 305-311, doi:10.1002/adma.201503954 (2016).

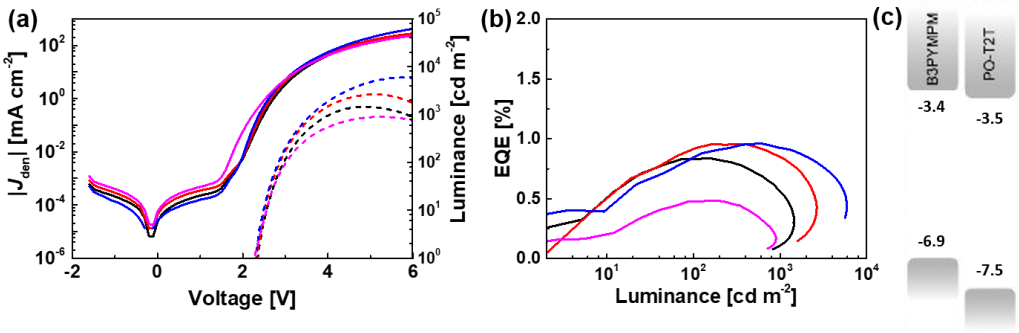


**Figure A1.** (a) J-V-L and (b) EQE versus luminance curves of $CH_3NH_3PbBr$ LEDs wherein PO-T2T was used as the ETL instead of B3PYMPM. The black, red, blue and magenta curves correspond to the 1:1, 1.05:1, 1.15:1, and 1.25:1 ratios of $CH_3NH_3Br$:$PbBr_2$ respectively. In (a), the solid lines represent the J-V curves while the dashed lines represent the L-V curves. (c) HOMO (bottom) and LUMO (top) values of the two ETLs.

## Discussion

Change of ETL from 4,6-bis(3,5-di(pyridin-3-yl)phenyl)-2-methylpyrimidine (B3PYMPM) to 2,4,6-Tris[3-(diphenylphosphinyl)phenyl]-1,3,5-triazine) (PO-T2T) which has lower HOMO level compared to B3PYMPM, increases the hole blocking ability of the ETL. Therefore, when used with the $CH_3NH_3PbBr$ active layer, PO-T2T enabled a significantly lower turn-on voltage of ~2.3V compared to the 2.7-2.8 V in case of B3PYMPM, while the EQE versus luminance trend for the different perovskite ratios were same in both cases. However, the maximum EQE obtained from the $CH_3NH_3PbBr$ LEDs were lower when PO-T2T was used compared to B3PYMPM. Regardless, due to the lower turn-on voltages obtained with PO-T2T compared to B3PYMPM, the former was used as ETL for the devices discussed in Chapters 5 and 6.